Study, analysis and experimental validation of fiber refractometers based on single-mode, multimode and photonic crystal fibers for refractive index measurements with application for the detection of methane

Haris Apriyanto

▶ **To cite this version:**

Haris Apriyanto. Study, analysis and experimental validation of fiber refractometers based on single-mode, multimode and photonic crystal fibers for refractive index measurements with application for the detection of methane. Physics [physics]. Institut National Polytechnique de Toulouse - INPT, 2019. English. NNT : 2019INPT0022 . tel-02088740v3

HAL Id: tel-02088740

https://laas.hal.science/tel-02088740v3

Submitted on 18 Jul 2023

HAL is a multi-disciplinary open access archive for the deposit and dissemination of scientific research documents, whether they are published or not. The documents may come from teaching and research institutions in France or abroad, or from public or private research centers.

L'archive ouverte pluridisciplinaire **HAL**, est destinée au dépôt et à la diffusion de documents scientifiques de niveau recherche, publiés ou non, émanant des établissements d'enseignement et de recherche français ou étrangers, des laboratoires publics ou privés.

THÈSE

En vue de l'obtention du

DOCTORAT DE L'UNIVERSITÉ DE TOULOUSE

Délivré par :

Institut National Polytechnique de Toulouse (Toulouse INP)

Discipline ou spécialité :

Photonique et système optoélectronique

Présentée et soutenue par :

M. HARIS APRIYANTO

le mercredi 27 février 2019

Titre :

Study, analysis and experimental validation of fiber refractometers based on single-mode, multimode and photonic crystal fibers for refractive index measurements with application for the detection of methane

---

Ecole doctorale :

Génie Electrique, Electronique, Télécommunications (GEET)

Unité de recherche :

Laboratoire d'Analyse et d'Architecture des Systèmes (L.A.A.S.)

Directeur(s) de Thèse :

M. HAN CHENG SEAT

M. OLIVIER BERNAL

Rapporteurs :

M. CHRISTOPHE CAUCHETEUR, UNIVERSITE DE MONS

M. PHILIPPE ROY, CNRS

Membre(s) du jury :

M. FRANCK CHOLLET, UNIVERSITE DE FRANCHE COMTE, Président

M. DOMINIQUE LEDUC, UNIVERSITE DE NANTES, Membre

M. FREDERIC SURRE, UNIVERSITY OF LONDON, Invité

M. GUY PLANTIER, EC SUP ELECTRONIQUE OUEST, Membre

M. HAN CHENG SEAT, INP TOULOUSE, Membre

Mme VALERIE CHAVAGNAC, CNRS TOULOUSE, Membre

M. MICHEL CATTOEN, INP TOULOUSE, Invité

M. OLIVIER BERNAL, INP TOULOUSE, Membre

Abstract

Refractive index measurement has been studied since Ernest Abbé initially designed a refractometer in 1869, which is named the Abbé refractometer. Since then, numerous types of refractometers have been developed by employing either the optical prism-based refractometer or the optical fiber-based refractometer, due to their wide-ranging applications such as for sensing various physical, biological and chemical parameters. Recently, a large number of researchers have been developing refractometers based on optical fibers, exploiting mechanisms such as surface plasmon resonance (SPR), multimode interference, fiber Bragg gratings (FBG), long-period gratings (LPG), tapered optical fibers, and striped-cladding multimode fibers (MMFs), for their advantages in immunity against electromagnetic interference, electrical passivity at the sensing probe, and capability to long term *in situ* measurement.

This thesis concerns the development of comprehensively functional and accurate models for optical fiber refractometers based on optical intensity modulation, in particular for stripped-cladding MMF refractometry as well as hybrid systems involving a combination of single-mode-multimode fiber refractometery and the all-fiber hybrid refractometer using photonic crystal fibers. A key objective of this work is to characterize the performance of these intensity-based optical fiber refractometers in terms of their power response, sensitivity, resolution, and dynamic range. The simulation results which are corroborated experimentally demonstrate very high sensitivity being obtained in Zone II (i.e. the sensing regime typically employed for measuring a sensing medium index higher than the cladding index but less than or equal to the core index) for all three types of refractometers. However, the sensitivity in Zone III (i.e. the sensing regime for which the sensing medium index is higher than the core index) is very low. A hybrid single-mode fiber - multimode fiber configuration is used to improve the sensitivity in Zone III. On other hand, the sensitivity for Zone I (i.e. the sensing regime typically employed for measuring a sensing medium index lower than the cladding index) has been improved by increasing evanescent wave absorption using the all-fiber hybrid refractometer based on solid-core photonic crystal fibers.

As a further potential of the fiber refractometer for applications in biochemical sensing, the proof-of-concept for a methane gas sensor has been demonstrated using supramolecular cryptophane-A which enables to trap the methane molecules. Cryptophane-A incorporated into a functionalized film of Styrene-Acrylonitrile (SAN) host is applied to a de-cladded region of the sensor as the sensitive region. The refractive index of this functionalized layer increases proportionally with increasing methane concentration, subsequently inducing variations in the transmitted optical power along the fiber sensor.

Keywords: refractometer, refractive index, fiber optic, multimode fiber, photonic crystal fibers, cryptophane-A, methane gas.

Résumé

La mesure de l'indice de réfraction a été étudiée depuis qu'Ernest Abbé aie initialement conçu un réfractomètre en 1869, appelé le réfractomètre d'Abbé. Depuis lors, de nombreux réfractomètres ont été développés tels que le réfractomètre à prisme optique ainsi que le réfractomètre à fibre optique, en raison de leurs applications étendues pour la détection de divers paramètres physiques, biologiques et chimiques. Récemment, un grand nombre de chercheurs ont mis au point des réfractomètres basés sur des fibres optiques, exploitant des mécanismes tels que la résonance des plasmons de surface (SPR), les interférences multimodes, les fibres à réseaux de Bragg (FBG), les fibres à réseaux à longues périodes (LPG), les fibres optiques coniques et la fibre multimode à gaine dénudée. Les capteurs fibrés sont avantageux grâce à leur immunité contre les interférences électromagnétiques, passivité électrique au niveau de la sonde de détection et potentiel de mesure *in situ* à long terme.

Cette thèse concerne le développement de modèles complets fonctionnels et précis pour les réfractomètres à fibres optiques basés sur la modulation d'intensité optique, en particulier la réfractométrie à fibre multimode à gaine dénudée ainsi que les systèmes hybrides associant fibres monomode et multimode, et un réfractomètre hybride tout fibré utilisant des fibres à cristaux photoniques. L'objectif clé de ce travail est de caractériser les performances de ces réfractomètres à fibres optiques basés sur la modulation d'intensité en termes de réponse en puissance, de sensibilité, de résolution et de dynamique de mesure. Les résultats de simulation qui sont corroborés expérimentalement démontrent que la très grande sensibilité obtenue dans la zone II (c'est-à-dire le régime de détection typiquement utilisé pour mesurer l'indice du milieu supérieur à l'indice de gaine mais inférieur ou égal à l'indice du cœur) pour tous les trois réfractomètres. Cependant, la sensibilité dans la Zone III (c'est-à-dire le régime de détection pour lequel l'indice du milieu à mesurer est supérieur à celui du cœur) est très faible. Ainsi, un refractomètre fibré hybride monomode-multimode est utilisé pour améliorer la sensibilité dans la Zone III. D'autre part, la sensibilité pour la zone I (c'est-à-dire le régime de détection pour mesurer l'indice du milieu inférieur à l'indice de la gaine) a été améliorée en augmentant l'absorption des ondes évanescentes à l'aide du réfractomètre hybride tout fibré à base de fibres à cristaux photoniques à cœur solide.

En termes d'application réelle du réfractomètre à fibre pour la détection biochimique, une preuve de concept pour un capteur du gaz méthane a été démontrée en utilisant les supramolécules de cryptophane-A qui permettent de piéger les molécules du méthane. Le cryptophane-A incorporé dans un film hôte à base de styrène-acrylonitrile (SAN) est appliqué sur la zone dénudée du capteur comme une région fonctionnalisée. L'indice de réfraction de cette couche sensible augmente proportionnellement avec l'augmentation de la concentration du méthane, ce qui induit une variation de la puissance optique transmise dans le capteur fibré.

Mots clés: réfractomètre, indice de réfraction, fibre optique, fibre multimode, fibres à cristaux photoniques, cryptophane-A, gaz méthane.

Acknowledgements

I would first like to thank Prof. Thierry Bosch for giving me the opportunity to joint the OSE research group. I would like to express my sincere gratitude to my supervisor Dr. Han Cheng Seat, for his continuous guidance, support, patience and motivation throughout my PhD program. He showed always enthusiasm during many unexpected short meeting in his office, and suggested to me ideas concerning the technical aspect of work. I would also thank my co-supervisor Dr. Olivier Bernal, for his advices. He helped me many times to solve some programming problems.

I take this opportunity to express my thankfulness to Prof. Franck Chollet as the president of jury. I would also like to thank Dr. Phillipe Roy (Research Director at XLIM Limoges) and Prof. Christophe Caucheteur (Professor in University of Mons, Belgium), for accepting to be the reviewers of my thesis. I'm thankful for any advice and suggestions from all the jury members (Dr. Valérie Chavagnac, Dr. Dominique Leduc, Prof. Guy Plantier, Prof. Michel Cattoen, and Dr. Frédéric Surre).

I'm grateful to all researchers and staffs of OSE group (Marc Lescure, Michel Cattoen, Françoise Lizion, Francis Bony, Hélène Tap, Julien Perchoux, and Adam Quotb) for their kindness. I'm also grateful to Francis Jayat et Clement Tronche for their help in experimental stuff, and Emmanuelle Tronche for her help in administrative stuff. I would also like to thank my colleagues (Yu Zhao, Gautier Ravet, Fernando Urgiles, Mengkoung Veng, Raul da Costa Moreira, Clement Deleau, Einar Knudsen, Bastian Grimaldi, and Farouk Amish) for their friendship and help.

I must express my most profound gratitude to my parents in Indonesia, my wife and my lovely children (Affan and Sofyan) for their support in most difficult moments. I acknowledge the financial support from the Indonesia Endowment Fund for Education (LPDP), Ministry of Finance, Republic of Indonesia. Without this financial support, I would not finish this thesis.

CONTENTS

General Introduction

In the 1960s, Charles Kuen Kao led some revolutionary and ambitious work in developing and experimentally investigating the low-loss glass-based optical fiber by technically removing most of the existing impurities in Quartz which was employed as the key component material in the fiber [1]. His successful accomplishment in the realization of the low-loss optical fiber led Kao to being regarded as “the father of fiber optics” for which he was later awarded one half of the Nobel Prize in Physics in 2009 for “groundbreaking achievements in the transmission of light in fibers for optical fiber communication”. The other co-Laureates of the Nobel Prize were Willard S. Boyle and George E. Smith for “the invention of an imaging semiconductor circuit – the CCD sensor”.

The aftermath of this successful trial experiment on low-loss optical fiber has since motivated researchers to exploit fiber optics not only in applications for broadband telecommunications, but also for numerous sensing and measurement domains. This motivation can also, in large part, be attributed to certain advantages intrinsic to the optical fiber over more conventional electro-mechanical sensor technologies, such as its immunity to electromagnetic interference, small size and light weight, electrical passivity at the sensing probe or head, multiplexing potential, and remote sensing capability [2-4].

Optical fiber sensors (OFSs) have been successfully exploited, either as extrinsic devices where the optical fiber simply acts as a waveguide to transmit a useful optical signal from the measurement point to the photodetector, or as an intrinsic sensor with the fiber acting directly as the sensing element subject to a modulation of the interrogating lightwave's optical properties (such as optical intensity, phase, refractive index, propagation direction and velocity, etc.) as a function of the physical quantity being measured [2, 5]. OFSs have been developed for many applications such as for sensing various physical, biological, and chemical parameters. As a chemical sensor, the OFS is commonly employed for sensing chemical processes, monitoring environmental conditions, and pollution parameters

due to its robustness to relatively harsh ambient conditions and its chemical inertness while offering explosion-free security since the sensor requires no electrical power at the sensing point [5]. In addition, the OFS offers rapid continuous real-time *in situ* measurement potential for remote sensing.

In chemical sensing, one sensor type that is frequently employed is the bulk refractive index (RI) sensor or refractometer for quantifying the concentration level of various aqueous solutions, such as sucrose, salt, glycerol, dimethyl sulfoxide (DMSO), methanol, aceto-nitrile, etc [6], in addition to measuring other parameters like temperature since the RI of a medium is generally temperature-dependent [7-11]. Further, the advent of the sol-gel technique has facilitated the synthesis of bespoke sensitized coatings that can be deposited on the surface of an optical fiber as a thin film in replacement of the cladding [12-14]. This approach can allow the fiber-based refractometer to selectively measure specific organo-chemical species. For example, using a thin film of Polydimethylsiloxane (PDMS) functionalized by incorporating cryptophane-A or cryptophane-E supramolecules as the sensitive region [15], the refractometer can be used to detect methane (CH_4) concentration. The cryptophane-based molecular traps will absorb or entrap the CH_4 molecules and reversibly produce a bond in the bulk polymeric material that will induce variations in the RI of the sensitized region as a function of CH_4 concentration [15].

Various operating principles have been exploited for fiber RI sensing schemes such as surface plasmon resonance (SPR) [16-20], multimode interference (MMI) [21-24], fiber Brag gratings (FBGs) [25-28], long-period gratings (LPGs) [29-32], etc. These techniques exploit spectral or wavelength modulation-based measurements, generally requiring a spectrometer or an optical time-domain reflectometer (OTDR) to extract the RI values as a function of the variation in the measured spectrum. Sensor instrumentation employing the expensive but high-precision spectrometer and/or the OTDR is thus not very cost-effective and practical for field measurements, in addition to the relative fragility of these instruments.

However, a simple and relatively cost-effective OFS-based refractometer can potentially be realized by exploiting intensity modulation-based schemes in which the variation of RI values will induce a variation in the measured optical power.

Several techniques for fiber refractometry based on intensity modulation have been successfully developed using Fresnel reflection at the end face of a single-mode fiber (SMF) [33], tapered optical fibers [34-35], and a totally or partially stripped cladding as the sensing region in a multimode fiber (MMF) [36-39].

This thesis concerns the development of comprehensively functional and accurate models for OFRs based on intensity modulation, in particular for stripped-cladding type MMF refractometry as well as hybrid systems involving a combination of SMFs, MMFs, and photonic crystal fibers (PCFs). One key objective of this work is to characterize the performance of these intensity-based OFRs in terms of their power response, sensitivity, resolution, and dynamic range. As a further demonstration of the potential of the fiber refractometer for applications in biochemical sensing, in particular in selective gas sensing, a CH_4 gas sensor has been realized using a thin (~12 µm) functionalized film of Styrene-Acrylonitrile (SAN) incorporating cryptophane-A supramolecular traps as the sensing region (de-cladded area). This PhD thesis, entitled "Study, analysis and experimental validation of fiber refractometers based on single-mode, multimode and photonic crystal fibers for refractive index measurements with application for the detection of methane", is composed of five chapters briefly summarized below. Some conclusions and a discussion on perspectives for future work conclude this thesis.

Chapter I introduces the refractive index as a key optical parameter for refractometric applications while also giving an overview of the existing techniques behind refractive index measurements, using both the optical fiber and non-optical fiber-based sensor systems. In this chapter, the general principles of refractive index measurement using various sensor types based on intensity modulation as well as those employing wavelength modulation-based techniques are discussed.

In Chapter II the stripped-cladding MMF refractometer together with its operating principles for refractive index sensing are described. In particular, the classification of the sensing zones as a function of the different sensing mechanisms involved is comprehensively studied. In addition, the accurate operational models henceforth developed to estimate the power response of these fiber sensors for each zone are

detailed. The models are then validated experimentally by employing a combination of glycerol-water solutions and calibrated oils.

Chapter III discusses the design of a hybrid fiber refractometer based on fusion splicing an SMF to an MMF to further improve the sensor performance, particularly by reducing parasite mechanical vibration noise and by improving the sensitivity in two of the higher RI regions (Zone II and Zone III). The development of the actual models for this hybrid system is carried out by adapting those developed in Chapter II to accurately estimate the optical power response of the refractometric sensor. Further experimental corroboration for this refractometer is also performed by a similar measurement procedure as carried out in Chapter II.

Chapter IV is dedicated to investigating the prospect of exploiting solid core PCFs in RI measurements. Two different schemes for injecting the interrogating laser beam into a PCF are investigated theoretically and experimentally, one of which uses a hybrid SMF-PCF-MMF architecture while the second involves an SMF-MMF-PCF-MMF hybrid design. The key objective is to achieve a significant increase in evanescent wave absorption (EWA), thus leading to several fold improvements in the measurement sensitivity in the lower index region (Zone I). It is found that EWA can be increased in solid-core PCFs by controlling or configuring their ability to guide injected lightwaves in the outer silica cladding of the fiber. Experimental measurements are next performed on solid-core PCFs with their coating removed. These fiber sections are then employed as the sensing element for probing an aqueous medium whose RI is varied, similar to the experiments carried out in Chapters II and III.

Chapter V demonstrates the proof-of-concept of the developed fiber optic-based refractometers for CH_4 detection. Here, the procedure to realize the CH_4 sensor involves employing a thin polymeric film of SAN incorporating Cryptophane-A supramolecules as the sensitized region or layer of the sensor. Methane gas is subsequently detected by the supramolecular traps (Cryptophane-A) which selectively absorb or entrap the CH_4 molecules, and reversibly produce a bond in the bulk polymeric material of SAN that induces a variation in the RI of the sensitized region as a function of CH_4 concentration. The preliminary results demonstrate the

capability of this sensor to detect CH_4 with a resolution of 174 ppm, but have an issue with repeatability, i.e. the sensor has only good sensitivity during the first measurement while degradation in performance (sensibility) occurs when the same sensor is re-used in subsequent measurements.

Conclusions and Perspectives concludes the work performed in this thesis, offers some recommendations with regard to improving the performance of the CH_4 sensor as well as discusses further prospective applications of the fiber refractometers developed in this research.

Chapter I

Refractive Index Measurement

1.1. Introduction

The refractive index (RI) or index of refraction n of a substance is defined as the ratio of the speed of an electromagnetic wave in vacuum c (= 2.99792458×10^8 m/s) to its velocity in that substance v, or $n = c/v$ [40]. According to this definition, RI could be used to describe "the optical velocity density" of a medium, since the light velocity propagating through a medium depends on the RI value of that medium. RI can also determine the deviation of the light's ray path when traversing or refracting into another medium. This is described by Snell's law, given by $n_1 \sin\theta_1 = n_2 \sin\theta_2$, where n_1 and n_2 are the indices of the first and second medium, while θ_1 and θ_2 represent the incident and refracted angles, respectively, as schematically illustrated by Figure 1.1 [41].

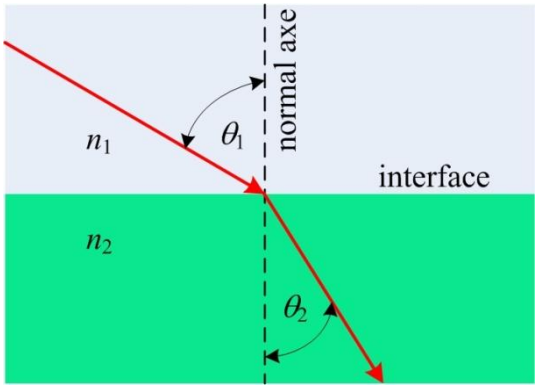

Figure 1.1. Refraction occurring when light passes from one medium into another.

The RI value is an important optical property in a dielectric medium for studying the laws of reflection and refraction. The law of reflection was introduced by Euclid in 300 B.C.E., while the refraction law was initiated in 50 B.C.E. by Cleomedes which was then continued by Claudius Ptolemy (130 C.E.) who realized a precise tabulation of the angles of incidence and refraction for several media through experimental measurements [41]. Abu Sa`d al-`Alā' Ibn Sahl (940–1000 C.E.), a mathematician and physicist who worked at the Abbasid court in Baghdad, introduced a

diagrammatical illustration of refraction. He also described both parabolic and ellipsoidal burning mirrors, as well as analyzed the hyperbolic plano-convex and biconvex lenses. Further, Abu Ali al-Hasan ibn al-Haytham, known also in the western world as Alhazen (965–1039 C.E.), elaborated the Law of reflection using spherical and parabolic mirrors. In the 17th century, a Dutch spectacle maker, Hans Lippershey, applied for a patent on a refracting telescope in October 1608, while in 1609 Galileo Galilei, inspired by this invention, then built his own version of telescope. In 1611, Johannes Kepler discovered total internal reflection, and described the detailed operating principles for both the Keplerian (positive eyepiece) and Galilean (negative eyepiece) telescopes. Willebrord Snel, more commonly known as Snell and Professor at Leiden University, in 1621 empirically discovered the Law of Refraction. The Law of Refraction was then simplified by René Descartes into the current sine form in 1637, which today is known as Snell-Descartes' law or Snell's law [41].

Since then Snell-Descartes' law has been universally exploited in various optical measurements, in particular for RI measurement (refractometry), to study the optical properties of materials. Additionally, according to Maxwell's equation, RI represents the relationship between the permittivity ε and permeability μ (with $n = \sqrt{\varepsilon\mu}$) of a dielectric material or medium. Therefore, RI is a unique intrinsic optical property of a specific material in relation with the propagation characteristics. By measuring RI, one can, for example, investigate the presence of impurities or contaminants in a medium for quality control purposes [42-45]. In addition, accurate knowledge of this parameter is important to enable the manipulation of lightwave propagation through any dielectric medium in a form of a waveguide or an optical fiber. In this context, various measurement techniques, including those most widely-exploited currently in both research and in the industry, are briefly discussed in the following sections.

1.2. Refractive index measurements

The measurement of RI (refractometry) is typically carried out using an optical glass-based prism where an incoming light beam is made to incident on one of the inclined sides of the prism. By varying the index of the target medium which is in direct

contact with the prism, the critical or refraction angle will vary following Snell-Descartes' law, as a function of the incident angle and the medium index being investigated. The angular variation is then quantified and translated into the desired RI value.

In 1869, Ernest Abbé designed the first refractometer which was then known as the Abbé refractometer. This refractometer was subsequently commercialized in 1881 by Carl Zeiss, a Swiss Company which became the first and only manufacturer of the refractometer for over 40 years [46]. The Abbé refractometer is both simple and quick to use for measuring RIs of both solid and liquid media. In 1887, a second critical-angle refractometer was designed by Carl Pulfrich which became known as the Pulfrich refractometer [46]. Hereafter, in 1899, Pulfrich succeeded in designing an immersion refractometer which allowed direct quick measurement of the RI of liquids under storage [47]. Another refractometer type is a hand-held device which was designed as a low-cost and portable refractometer using prism optics for measuring the RI of liquids [48]. This refractometer has since been further developed into a digital refractometer using an LED source and a photoelectric sensor to replace the traditional eye observation technique [49].

In addition to the prism optic-based refractometer, other refractometer types, such as the interference-based [50-52] and optical fiber-based devices [53-63], have also been developed. Interference-based refractometers allow for measuring the RI value of a medium which is usually in gaseous form by observing the movement of the interference pattern across a calibrated scale through an optical microscope [50]. For the optical fiber-based refractometer, the variation in RI values of the medium can be measured using optical intensity modulation as well as wavelength or spectral modulation. Some widely-exploited principles and techniques for RI measurements are discussed below.

1.2.1. The Abbé refractometer

The Abbé refractometer was the first refractometric device constructed by Ernest Abbé (Figure 1.2) in 1869. In 1874, Abbé then published a comprehensive booklet

which described the operating principle of his invention, as well as the construction process [46, 64].

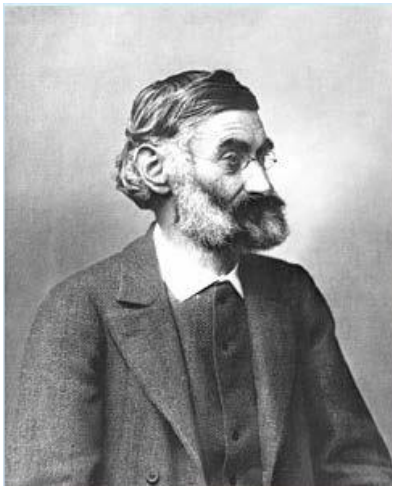

Figure 1.2. Ernest Abbé, inventor of the Abbé refractometer [65].

Despite its first construction in 1869, the Abbé refractometer, illustrated in Figure 1.3(a), was only commercialized in 1881 by Carl Zeiss [66]. Until the beginning of the twentieth century, Carl Zeiss exclusively manufactured the Abbé refractometer [64]. Nevertheless, the enduring success of the Abbé refractometer could be measured through the existence of different variants of refractometric devices derived from the original Abbé design (Figure 1.3(b)).

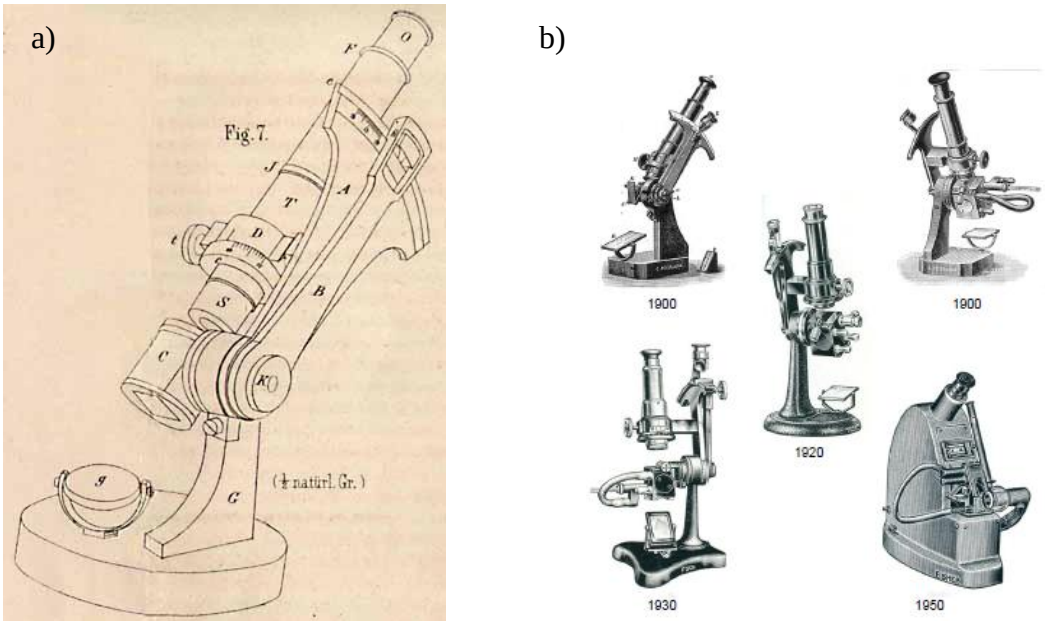

Figure 1.3. The Abbé refractometer: a) the first Abbé refractometer designed by Ernest Abbé [66], and b) variants of the Abbé instrument [65].

This refractometer works in the visible wavelength range and measures the RI of a substance by observing the variation of the angle of refraction as a function of RI using prism optics. Although many variants of the Abbé refractometer exist, their basic operating principle is similar and is based on the measurement of the refraction angle of a light beam through a thin layer of sample medium sandwiched between two glass prisms. The light source is incident from a lower or illuminating prism which is directly above a mirror reflector as the light source. Above the illuminating prism, a sample medium is placed in direct contact between this prism and a measuring prism (or an upper prism). This allows the refracted light from the sample medium to be refracted again in the latter measuring prism (Figure 1.4(a)).

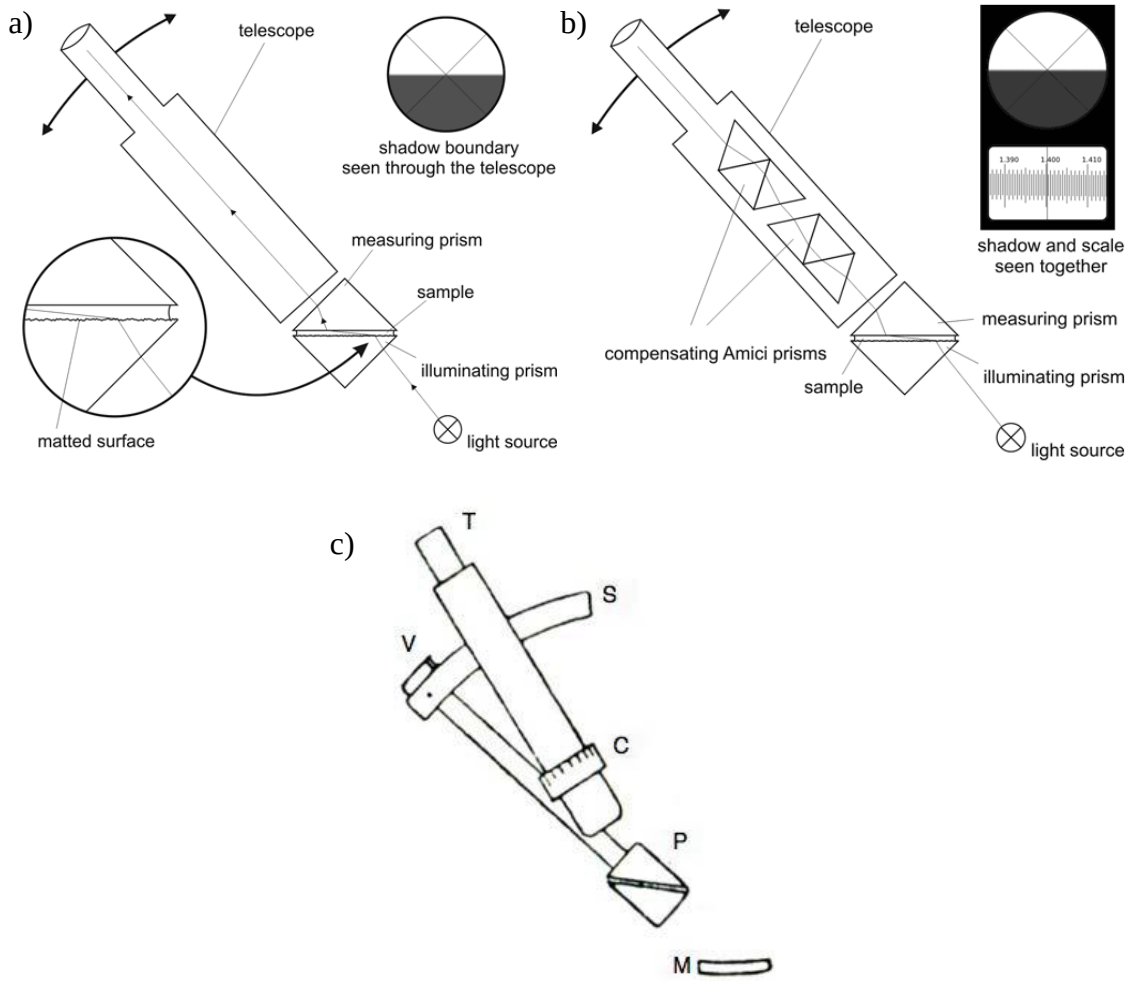

Figure 1.4. Schematic of the Abbé refractometer, illustrating a) basic principle of the instrument [67], b) integrating Amici prisms within the telescope tube to compensate diffraction effects [67], and c) schematic of Abbé refractometer with Vernier displacement (V), telescope (T), scale (S), compensator (C), mirror (M), and prism (P) with its rotating holder [66].

Here, the input light is incident at the illuminating glass prism (with index n_g) at an angle θ_{i1}. This is refracted into the sample medium with a refracted angle θ_{r1}. The RI of the sample medium n_{sm} can thus be calculated using Snell's law as a function of n_g, θ_{i1}, and θ_{r1} via

$$n_g sin\theta_{i1} = n_{sm} sin\theta_{r1} \tag{1.1}$$

The refracted light within the sample will again be refracted into the measuring prism (of index n_g) with a refracted angle θ_{r2} according to

$$n_g sin\theta_{r2} = n_{sm} sin\theta_{r1} \tag{1.2}$$

Since n_g is known, n_{sm} can thus be calculated using Equations (1.1) and (1.2) for a given θ_{i1} corresponding to the refracted angle θ_{r2}. In practice, the mathematical calculation is not necessary since the Abbé refractometer has a holder beneath a telescope (T) (Figure 1.4(c)) with a set of crosshairs which can gradually be rotated for scanning the light exiting the measuring prism. This telescope is mounted with a displacing Vernier (V) which is connected to the turning knob of the prism holder along a fixed scale as illustrated in Figure 1.4(c). The measurement is thus realized by sandwiching the sensing medium between the illuminating prism and measuring prism. This is then observed with a small magnifying lens attached to the Vernier. The point at which half of the visual field is light and the other half is dark is next obtained by turning the telescope holder to give the measured RI scale as illustrated in the inset of Figure 1.4(b) [65].

The basic principle of the Abbé refractometer described above could, however, only function for a monochromatic light due to dispersion at other wavelengths. To reduce or eliminate dispersion, two compensating Amici prisms are added to the design as shown in Figure 1.4(b). This complete design also has the advantage that both the telescope position and that of the Amici prisms can be adjusted to correct the dispersion effects [67].

1.2.2. The Pulfrich refractometer

The Pulfrich refractometer is another refractometer that was developed around 1887 by Carl Pulfrich (Figure 1.5), a German physicist who worked at Carl Zeiss for most

of his career. This refractometer used only a single optical prism (the measuring prism), while the Abbé refractometer in the previous section (1.2.1) employed a dual prism system (i.e. illuminating and measuring prisms) [65].

Figure 1.5. Carl Pulfrich, inventor of the Pulfrich refractometer and the immersion refractometer [65].

In the Pulfrich refractometer, the measured sample medium is placed on top of the measuring glass prism. Monochromatic light is then positioned almost horizontally to the sample medium from which the incident beam arrives at the prism face at grazing incidence (Figure 1.6(a)). The light is focused onto the sample medium and the exit angle on the adjacent prism face is measured using a telescope which can be turned along the circular transit (Figure 1.6(b)). Similar to the Abbé refractometer, the measurement of the sample index is performed by taking the point at which half of the optical field is dark and half is light. This position is subsequently translated into RI units by the circular transit.

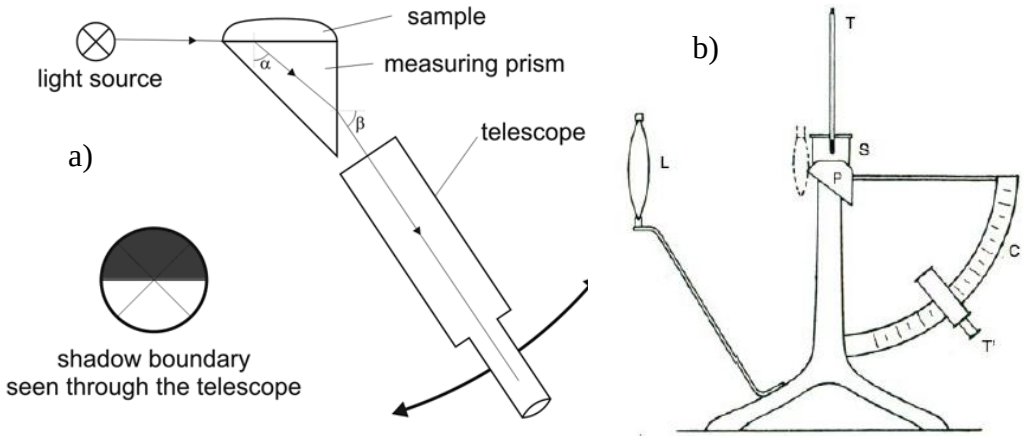

Figure 1.6. a) Schematic of the basic principle of the Pulfrich refractometer [65], and b) simplified cross-section of the Pulfrich refractometer, with thermometer (T), sample compartment (S), prism (P), light source (L), transit circle (C), and telescope (T') [65].

To compensate the influence of temperature, a hollow metal jacket with flowing water is used to surround the measuring prism and is equipped with a top cover which is also of hollow metal as illustrated in Figure 1.7.

Figure 1.7. Metal water-jacket to control temperature in the Pulfrich refractometer [68].

These are connected in series with a thermometer which is immersed into a cell for holding the target liquids. Thus, both the measuring prism and the substance experimented upon are entirely jacketed, except the vertical prism face from which the light emerges and a small rectangular aperture by which the light enters the prism. Therefore, by pumping a stream of water at constant temperature through the system, a very constant temperature can be maintained [69].

1.2.3. The immersion refractometer

The immersion or dipping refractometer was initially designed by Carl Pulfrich, and then commercialized by Carl Zeiss in 1899. This original design was then modified by Lowe in 1902 [70]. The immersion refractometer was designed primarily for determining and measuring solution concentrations, such as in the sugar industry, pharmaceutical products, milk serum, and alcohol. This refractometer is also very useful, in particular, for measuring the RI of acids since only the inert glass prism is immersed and therefore in contact with the corrosive acid solution.

The original Pulfrich immersion refractometer can detect RI variation (resolution) down to 4.2×10^{-5} RIU over a dynamic range of 1.325 to 1.367 RIU. Despite a relatively high resolution, the accuracy of the immersion refractometer was limited since a calibration process was necessary through a known sample for every new measurement [70]. Similar to the Abbé and Pulfrich refractometers, the immersion

refractometer measurement is based on the critical angle represented by the bordering dark and light regions. Nevertheless, unlike the Abbé and Pulfrich refractometers, the immersion device is not supported by the moveable telescope incorporating a Vernier for reading the RI value. In its place, a calibrated micrometer screw is employed to measure the fractional distance required to displace the border to the nearest scale division. The dark and light regions will thus be projected onto the linear scale-reading to determine the corresponding index of the measured liquid (Figure 1.8(a)) [65].

a) b)

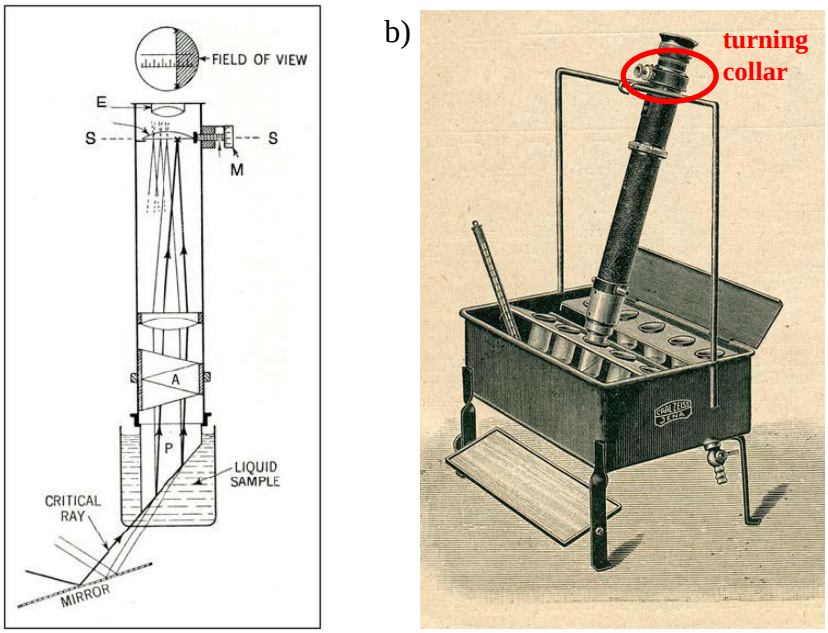

Figure 1.8. Immersion refractometer [65]: a) schematic of immersion refractometer with eye-piece (E), scale (S), micrometer (M), Amici prism (A), and prism (P), and b) image of Zeiss immersion refractometer with a turning collar.

The immersion refractometer exploits ambient light as the illuminating source by employing a reflector mirror below the refractometer as illustrated in Figures 1.8(a) and 1.8(b). Since white light is used as the light source, an Amici prism (A) is needed to compensate the diffraction effects. This prism can be adjusted by turning a collar on the telescope barrel, below the eye-piece (see Figure 1.8(b)).

1.2.4. Hand-held refractometers

Hand-held refractometers are one of the most popular analog instruments used for determining the RI of a liquid due to their relatively low cost and portability. These

refractometers were initially produced by Carl Zeiss in 1955 for applications in the fruit and food processing industry for measuring fruit culture, sugar concentration, moisture content of honey as well as in other related industries [71]. These refractometers employ only a single measuring prism incorporating an illuminator flap with matted surface to hold the target liquid, as illustrated in Figure 1.9.

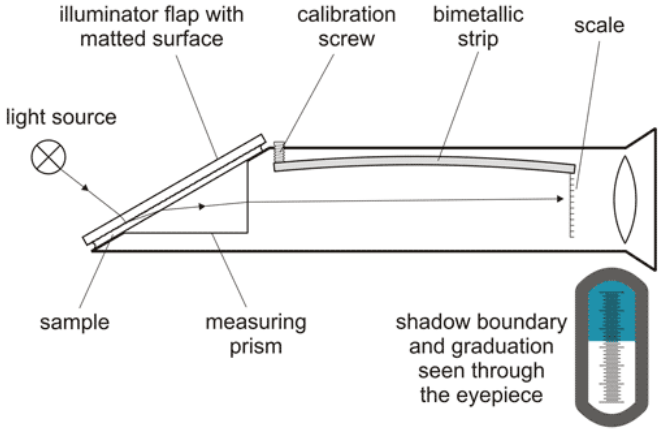

Figure 1.9. Typical example of hand-held refractometer [72].

The basic measurement principle of hand-held refractometers is by measuring the variation of the refraction angle in relation to the target liquid index and is similar to the immersion refractometer which commonly exploits ambient light as the source for illumination. Thus the illuminating light will be refracted in the illuminator flap, the measured liquid medium, as well as the measuring prism and will be projected onto a measuring scale. The measured liquid index can then be read by observing the position of a shadow boundary on the measuring scale which displaces with variation of the refracted angle. In addition, as the RI value is a function of temperature, a bimetallic strip is coupled to the measuring index scale to compensate temperature variation by adjusting the calibration screw.

1.2.5. Hand-held digital refractometers

The hand-held digital refractometer was developed as a result of the successful development in low-cost integrated optoelectronic devices such as, in particular, the light-emitting diode (LED) and photodetector or photoelectric sensor. This refractometer uses an LED as the illuminating source and a photoelectric sensor to

replace the eye observation technique which could be subject to operator-induced errors as illustrated in Figure 1.10(a).

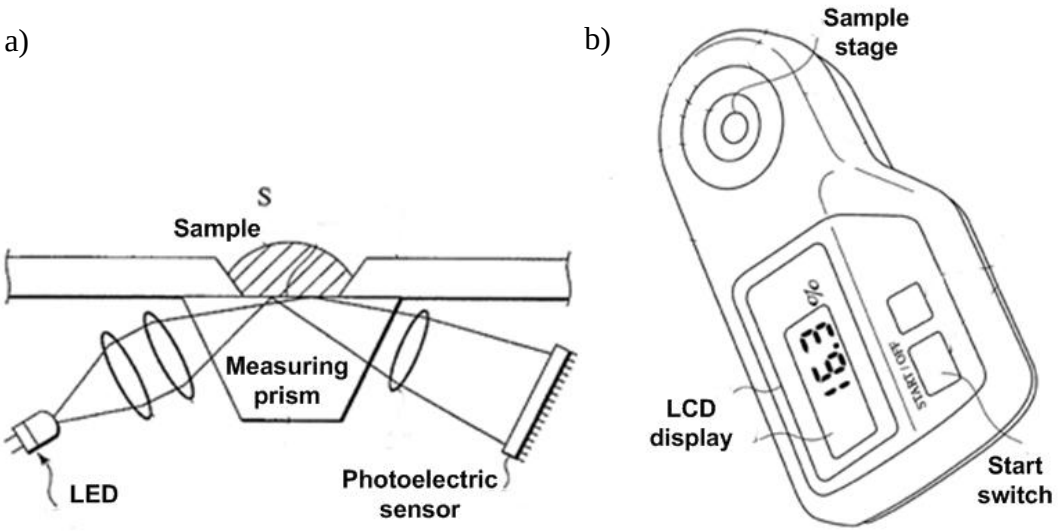

Figure 1.10. Hand-held digital refractometer [49] with a) schematic of the measurement principle, and b) sketch of the hand-held digital refractometer.

For measuring the RI of a sample, the target liquid is first placed above a measuring prism. An LED source radiates the light into the measuring prism, which then arrives at the interface between the prism and the liquid under investigation within a certain range of incident angle. The proportion of reflected light into the photoelectric sensor and the refracted light into the liquid then depends on the liquid index since the incident beam angle and the measuring prism index are constant. Furthermore, this refractometer is supported by a digital temperature compensator for measurement correction when the temperature is beyond that specified for the measurement range. The measured RI value and temperature are then displayed on an LCD monitor as illustrated in Figure 1.10(b).

1.2.6. Fiber optic surface plasmon resonance refractometers

The surface plasmon resonance (SPR)-based optical fiber device can typically be realized as illustrated in Figure 1.11. The cladding and coating of a plastic-clad silica (PCS) multimode fiber (MMF) with a relatively large numerical aperture (*NA*), for example 0.40, must first be removed over a certain length (e.g. 1 cm). The unclad MMF is then coated with a thin metal nano-particle layer (typically silver nano-particles) of several 10's of nm thick. This metal layer could be followed by a very

thin silicon layer of several nm thick (e.g. 5 nm) to increase the sensitivity and to protect the metal layer from oxidation [73]. This coated section will serve as the sensing region which is surrounded by the target or sensing medium. Polychromatic light with a fixed angle of incidence is next launched into the system via a microscope objective and guided along the fiber by the phenomenon of total internal reflection (TIR) [73, 74]. If this incident angle is accordingly matched to a pre-determined propagation condition, resonance will occur at a specific wavelength known as the resonance wavelength [73, 74]. Spectral or wavelength interrogation is typically used for measuring the refractive index value by exploiting a spectrometer or an equivalent system.

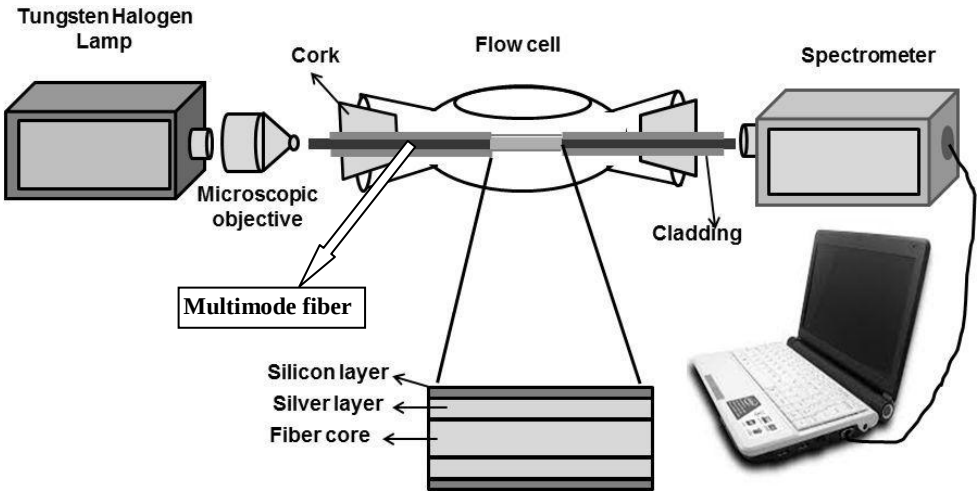

Figure 1.11. Schematic of a typical fiber optic SPR-based refractometer [74].

Any index variation of the sensing medium will thus induce a shift of the resonance wavelength which will be indicated by a sharp dip of the transmitted power over the interrogated wavelength range as represented in Figure 1.12. The SPR curves in Figure 1.12(a) show that the resonance wavelength increases and shifts towards the longer wavelength with increasing index values for a constant silicon layer thickness. Figure 1.12(b), on the other hand, illustrates the resonance wavelength variation when this thickness is varied from 0 nm, 5 nm, 7 nm, and 10 nm, respectively. Hence, for a fixed RI value, increasing the thickness of the silicon layer will induce an increasing resonance wavelength as well as an increase in the sensitivity (as seen from the curves' slope or gradient in Figure 1.12(b)). Nevertheless, the silicon layer

thickness cannot be increased indefinitely since this will increasingly broaden the SPR response and reduce the system accuracy [73].

a)

b)

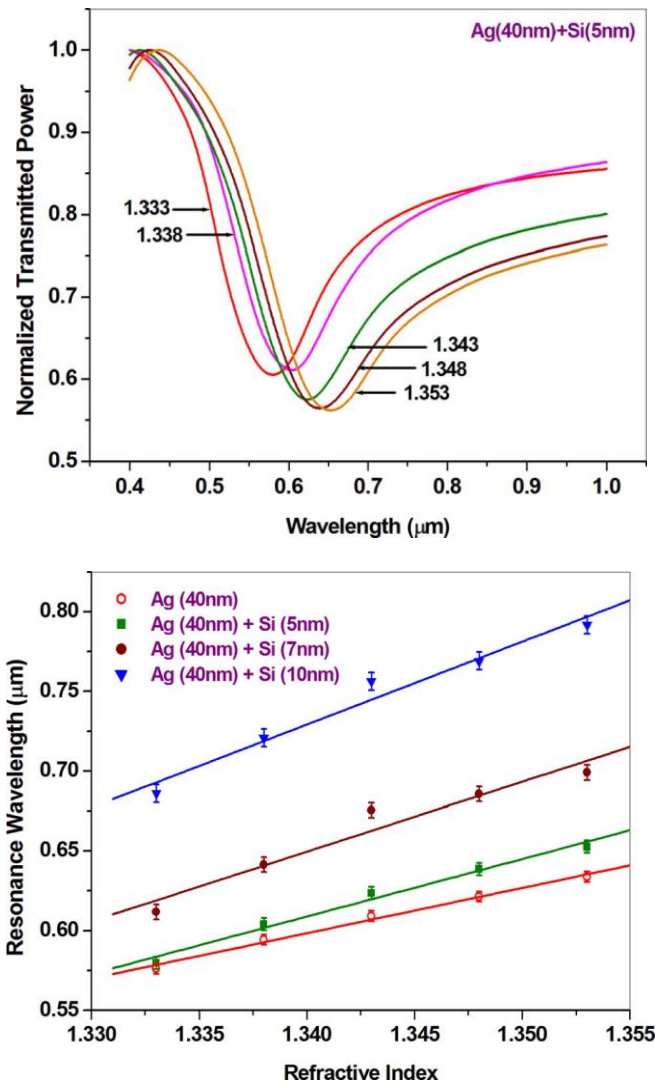

Figure 1.12. Typical results from SPR-based fiber optic refractometer [73]: a) SPR spectra with 5 nm thick silicon layer for RI variation from 1.333 to 1.353, and b) resonance wavelength shift with sensing medium index for different thickness of silicon layer.

1.2.7. Multimode interference-based refractometers

A multimode interference (MMI)-based refractometer can be realized by splicing step-index MMFs to obtain a hybrid structure consisting of an unclad MMF joint at its extremities by two clad MMFs as illustrated in Figure 1.13(a) [75]. Another possible configuration is an unclad MMF sandwiched between two single-mode fibers (SMFs) by fusion splicing shown in Figure 1.13(b) [23].

The basic principle of fiber-based MMI refractometry is based on observing or tracking the shifting wavelength which is induced by the resulting optical interference in the multimode fiber. Interference occurs when light from the lead-in SMF or smaller-diameter MMF diffracts into the larger-diameter unclad MMF. The light is then reflected by total internal reflection (TIR) several times at the outer surface of the unclad MMF and subsequently interferes at the extreme end of the unclad MMF. The resulting shifting of the output wavelength can thus be observed in the presence of variations in the surrounding medium index due to the multimode interference effects [75, 76]. A typical measurement scheme to monitor the SPR-induced shift in the wavelength is illustrated in Figure 1.13(c).

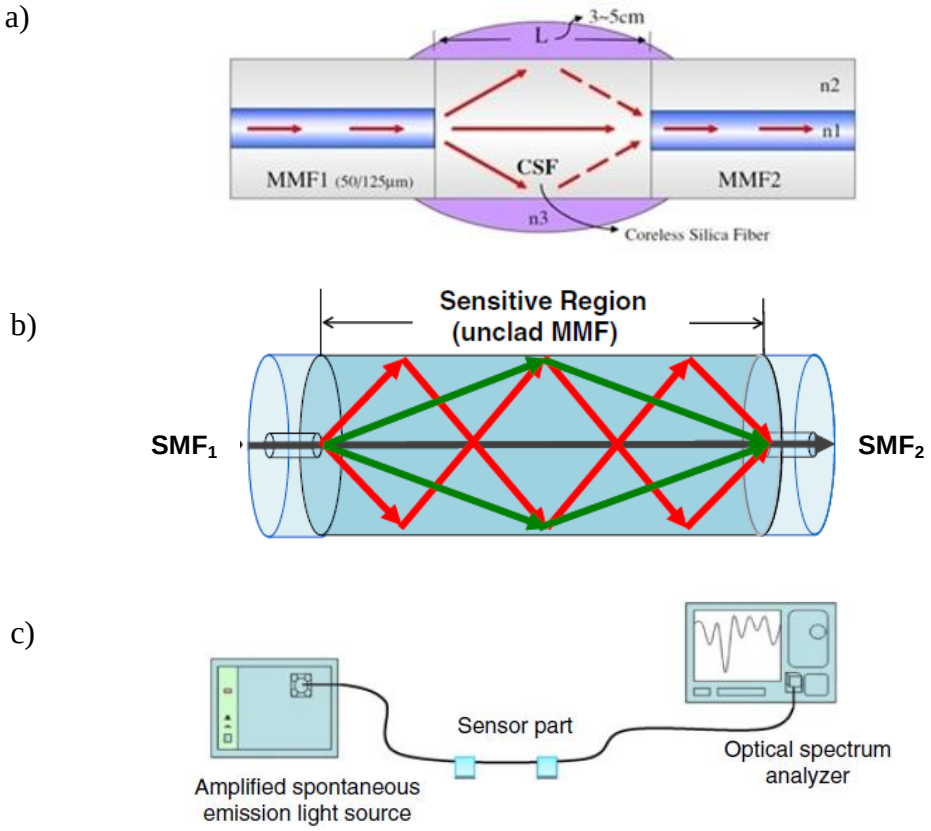

Figure 1.13. Fiber-based MMI refractometry, a) using MMF-unclad MMF-MMF structure [75], b) using SMF-unclad MMF-SMF structure [24], and c) schematic diagram of complete refractometer set-up [24].

In the SMF-unclad MMF-SMF configuration (Figure 1.13(b)), the radiated light from the lead-in or input SMF is diffracted into the MMF from which multiple modes are excited. These modes will interfere while propagated along the MMF,

subsequently resulting in a phase difference ($\Delta\phi$) between the LP_{0m} and LP_{0n} modes which can be expressed as [76]

$$\Delta\phi^{m,n} = \frac{2\pi\left(n_{eff}^{m} - n_{eff}^{n}\right)L}{\lambda} = \frac{2\pi\Delta n_{eff}^{m,n} L}{\lambda} \tag{1.3}$$

where m and n are positive integers, L is the length of the unclad MMF, $n_{eff}^{m,n}$ the effective refractive index difference between the LP_{0m} and LP_{0n} modes and λ is the free-space wavelength. Further, the wavelength spacing $\Delta\lambda$ between two adjacent minima can be determined by [76]

$$\Delta\lambda \approx \frac{\lambda^2}{\Delta n_{eff}^{m,n} L} \tag{1.4}$$

Thus, $\Delta\lambda$ will increase for decreasing length of unclad MMF. Concurrently, the variation of RI around the MMF sensing region will also modify the effective index difference between the LP_{0m} and LP_{0n} modes. This effect will induce changes in the coupling conditions between the core and cladding modes to further result in a shift of the interference fringes as illustrated in Figure 1.14.

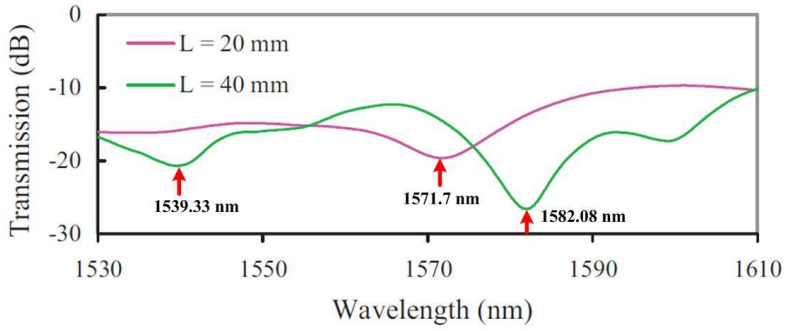

Figure 1.14. Transmission spectra for 20 mm and 40 mm sensor lengths in surrounding medium of air [76].

A spectral interference fringe for the 20 mm sensing length is observed at 1571.7 nm with 19.5 dB of power transmission, while for the 40 mm sensor, two spectral interference fringes are observed at 1539.33 nm and 1582.08 nm with power transmissions of 20 dB and 25 dB, respectively. A single-fringe signal is observed for the shorter MMF sensing length since, according to Equation (1.3), the phase difference between the guided modes is small, while the longer MMF sensor has a larger phase difference between the modes and $\Delta\lambda$ being smaller according to

Equation (1.4) [76]. Hence, more interference fringes can be observed for the longer sensor. Further, Equation (1.4) predicts that a wider interference pattern spectrum will be obtained by the shorter sensor since it induces a weaker interference fringe amplitude compared to the longer MMF, as validated by Figure 1.14.

Figure 1.15 shows the response of the longer 40-mm refractometer employed for RI measurement having a better sensitivity (187.78 nm/RIU) with a fringe shift of 6.76 nm for a dynamic range from 1.336 to 1.372 RIU. The 20-mm sensor, as a comparison, has a fringe shift of 5.72 nm which is equivalent to 158.89 nm/RIU of sensitivity. From Figure 1.15(a), when the sensor is exposed to air, resonant wavelengths at 1539.33 nm and 1582.08 nm are observed. These then shift toward the longer wavelength spectrum for increasing medium index from 1.336 to 1.372 RIU. The resulting spectral response from the 40-mm sensor is plotted in Figure 1.15(b).

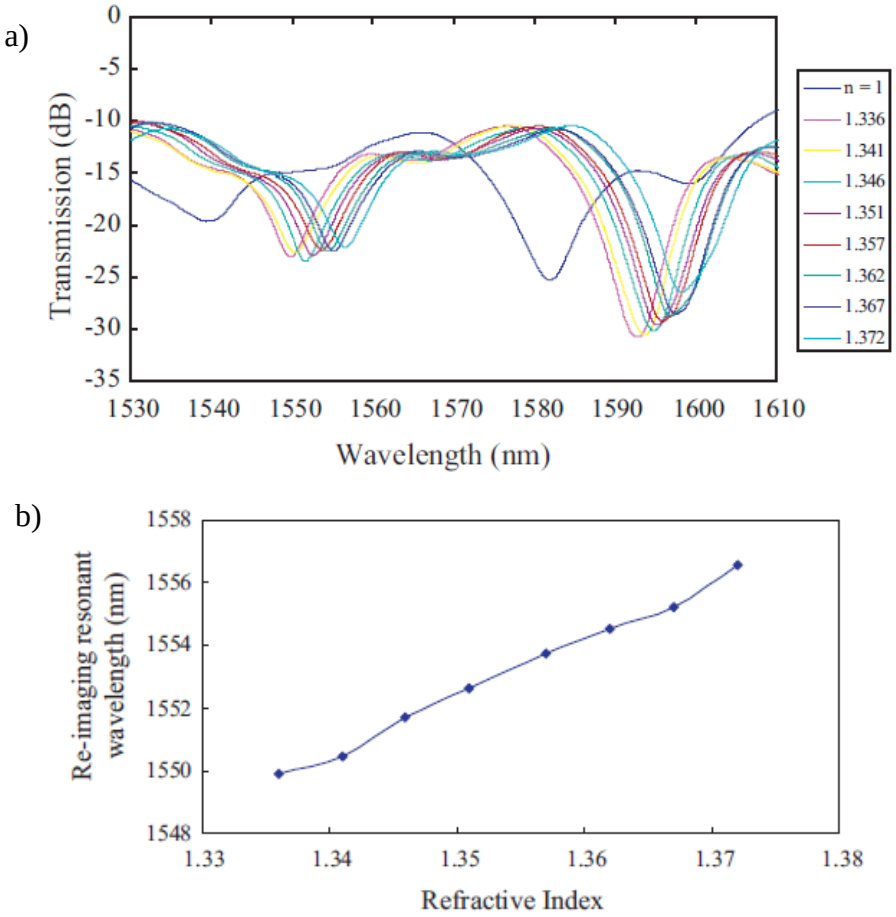

Figure 1.15. Experimental results from 40-mm MMI-based refractometer demonstrating [76] a) transmission spectra for different RIs, and b) resonant wavelength responses for different RIs.

1.2.8. Fiber Bragg grating-based refractometers

A fiber Bragg grating (FBG) is an optical fiber whose core has been subject to a periodic refractive index modulation, resulting in a grating structure being permanently inscribed in the fiber core [27]. This grating functions as a wavelength-selective reflector or optical filter hence, only a particular wavelength is reflected into a backward propagating mode or signal while the remaining wavelengths are transmitted along the fiber after the grating to result in a forward-propagating mode. The reflected wavelength, which is also called the Bragg resonance wavelength, can be expressed by [77]

$$\lambda_B = 2n_{eff}\Lambda \tag{1.5}$$

where n_{eff} and Λ are the effective modal index for the guided mode and the periodicity or pitch of the core RI modulation, respectively. Any changes to n_{eff} and/or Λ due to external perturbations will thus modify λ_B. Hence, a response to longitudinal strain and temperature variations along the FBG can be estimated as a function of the shift in the Bragg wavelength ($\Delta\lambda_B$) such that [78]

$$\Delta\lambda_B = 2\left[\Lambda\frac{\partial n_{eff}}{\partial l} + n_{eff}\frac{\partial\Lambda}{\partial l}\right]\Delta l + 2\left[\Lambda\frac{\partial n_{eff}}{\partial T} + n_{eff}\frac{\partial\Lambda}{\partial T}\right]\Delta T \tag{1.6}$$

The first term on the right of Equation (1.6) represents the strain sensitivity ($\Delta l/\Delta\lambda_B$), while the second term represents the influence of temperature variation on $\Delta\lambda_B$. Therefore, the FBG can be employed for strain as well as temperature sensing.

Under normal conditions, n_{eff} and, hence, λ_B are not influenced by the external environment since it is shielded by the cladding index. However, when the cladding is reduced or removed such as by an etching process, n_{eff} will become highly sensitive to the surrounding medium in contact with the uniform FBG. Thus, any variation in the medium index will induce a shift in λ_B as predicted by Equation (1.5). Figure 1.16(a) illustrates a typical experimental set-up employed for RI measurement in which $\Delta\lambda_B$ is detected against variation in the surrounding medium index and plotted in Figure 1.16(b) [25].

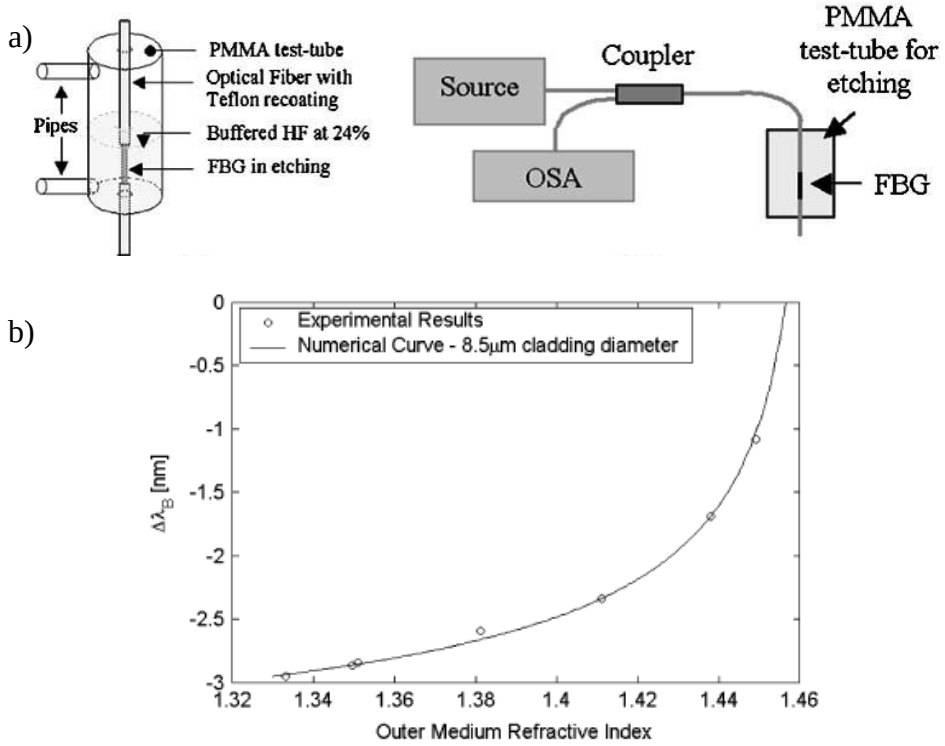

Figure 1.16. FBG-based refractometer [25]: a) schematic of experimental set-up, and b) response of Bragg wavelength shift to variation in surrounding index.

The FBG-based refractometer typically employs a broad-band superluminescent diode (SLD) operating at 1550 nm which is connected to the input arm of a directional coupler. Light is then transmitted to the sensor probe in the form of a Bragg grating which is immersed in the medium under investigation. The coupler's return arm is employed to collect the reflected spectrum from the FBG that can be subsequently analyzed by an optical spectrum analyzer (OSA) for a medium index ranging from 1.333 to 1.4547 RIU. As illustrated by Figure 1.16(b), λ_B shifts toward the shorter wavelength range for decreasing sensing medium index. This is a consequence of the diminution of n_{eff} as well as of the power of the fundamental mode. Thus, for an OSA resolution of 1 pm at 1550 nm, a potential RI resolution of the order of ~10^{-5} to ~10^{-4} RIU could be achieved [25].

1.2.9. Long-period grating-based refractometers

Fiber gratings are classified into FBGs which have a smaller uniform sub-micron grating period or pitch Λ, and long-period gratings (LPGs) which have much larger non-uniform grating periods or pitch [79]. Although FBG-based refractometers can

demonstrate attractive RI sensing characteristics, they need to be suitably configured through cladding processing and by isolating the grating from temperature and strain perturbations in order to achieve the necessary performance since under normal operation, FBGs are intrinsically insensitive to external medium index variation [80, 81]. However, processing the cladding typically reduces the fiber diameter rendering the device very thin and fragile.

LPGs, on other hand, do not require any modification to the fiber cladding since the grating structure basically couples light from the fiber core into modes in the cladding. These cladding modes are hence inherently sensitive to external index variations. As illustrated in Figure 1.17, the light coupling between the propagating core mode and the co-propagating cladding modes occurs in the gating structure. Upon satisfying the phase matching condition between the fundamental core mode and cladding mode, a resonance wavelength λ_{res} can be obtained, given by [81]

$$\lambda_{res} = (n_{co}^{eff} - n_{cl,m}^{eff})\Lambda \tag{1.7}$$

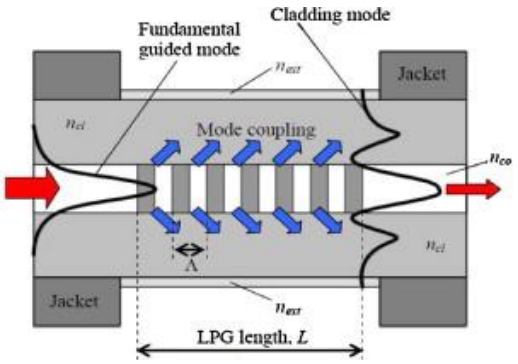

Figure 1.17. Coupling of fundamental core mode into cladding modes in LPG [81].

In the LPG, n_{co}^{eff} represents the fundamental core mode and is principally isolated against the external sensing medium index while the cladding modes, defined by $n_{cl,m}^{eff}$, are exposed to the external medium. These will thus be influenced by its index variation. The sensitivity of $n_{cl,m}^{eff}$ to external index variation, for example, of an LPG immersed in a medium (see Figure 1.18(a)), thus induces a shift in λ_{res} according to Equation (1.7). The transmission attenuation of the coupling mode is also concurrently altered, as measured experimentally in Figure 1.18(b).

a)

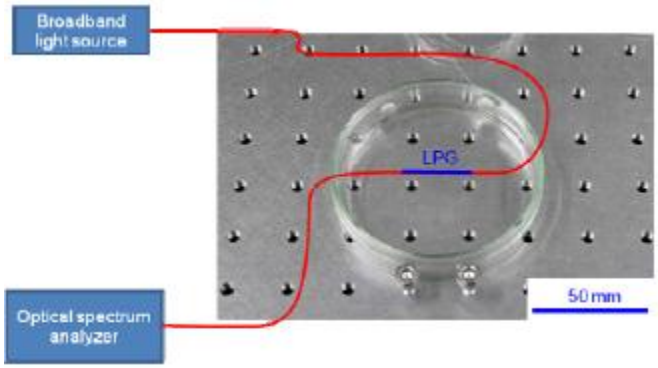

b)

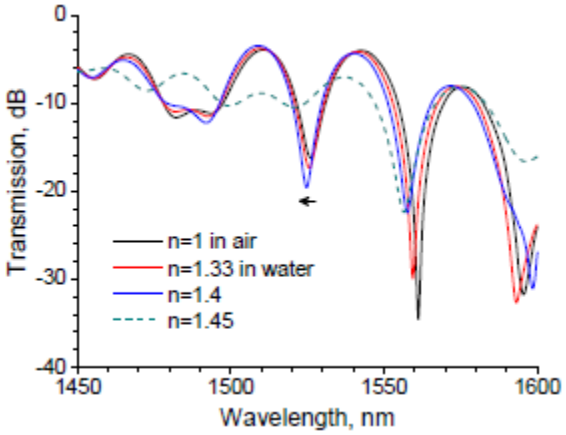

Figure 1.18. LPG-based refractometer [79]: a) experimental set-up, and b) measurement results with a 20 mm LPG sensor.

The experimental results demonstrated a shift of λ_{res} to the left by 1.4 nm (i.e. toward the lower wavelength range) for an RI variation from 1 to 1.4 RIU or equivalent to 3.5 nm/ RIU of sensitivity, coupled with an increase in the optical power attenuation for increasing index [79].

1.2.10. Fiber-tip reflection-based refractometers

A simple and cost-effective RI measurement scheme can also be performed by exploiting Fresnel reflections at the tip of an optical fiber [33, 82-84]. Due to the index difference between the fiber core and the sensing medium, which can be given by [84]

$$n_{sm} = n_{co}\frac{\left(1-10^{R_{end}/20}\right)}{\left(1+10^{R_{end}/20}\right)},\ n_{co} > n_{sm} \tag{1.8}$$

where n_{sm} and n_{co} represent the measured index and the fiber core index, respectively. Also, R_{end} is the reflected power coefficient (in dB) due to Fresnel reflections at the fiber end and can be calculated as a function of n_{co} and the air index n_a through [84]

$$R_{end} = \left(\frac{n_{co} - n_a}{n_{co} + n_a}\right)^2 \tag{1.9}$$

A simple experimental set-up illustrated in Figure 1.19(a) can typically be employed for measuring liquid RI based on Fresnel's reflection principles. Lightwave from a tunable laser source is modulated by an optical/electrical (O/E) converter. This light is transmitted via an SMF coupler to the fiber tip which is immersed in the liquid being studied. The light is then reflected at varying degrees of intensity as a function of the liquid index, as predicted by Equations (1.8) and (1.9). Simulation and experimental results are also presented in Figure 1.19(b) to illustrate the response of the fiber-tip refractometer.

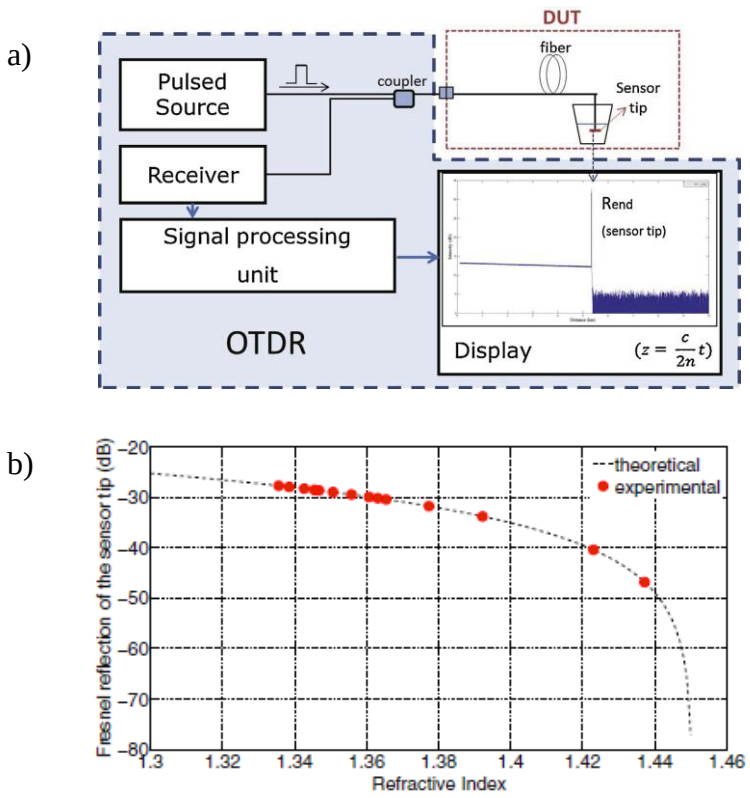

Figure 1.19. Fiber-tip refractometer based on Fresnel reflections [84]: a) experimental set-up, and b) simulation and experimental results.

Figure 1.19(b) shows very good agreement being achieved between simulation and the experimental measurements of Fresnel reflections at the fiber tip. Furthermore,

this sensor has been found to have good repeatability over three measurements, with a standard deviation of 1.7×10^{-4} RIU [84].

1.2.11. Tapered optical fiber-based refractometers

Tapering an MMF is realized by reducing the MMF diameter into a “taper waist” form. A conventional MMF can thus be "linked" to two fiber tapers through a conical tapered sector called the "taper transition", as illustrated in Figure 1.20 [34]. At the taper transition, core modes are excited into cladding modes, which could then be guided within the cladding when the surrounding medium index is lower than that of the cladding. As these cladding modes are in direct contact with the sensing medium the subsequent evanescent waves generated in the cladding can be absorbed by the sensing medium. Furthermore, since the multimode fiber-based sensing section has a smaller diameter, higher evanescent wave absorption (EWA) can be achieved thus leading to an improved sensitivity [34].

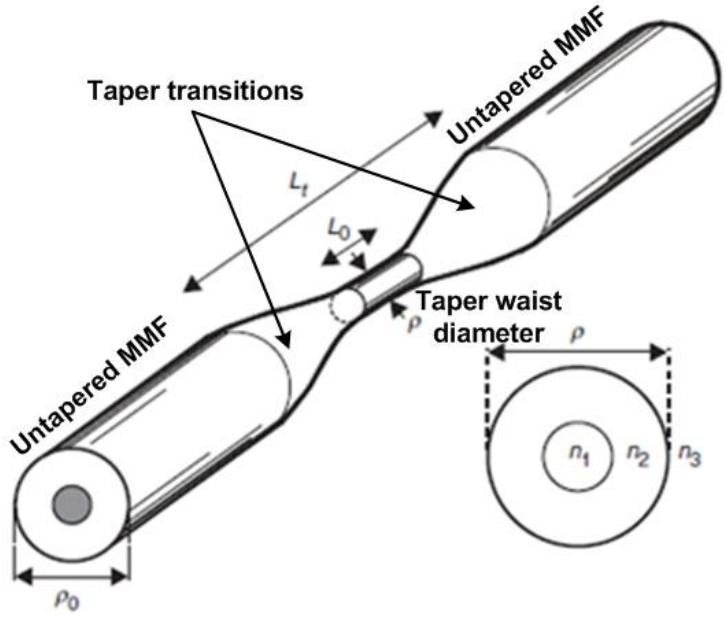

Figure 1.20. Tapered MMF [34].

Results for three different tapered-fiber waist diameters ρ with the same waist length L_0 are reproduced in Figure 1.21 showing more losses occurring for increasing medium index up to the cladding index value. In the lower index range, the smallest-diameter taper exhibits the highest sensitivity. However, for measured indices close

to the cladding index the highest sensitivity is obtained from the taper waist with the largest ρ, together with the best resolution of 10^{-4} RIU.

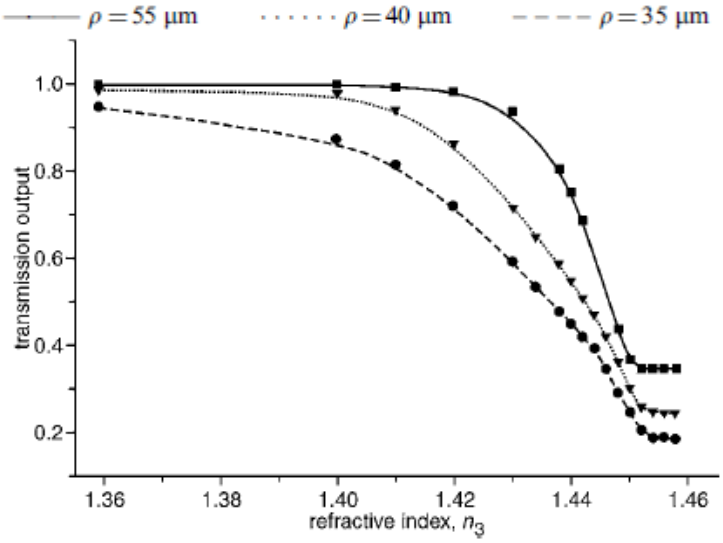

Figure 1.21. Transmission output of tapered fiber-based refractometer for three different waist diameters [34].

1.2.12. D-shaped fiber-based refractometers

These refractometers measure RIs by exploiting EWA induced at the surface of a D-shaped fiber section in contact with the target medium. Any index variation in the medium will thus result in an attenuation of the transmitted optical power or intensity [37-39, 63]. Such a fiber can be fabricated by removing the outer surface of a plastic optical fiber (POF) over a specific length up to a certain depth to form a "D-shape" section. A typical D-shaped fiber obtained by the side-polishing method is illustrated in Figure 1.22 [38].

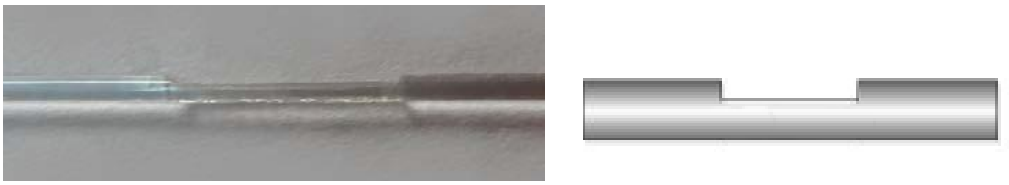

Figure 1.22. D-shaped optical fiber sensor [38].

Since the cylindrical fiber section is transformed into a D-shape, the effective V-parameter V_D for this fiber can be expressed by [38]

$$V_D = \frac{2\pi r_{eff}(d)}{\lambda}\sqrt{{n_{co}}^2 - {n_{sm}}^2} \qquad (1.10)$$

where r_{eff} represents the effective radius of the D-shaped fiber with respect to the side-polished depth of the zone, while n_{co} *a*nd n_{sm} are the core and sensing medium indices, respectively. Therefore, when n_{sm} varies, V_D will be modified according to Equation (1.10). Consequently, the optical power ratio between the power confined in the core and that penetrated into the sensing medium as evanescent fields varies with n_{sm} [38]. A typical experimental set-up for measuring RIs using a D-shaped fiber-based refractometer is illustrated in Figure 1.23(a) while Figure 1.23(b) plots the subsequent response curves (transmission loss) as a function of RI variation in the sensing medium.

a)

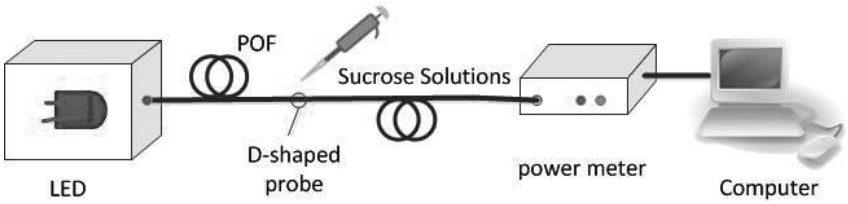

b)

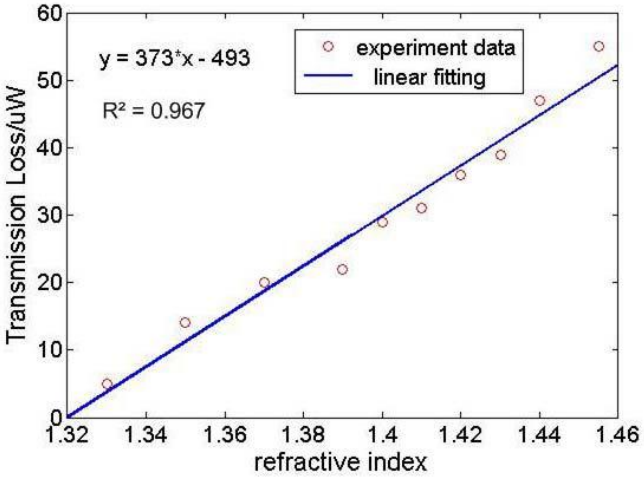

Figure 1.23. D-shaped optical fiber-based refractometer [38]: a) experimental set-up, and b) transmission loss occurring in 350 um groove depth.

The results obtained indicate that, for a sensor with a 350 µm groove depth, the optical power loss increases linearly with increasing n_{sm}. Such a response occurs since more evanescent waves penetrate into the sensing medium when its index increases, i.e. optical power is increasingly absorbed by the medium. Here, different concentrations of sucrose solutions were used to induce n_{sm} variation from 1.333 to 1.455 RIU.

1.2.13. Stripped-clad multimode fiber (MMF)-based refractometer

Refractometers based on stripped-clad multimode fiber are realized by removing a certain length of the MMF cladding as the sensitive region [36, 57-62]. This device is similar to the dielectric rod refractometer [53-55]. Typically, the refractometer employs a plastic-clad silica (PSC) fiber due to the ease in removing the cladding part using a thermal stripper as illustrated in Figure 1.24.

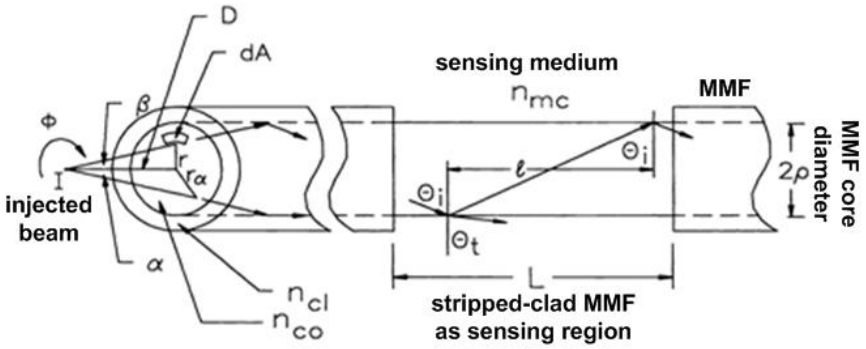

Figure 1.24. Stripped-clad MMF as the sensing region in multimode fiber refractometer [61].

The sensing region is subsequently immersed in a liquid measurand as illustrated in Figure 1.25.

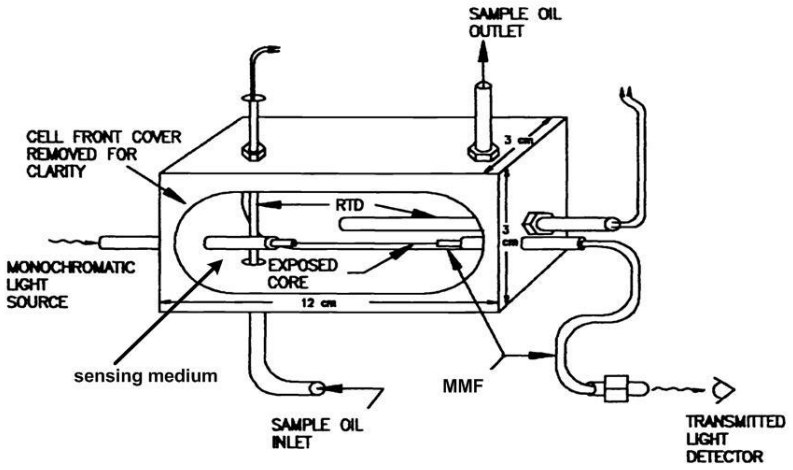

Figure 1.25. Experimental set-up to measure RI values of liquids using stripped-clad MMF [61].

Cole *et al.* propose 4 mathematical models to predict the guided power exploiting geometrical optic analysis [61]. The first model is used to calculate the guided power (P_t) along the MMF when the sensing medium index n_{sm} is lower than the cladding index n_{cl}. Hence

$$P_t = I\int_0^{2\pi}\int_0^{r_a}\frac{r\,d\phi\,dr}{D^2} = \pi I\left(\frac{r_a}{D}\right)^2 = \pi I\left(n_{co}{}^2 - n_{cl}{}^2\right) \tag{1.11}$$

where I is the light intensity, and r_a/D represents the fiber's numerical aperture for which r_a represents the outer ray radius, while D represents the outer ray hypotenuse. Further, when $n_{cl} \le n_{sm} < n_{co}$, the mathematical model to estimate P_t under this condition is influenced by mode loss due to the modified numerical aperture ($NA_{mod} = (n_{co}^2\text{-}n_{sm}^2)^{0.5}$), and the corresponding reflectivity (R) from Fresnel reflections which originate from the mode loss. The second model is represented by

$$\begin{aligned} P_t &= I\int_0^{2\pi}\int_0^{r_a}\frac{r\,d\phi\,dr}{D^2} + I\int_0^{2\pi}\int_{r_m}^{r_a}\left(\frac{r}{D^2}\right)\left[R\left(\theta_i, n_{co}, n_{sm}\right)\right]^{\frac{L}{2\rho\tan\theta_i}} d\phi\,dr \\ &= \pi I\left(n_{co}{}^2 - n_{cl}{}^2\right) + \frac{2\pi I}{D^2}\int_{r_m}^{r_a}\left(\frac{r}{D^2}\right)\left[R\left(\theta_i, n_{co}, n_{sm}\right)\right]^{N(r)} dr \end{aligned} \tag{1.12}$$

where $R(\theta_i, n_{co}, n_{sm}) = R(r, n_{co}, n_{sm})$ is reflectivity from the mode loss by Fresnel reflections as a function of r, n_{co}, and n_{sm}, while $N(r)$ represents the number of reflections along the sensitive region, given by $N(r) = L/(2\rho \tan \theta_i)$. The third model predicts the guided power along the sensor when $n_{sm} = n_{co}$, which can be expressed as

$$P_t = \pi I\left(\frac{\rho^2}{L^2}\right) \tag{1.13}$$

Here, L and ρ represent the sensing length and the MMF radius, respectively. The final or fourth model describes the power guided when $n_{sm} > n_{co}$. Under this condition, the guiding mechanism is uniquely due to Fresnel reflections, and, hence, the model can be expressed as

$$\begin{aligned} P_t &= I\int_0^{2\pi}\int_0^{r_a}\frac{r\,d\phi\,dr}{D^2} + I\int_0^{2\pi}\int_{r_m}^{r_a}\left(\frac{r}{D^2}\right)\left[R\left(\theta_i, n_{co}, n_{sm}\right)\right]^{N(r)} d\phi\,dr \\ &= \frac{2\pi I}{D^2}\int_{r_m}^{r_a}\left(\frac{r}{D^2}\right)\left[R\left(\theta_i, n_{co}, n_{sm}\right)\right]^{N(r)} dr \end{aligned} \tag{1.14}$$

Using the models in Equations (1.12), (1.13) and (1.14), simulations have been realized and validated experimentally as illustrated in Figure 1.26.

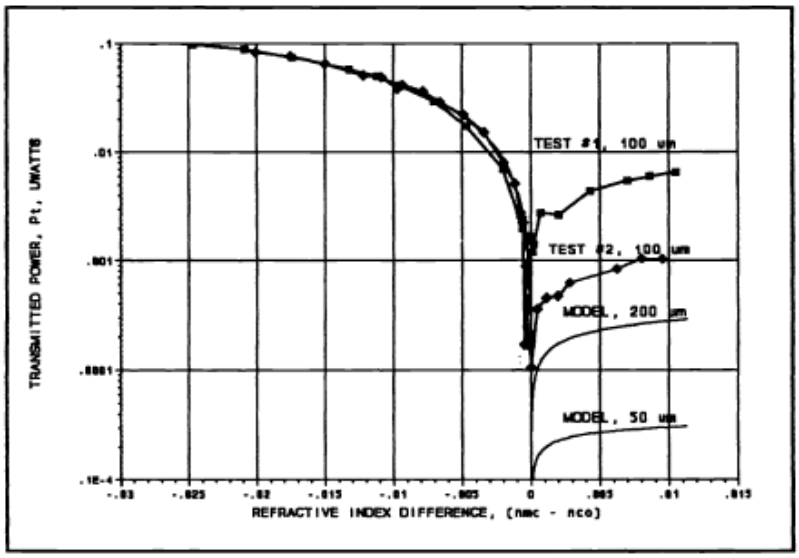

Figure 1.26. Simulation and experimental results from a stripped-clad MMF refractometer [61].

When $n_{cl} \leq n_{sm} < n_{co}$, good agreement is obtained between the experimental and simulation results. However, when $n_{sm} > n_{co}$ a relatively high discrepancy occurs between simulation and experiment. In addition, the first model in Equation (1.11) predicts that when $n_{sm} < n_{cl}$, the guided power does not change with varying n_{sm}. In this study [61] as well as in another by Arie *et al.* [57-59], the models proposed, in particular the first and second models, did not consider evanescent wave absorption. Nevertheless, under this condition ($n_{sm} < n_{cl}$), evanescent waves exist since the lightwaves propagate along the MMF by total internal reflection (TIR). These evanescent waves will be absorbed by the sensing medium, and, hence, will contribute to the reduction in the guided optical power along the MMF.

In this thesis, therefore, 3 functional and accurate models will be developed to estimate the power response in MMF-based as well as in photonic crystal fiber (PCF)-based refractometers. Here, the mathematical models will exploit a combination of the ray optics approach, Gaussian beam analysis, and the EWA-related analytical equation. Ray optics is used in a similar manner to previous studies [57, 58] since it can represent the mode loss phenomenon for increasing n_{sm}. Gaussian beam analysis, on the other hand, is employed to accurately analyze the injected optical power distribution into the MMF. This thesis will therefore strive to reinforce existing work in MMF refractometry, for example that by Arie *et al*. who

proposed a relatively accurate approximation to determine the injected optical power distribution, albeit for beams launched from a lens system. In addition, Gaussian beam analysis can be employed for any launch conditions, i.e. for coupling condition using a lens through beam coupling from an SMF. The analytical equation of EWA is also employed since the propagation modes in the MMF occur principally by TIR, resulting in the generation of evanescent waves. Therefore, EWA must be considered to comprehensively describe the power response in the MMF as well as the PCF refractometers.

1.3. Comparison and conclusion

Refractometers based on prism optic are typically used for measuring the RI of sample media in the laboratory. They cannot, however, be used for continuous *in situ* measurements over long periods. For *in situ* and remote measurements, optical fiber-based refractometers are the most suitable alternative and can be divided into broad categories, those based on spectral interrogation and intensity measurement, respectively. Table 1.1 below gives a brief comparison of optical fiber refractometers exploiting spectral-based measurements.

Table 1.1. Optical fiber refractometers based on spectral measurements with OSAs having a typical resolution of ~1 pm.

Type of refractometer	**Cost**	**Fabrication difficulty**	**Resolution (RIU)**	**Dynamic range (RIU)**
SPR-based [18, 19, 73]	+++	+++	4×10^{-6} [18] 6.25×10^{-7} [19] 1.92×10^{-7} [73]	1.5375 - 1.5515 [18] 1.3353 - 1.3653 [19] 1.333 - 1.353 [73]
MMI-based [23, 24, 76]	++	+	6×10^{-6} [23] 6.8×10^{-6} [24] 5.32×10^{-6} [76]	1.33 - 1.36 [23] 1.33 - 1.36 [24] 1.336 - 1.372 [76]
FBG-based [25, 26, 28]	++	++	10^{-5} [25] 1.4×10^{-6} [26] 1.4×10^{-4} [28]	1.333 -1.4547 [25] 1 - 1.378 [26] 1.324 - 1.439 [28]
LPG-based [31, 79]	++	++	7.69×10^{-5} [31] 1.92×10^{-4} [79]	1.404–1.452 [31] 1.33 - 1.45 [79]

Optical fiber refractometers based on spectral measurements enable to measure RI variations by observing the spectrum shift using an OSA, a spectrometer, or by OTDR which are relatively costly. In terms of performance, the fiber SPR-based refractometer can offer very high resolution in the order of 10^{-7} RIU, but is limited by a relatively narrow dynamic range. This refractometer is also more complicated to realize since it requires the deposition of a very thin metal layer (nanometric range) as the sensing element. On the contrary, the refractometer based on MMI is very easy to fabricate and can be made to achieve a good resolution in the order of 10^{-6} RIU, although the dynamic range is still relatively narrow. Refractometers based on FBGs and LPGs, on the other hand, allow exploiting a larger dynamic range coupled with a relatively good resolution.

However, more competitive and cost-effective optical fiber refractometers can be realized using intensity-based measurement which does not require expensive interrogating instruments for measuring the optical spectrum. Table 1.2 summarizes some widely-used refractometers based on intensity measurement.

Table 1.2. Optical fiber refractometers based on intensity measurement.

Type of refractometer	**Cost**	**Fabrication difficulty**	**Resolution (RIU)**	**Dynamic range (RIU)**
Fiber-tip reflection [82-84]	+	+	2.5×10^{-5} [82] 3.28×10^{-5} [83] 1.7×10^{-4} [84]	1.3296 - 1.453 [82] 1.3486 - 1.4525 [83] 1.33 - 1.45 [84]
Tapered optical fiber [34, 35]	+	++	10^{-4} [34] 6×10^{-3} [35]	1.36 - 1.45 [34] 1.33 - 1.492 [35]
D-shaped optical fiber [37, 38]	+	+	6.48×10^{-3} [37] 10^{-3} - 10^{-4} [38]	1.332 - 1.471 [37] 1.33 - 1.455 [38]
Stripped cladding optical fiber [36, 85]	+	+	10^{-1} - 10^{-4} [36] 10^{-3} - 10^{-5} [85] (10^{-6})	1.33 - 1.56 [36] 1.31 - 1.61 [85]

Typically, optical fiber refractometers based on intensity measurement are less costly, relatively simple to fabricate, and can achieve relatively good resolution with a large dynamic range, as presented in Table 1.2. These resolutions, however, are not

sufficient to enable detection of 1 nmol/L of dissolved methane (CH_4) in water, for example, since as reported by Boulart *et al.*, the RI variation as a function of dissolved CH_4 concentration has a linear relation with a sensitivity of 5.5×10^{-6} RIU/nM CH_4. Hence, to be capable of measuring 1 nM (1nmol/L) CH_4, a refractometer with a resolution of at least of 5.5×10^{-6} RIU is necessary [86].

In this thesis, therefore, stripped cladding and/or stripped coating optical fibers will be further studied for their geometrical flexibility, cost effectiveness, large dynamic range together with a relatively good overall performance. Furthermore, as will be demonstrated in this work, the resolution achieved for a stripped cladding fiber refractometer developed has been increased to 10^{-6} RIU order, thus potentially allowing CH_4 concentrations down to 1 nmol/L in water to be detected.

CHAPTER II

Stripped-cladding Multimode Fiber-based Refractometer

2.1. Introduction

A large variety of refractive index (RI) sensors or refractometers exploiting different measurement techniques have been reported since the first Abbé refractometer designed by Ernest Abbé at the end of the 19th century [65]. Their popularity, which generates a significant level of commercial viability over the past few decades, is due to their wide-ranging application potential in chemistry and physics, in environmental monitoring, as well as across the biochemical, pharmaceutical, and the food and beverage industries [2, 3]. Amongst these RI sensors, a multitude of optical fiber refractometers (OFRs) has also been developed for their intrinsic advantages, such as robustness to relatively harsh ambient conditions, non-cumbersome size, explosion-free security since no on-probe electrical power is necessary, relatively rapid real-time in-situ measurement for remote sensing, multiplexing potential, and immunity to electromagnetic interference (EMI) [2-5].

One RI measurement method which is widely exploited is the optical intensity-based refractometer [53-63] due to its simplicity and cost effectiveness. In such a device, the variation in RI value will induce a variation in the optical power or intensity to be measured. OFR techniques based on optical intensity modulation have been realized using tapered multimode fibers (MMFs) [34, 35], back-reflection fiber core tips [33, 82-84], dual MMF configurations similar to the fiber bundle proximity sensor [87-89], D-shaped multimode plastic optical fibers [37-39, 63], and stripped-cladding MMFs [36, 57-62].

Development of the stripped-cladding MMF refractometer has been reported since the 1980's [57-60], inspired by a dielectric rod refractometer immersed in a liquid which was used as the equivalent cladding [53-55]. Various models of the stripped-cladding MMF refractometer have been proposed and are based on the estimation of their optical power response measured against the RI variation with respect to the

fiber core index [57-61]. In these early refractometers, Snell's law and Fresnel's reflection law were employed to interpret the sensor response for measured indices lower than that of the core while only Fresnel reflections were employed when the indices were higher than the core index. Although previous models [58, 59] attempted to determine and take into account the power distribution density of the incident beam, the influence of evanescent wave absorption (EWA) was, however, not considered. Nevertheless, EWA exists since the beams or rays are essentially guided by total internal reflection (TIR). In addition, the resulting approximation from these existing models was sufficiently precise only when applied to a beam launched through a lens system [58, 59].

We propose, in this chapter, an alternative Gaussian beam analysis method to accurately estimate the optical power distribution density of the laser beam launched from a microscope objective (MO) into an MMF. This method achieves a good estimation of the power response of stripped-cladding MMF refractometers. Consequently, it is necessary to incorporate Gaussian beam optic analysis into the model describing an incident beam distribution launched into an MMF from a single-mode (SM) laser source. Although experimentally validated for beam injections or launching via an MO in this chapter, this method can also be extended to deal with other launch conditions, including that from a single-mode fiber (SMF) spliced to an MMF which will be discussed in the next chapter (Chapter III). As a result, a functional and accurate model has been developed in this work and will be detailed in this chapter. It clearly identifies and defines three distinct sensing regions (or RI zones) through different sensing mechanisms and their subsequent responses to RI variations. Typically, the first zone (Zone I) describes the sensing mechanism uniquely attributed to EWA for an external or sensing medium index (n_{sm}) inferior to the cladding index (n_{cl}) while the second zone (Zone II) corresponds to combined contributions from EWA and mode power loss due to the number reduction of propagating modes for $n_{cl} \leq n_{sm} \leq n_{co}$ (core index). Note that the typical RI boundary between Zone I and Zone II given as n_{cl} is still valid when the injected beam angle (β_b) is higher than or equal to the MMF's acceptance angle (β_{MMF}). However, for $\beta_b < \beta_{MMF}$, the RI boundary between Zone I and Zone II will transform into an equivalent

index (n_b) with respect to θ_b ($n_b = n_{co} \sin\theta_b$). In the third and final zone (Zone III), the power response is due uniquely to Fresnel reflections when the measured index is higher than the core index ($n_{sm} > n_{co}$).

The model thus proposes the integration of Snell's law, Fresnel reflections and EWA into a complete inter-dependent relationship, and is developed using a combination of Gaussian beam principles, ray optics, and wave optic analysis to comprehensively describe the optical power response across the three sensing zones of an MMF-based refractometer. The use of Gaussian beam analysis enables to fully characterize the launching conditions at the input end of the MMF, while wave optic analysis can accurately describe and, hence, predict the absorption characteristics of the evanescent waves. Both Gaussian beam and wave optic principles are subsequently employed to reinforce ray optic analysis of the propagating modes in the MMF, leading to a highly accurate and robust model. The model is then experimentally validated in terms of the optical power response over a broad range of RI values.

2.2. Theory of propagation in multimode fibers

A lightwave or laser beam is propagated in an optical fiber by TIR which occurs as the beam injected into the fiber core is incident at the core-cladding interface at an angle higher than the critical angle. This critical angle, θ_c, can be explained by Snell's law as a function of the RI contrast between the core index (n_{co}) and the cladding index (n_{cl}), respectively, as follows:

$$\theta_c = \sin^{-1}\left(\frac{n_{cl}}{n_{co}}\right) \tag{2.1}$$

For a single-mode fiber (SMF), only one mode propagates in the fiber. On the contrary, in an MMF numerous modes can propagate. The propagating modes are modes that are incident at the core-cladding interface with an angle comprising between θ_c and 90^o. Theoretically, the number of modes (M) for a very large number of modes in a step-index MMF can be estimated by [90]

$$M \cong \frac{V^2}{2} \tag{2.2}$$

where V is an all-important parameter known as the normalized frequency for determining whether an optical fiber is single or multi mode. For $V \leq 2.405$, the fiber will be single-mode while an MMF has a V-parameter greater than 2.405. The value of V is related to n_{co}, n_{cl}, the fiber core radius (a), and the wavelength (λ) of the injected beam via

$$V = \frac{2\pi a}{\lambda}\sqrt{n_{co}^{\,2} - n_{cl}^{\,2}} \tag{2.3}$$

where $\sqrt{n_{co}^{\,2} - n_{cl}^{\,2}}$ is also known as the numerical aperture (NA) of the fiber. NA defines the acceptance angle within which an injected beam can be propagated or radiated by the fiber. Hence, to excite all the modes over the entire possible acceptance angle, the injected beam must be matched to the NA of the step-index MMF.

2.2.1. Sensing mechanism and modeling in Zone I

Consider the case of the sensing medium having an RI value (n_{sm}) less than the cladding RI (n_{cl}). Under this condition, all the modes propagate in the fiber core up tothe sensing zone by the phenomenon of TIR as shown in Figure 2.1(a).

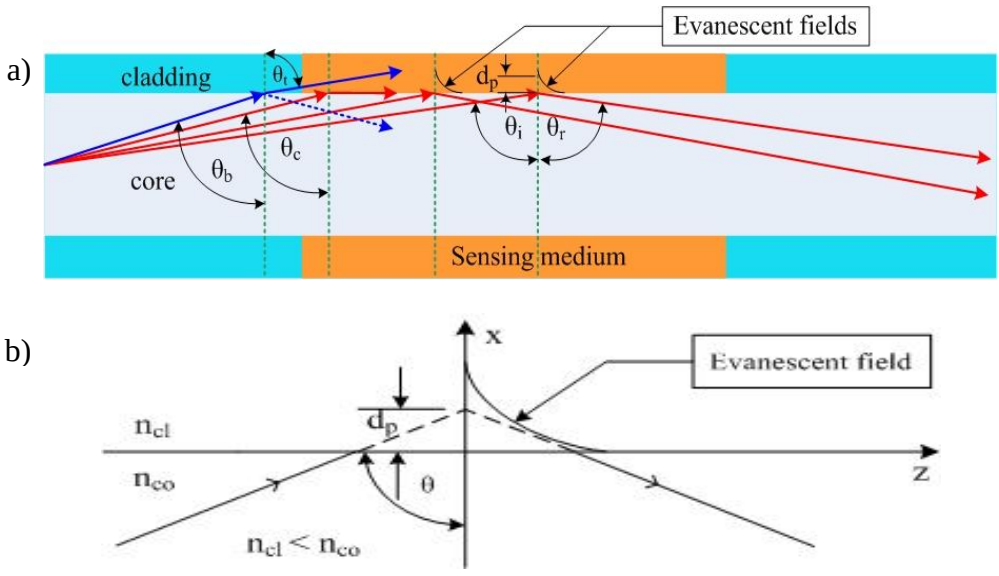

Figure 2.1. Propagation by TIR in an MMF: a) for incident lightwave angles θ_i larger than critical angle θ_c, and b) evanescent wave generated at the core-cladding interface and penetrating into the cladding when TIR occurs along the MMF [91].

At this point, evanescent waves will be generated along the core-cladding interface, as illustrated in Figure 2.1(b) and penetrates into the cladding up to a depth (d_p) given by [92]

$$d_p = \frac{\lambda}{2\pi\sqrt{{n_{co}}^2 \sin^2\theta - {n_{cl}}^2}} \tag{2.4}$$

When the incident beam angle (θ_b) is larger than θ_c, almost all power is confined within the core while the previously transmitted part of the beam propagates as evanescent waves penetrating into the cladding. Hence, the resulting power transmitted to the fiber end while propagating over a stripped cladding of length, L, can be estimated by [93]

$$P_L = P_0 e^{(-\gamma L)} \tag{2.5}$$

where γ is the attenuation coefficient of the evanescent wave and P_0 the initial power propagated by TIR in the MMF. For a weakly guiding fiber, i.e. for a fiber with only a small RI difference between the cladding and core, γ is a function of the bulk absorption coefficient (α) and the fractional power in the cladding and core (r), i.e. the ratio of the power in the cladding to the total power, given by [93]

$$\gamma = r\alpha \tag{2.6}$$

Now, r can be estimated by a simple equation related to the number of modes (M) using [93]

$$r = \frac{4}{3}\sqrt{M} = \frac{4\sqrt{2}}{3V} \tag{2.7}$$

Nevertheless, since the MMF is generally a non-weakly guiding fiber, γ thus has to be re-defined to account for the number of modes with a transmission coefficient (T) penetrating into the cladding over a number of reflections per unit length (N) as a function of the critical angle of the sensing medium ($\theta_{csm} = sin^{-1}(n_{sm}/n_{co})$) in replacement of the cladding and θ_b for $\theta_b > \theta_c$ [93] such that

$$\gamma(\theta_i) = N(\theta_i)T(\theta_i) \tag{2.8}$$

where

$$N(\theta_i) = \frac{\cot \theta_i}{2a} \tag{2.9}$$

$$T(\theta_i) = \frac{\alpha \lambda n_{co} \cos \theta_i}{\pi n_{sm}{}^2 \cos^2 \theta_{csm} \sqrt{\cos^2 \theta_{csm} - \cos^2 \theta_i}} \tag{2.10}$$

Further, by adopting Equations (2.8), (2.9), and (2.10) to solve Equation (2.5) for non-weakly guiding fibers, the power over a sensing length, L, can be calculated as a function of the angle over all the acceptance angles (θ_b, $\pi/2$) as

$$P_L = \int_{\theta_b}^{90^\circ} P_0(\theta_i) e^{(-N(\theta_i)T(\theta_i)L)} \, d\theta_i \tag{2.11}$$

Moreover, due to the comparatively low power transmission loss in the MMF over a length of ~80 cm, the absorption effect by the fiber cladding is assumed to be negligible (attenuation ~0.028 dB/m from manufacturer's datasheet [94]). Hence, the initial power can be taken as the combined power of all the rays launched into the fiber under TIR as shown in Figure 2.2.

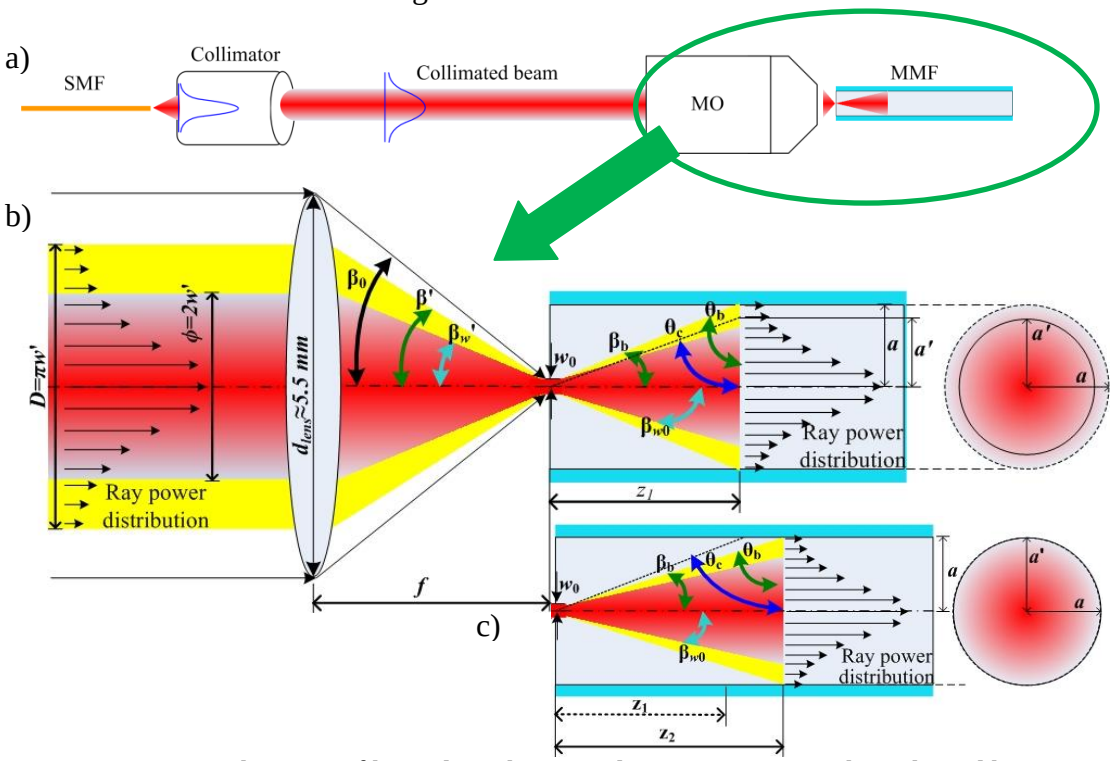

Figure 2.2. Schematic of beam launching conditions into MMF where the red beam represents the portion of the beam which transmits ~86% of the total power (or $1/e^2$ beam intensity) and which is used to determine the spot size radius (w_0), while the yellow beam represents over 99% of the total beam power. a) Collimated beam from lead-in SMF with Gaussian power distribution is focused by MO into the MMF for more specific launch parameters when b) $\theta_b < \theta_c$ of the fiber and when c) $\theta_b > \theta_c$ of the fiber.

The single-mode Gaussian beam from the SMF is collimated by an F220FC-1550 collimator to a beam diameter ($\phi = 2w'$) [95] of 2.1 mm (red beam in Figure 2.2(b) to the left of the lens) while the diameter of the total beam power can be calculated by $D = \pi w'$ [96]. This collimated beam (consisting of both the red and yellow beams) is next focused by an MO with NA = 0.65 to match all possible acceptance angles for propagation in the MMF. The beam waist (w_0) can be estimated by Equation (2.12) below which relates λ, the focal length of MO (f), and the spot radius of the collimated beam (w') in the form [90]

$$w_0 = \frac{\lambda f}{\pi w'} \tag{2.12}$$

As illustrated in Figure 2.2(b), when the total lens area of the MO is completely illuminated by the input collimated beam, the injection angle $\beta' = \beta_0$, can be obtained from the relationship $NA = n_{air}\ sin\ \beta_0$. However, since the input beam does not illuminate the entire lens area due to the lens diameter ($d_{lens} \approx 5.5$ mm) being larger than the total beam diameter ($D = \pi w' = 3.2987$ mm [96]), β' cannot, consequently, be calculated directly using the NA equation which gives a β_0 value of ~40.54°. By simplifying MO to a one-lens system, f can first be obtained using Equation (2.13) relating β_0 to the lens radius ($r_{lens} = 0.5d_{lens}$), after which β' can then be obtained for a given D value via Equation (2.14)

$$f = r_{lens} \cot \beta_0 \tag{2.13}$$

$$\beta' = \tan^{-1}\left(\frac{0.5D}{f}\right) \tag{2.14}$$

In ray optics, mode propagation in the MMF is represented by individual rays at specific angles injected into and, subsequently, propagating in the fiber, and can thus be simply analyzed by considering the beam with an incident θ_i at the core-cladding interface. Rays which have incident angles less than θ_c of the fiber will not be propagated in the core, when compared to rays with angles greater than θ_c. These latter rays will be guided in the core by TIR. To simplify the propagation model, the incident beam characteristics illustrated in Figures 2.2(b) and 2.2(c) are analyzed. The beam with a propagating angle β_b in the MMF will arrive at the core-cladding interface at a distance z_i, calculated using

$$z_i = a \cot \beta_b \tag{2.15}$$

where β_b (= 90°-θ_b) is related to β' by Snell's law via $n_{air} sin\ \beta' = n_{co} sin\ \beta_b$ and i = 1 or 2. The incident Gaussian beam can be represented as a set of rays with different individual optical power values exhibiting a Gaussian distribution, where the outer rays have a lower power density than the rays towards the center fiber axis. However, since the onset of TIR starts at z_i, the diffraction effects of the Gaussian beam are annulled at z_i [97]. Thus the power distribution for each angle of the individual rays propagated along the MMF follows on from the ray power distribution at point z_i, as will be explained below. Consequently, the sensing region must be placed after the point z_i. Then, by using Equation (2.15) and considering that the beam is injected into the center of the fiber core with a = 100 µm, for a 1 cm sensing length, the beam will be incident at the interface of the sensing area at least once up to θ_i = 89.427°. Hence, almost all of the rays injected will reach the sensing region. Further, for a Gaussian beam injected from air and expanded in the fiber core (silica with n_{co} = 1.444), the beam spot radius at z_i (w_{zi}) can be calculated by [96]

$$w_{zi}(z) = w_0 \sqrt{1 + \left(\frac{\lambda z_i}{n_{co} \pi w_0^{\ 2}} \right)^2} \tag{2.16}$$

The optical intensity at z_i (I_{zi}) and the normalized optical power injected into the fiber (P_{inj} in a.u.) can respectively then be given by [90, 96]

$$I_{z_i}(a) = I_0 e^{\left(\frac{-2a^2}{w_{z_i}^{\ 2}} \right)} \tag{2.17}$$

$$P_{inj}(a) = 1 - e^{\left(\frac{-2a^2}{w_{z_i}^{\ 2}} \right)} \tag{2.18}$$

Subsequently, as illustrated in Figure 2.2(b), when θ_b is lower than θ_c of the fiber, the total power arrives at the core-cladding interface at the point z_1. Only the optical power between θ_b and θ_c will exit the core while the remaining power will still be guided in the fiber core by TIR. This power is represented as the beam with a radius a' which can be calculated by simple trigonometry as

$$a' = z_i \cot \theta_c \tag{2.19}$$

Substituting the new radius a' into Equation (2.18) then allows P_0, the normalized power guided by TIR for $\theta_b < \theta_c$ of the fiber, to be obtained as

$$P_0(a) = 1 - e^{\left(\frac{-2a'^2}{w_{z_i}{}^2}\right)} \tag{2.20}$$

However, if $\theta_b > \theta_c$, all the incident beams arriving in the sensing region are reflected by TIR. Thus, for this condition, $a' = a$ and $P_{inj} = P_0$. Equation (2.20) must then employ $z_i = z_2$ (see Figure 2.2(c)), and w_{zi} takes on w_{z2}. Since the surface of the MO lens is not entirely illuminated by the collimated beam (c.f. $d_{lens} \approx 5.5$ mm and $D \approx 3.2987$ mm), θ_b can be obtained by applying Equations (2.13), (2.14) and Snell's law. Here, $\theta_b = 71.57°$ is higher than θ_c (70.60°), thus all injected beams are guided by TIR. Consequently, the limit of Zone I is the RI value (n_b) which is equivalent to the angle of the incident beam (via $\theta_b = sin^{-1}(n_b / n_{co})$). Further, $w_{z2} = 67.898$ µm is obtained via Equation (2.16) for the point $z_2 = 300.14$ µm while $w_0 = 1.51$ µm is obtained using Equation (2.12). Then, to solve Equation (2.11), P_0 in Equation (2.20) can be discretized into individual ray powers between θ_b and 90° (i.e. $P_0(\theta_b, \pi/2)$) at the point z_2 by varying a' in discrete steps (from 100 µm to 0) corresponding to the θ_i value for each ray. Substituting these step variations of a' into Equation (2.20) then allows the decremental power difference, $P_0(\theta_b, \pi/2)$, to be calculated for each individual ray with a corresponding set of $T(\theta_b, \pi/2)$ and $N(\theta_b, \pi/2)$ parameters. Finally, these powers are integrated over θ_b - 90° in Equation (2.11) to obtain the total transmitted power (P_L) subject to EWA for a given sensing length L.

2.2.2. Sensing mechanism and modeling in Zone II

For the second operating condition or Zone II response, where the RI of the sensing medium (n_{sm}) lies between the cladding RI and the core RI (i.e., $n_{cl} < n_{sm} < n_{co}$), two optical phenomena are concurrently influencing the optical power loss (see Figure 2.3) through (1) reduction of the number of propagation modes due to the modification of the critical angle (from θ_c to θ_{csm}) upon variation of n_{sm} and (2) EWA since TIR is always present in this operating zone, identical to the explanation of losses described for Zone I.

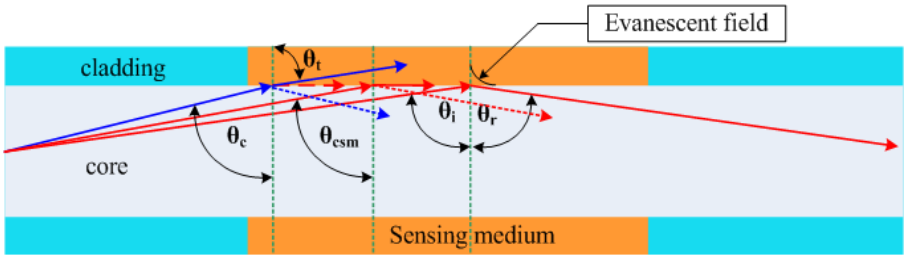

Figure 2.3. Illustration of sensing mechanism in Zone II.

As illustrated in Figure 2.3, the sensing mechanism originates from the combined contribution of both EWA and mode power loss by the modification of the critical angle (θ_{csm}). Under initial conditions, the blue line represents the mode propagated in the MMF by TIR at critical angle. However, when n_{sm} increases, θ_c is modified to θ_{csm} and this mode will be transmitted through the medium and lost to the exterior. The remaining rays incident at an angle greater than the new θ_{csm} will be guided in the MMF by TIR and concurrently subject to EWA. The reflection at the sensing medium-air interface is negligible since the medium thickness is typically more than 20 times the core diameter in addition to its strong absorption at 1550 nm. The dotted blue and red lines represent very weak Fresnel reflections off the core-medium boundary. Hence, the model of the power response for Zone II can mathematically be expressed by

$$P_L = \int_{\theta_{csm}}^{90^\circ} P_0(\theta_i) e^{(-N(\theta_i)T(\theta_i)L)}\, d\theta_i + \int_{\theta_b}^{\theta_{csm}} P_0(\theta_i) R(\theta_i)^{N(\theta_i)L}\, d\theta_i \tag{2.21}$$

The first term on the right side of Equation (2.21) describes the power response of the sensor which is induced by EWA for guided modes by TIR from θ_{csm} to 90°, while the second term corresponds to the influence of Fresnel reflections. Here, R represents the reflectivity of the rays from θ_b to θ_{csm}, and can be calculated as a function of the reflectance under both *p*-polarization (r_p) and *s*-polarization (r_s), respectively, as [90]

$$R(\theta_i) = \frac{1}{2}(r_p^{\,2} + r_s^{\,2}) \tag{2.22}$$

for which the reflectances of the respective polarizations are given by

$$r_p(\theta_i) = \frac{n_{sm}\cos\theta_i - n_{co}\cos\theta_t}{n_{sm}\cos\theta_i + n_{co}\cos\theta_t} \tag{2.23}$$

$$r_s(\theta_i) = \frac{n_{co}\cos\theta_i - n_{sm}\cos\theta_t}{n_{co}\cos\theta_i + n_{sm}\cos\theta_t} \tag{2.24}$$

where θ_t is the transmitted angle which is obtained by Snell's law as

$$\theta_t = \sin^{-1}\left(\frac{n_{co}\sin\theta_i}{n_{sm}}\right) \tag{2.25}$$

However, the contribution from Fresnel reflections in Zone II is very weak due to a high total number of reflections (*NL*) along the sensor, as well asa relatively small index contrast between n_{sm} and n_{co}. Hence, these reflections can be neglected. Subsequently, the model for Zone II in Equation (2.21) can be simplified using only the left term on the right of the equation to

$$P_L = \int_{\theta_{csm}}^{90^\circ} P_0(\theta_i) e^{(-N(\theta_i)T(\theta_i)L)}\, d\theta_i \tag{2.26}$$

According to Equation (2.26), propagation by TIR still occurs for rays with incident angles from θ_{csm} to 90°. Therefore, in Zone II, a reduction in the number of propagation modes occurs for increasing n_{sm} since the critical angle also increases as

$$\theta_{csm} = \sin^{-1}\left(\frac{n_{sm}}{n_{co}}\right) \tag{2.27}$$

This leads to a decrease in the guided power by TIR (P_0) as the beam radius a' at point z_2 decreases (see Equation (2.20)), subsequently reducing the sectional area at this point as illustrated by Figure 2.4. The beam radius, a', is here calculated by using the following relation:

$$a' = z_2 \cot\left(\sin^{-1}\left(\frac{n_{sm}}{n_{co}}\right)\right) = z_2 \cot\theta_{csm} \tag{2.28}$$

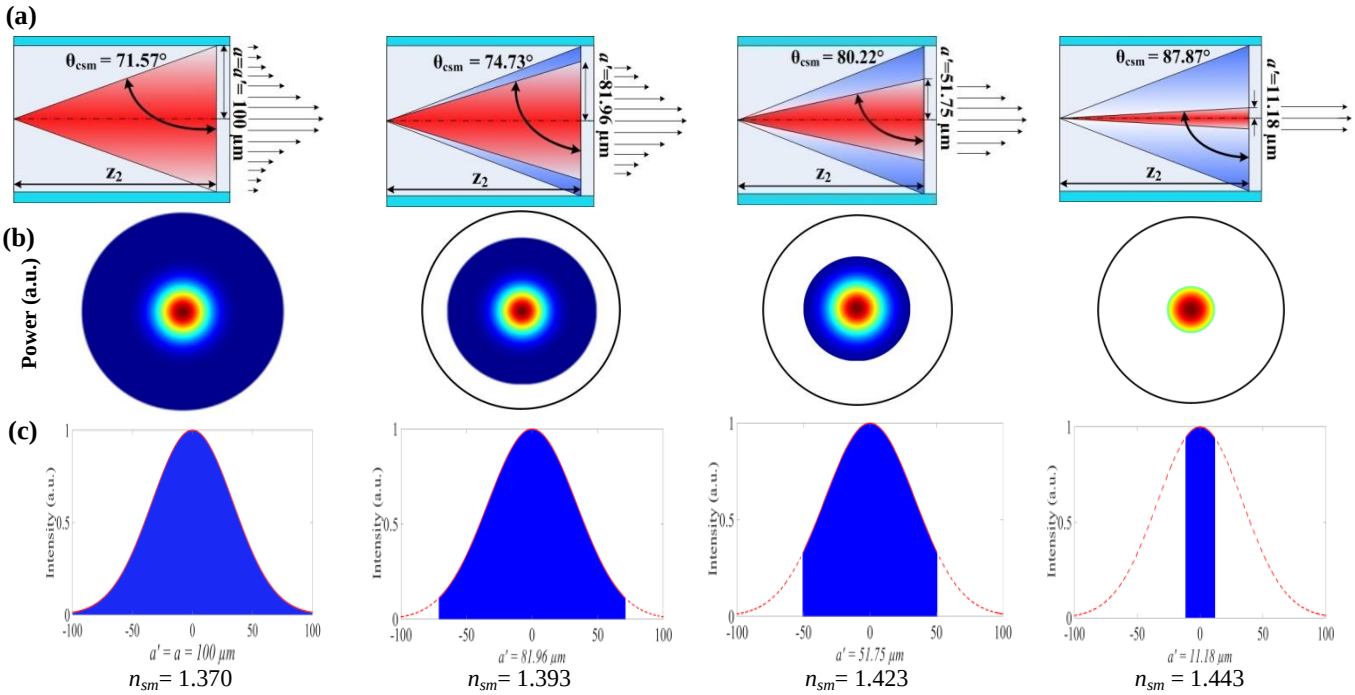

n_{sm}= 1.370 n_{sm}= 1.393 n_{sm}= 1.423 n_{sm} = 1.443

Figure 2.4. Evolution of optical power and intensity in the MMF RI sensor for various values of n_{sm} by modification of the critical angle, θ_{csm}, for $n_{cl} < n_{sm} < n_{co}$: a) increasing n_{sm} will increase θ_{csm} which reduces the acceptance angle of the propagating beam, b) power in transversal plane decreases for increasing n_{sm}, and c) illustrates decreasing optical intensity over different a' values obtained by Equation (2.17).

As described in Equations (2.27) and (2.28), increasing n_{sm} leads to increasing θ_{csm}, which represents the mode loss occurring in the MMF as illustrated by a decrease of the red beam in Figure 2.4(a). This also reduces the beam area as illustrated in Figures 2.4(b) and 2.4(c) which represent a decreasing guided power in the MMF. This decreased guided power due to mode loss contribution will concurrently be subject to EWA as described in Equation (2.26).

2.2.3. Sensing mechanism and modeling in Zone III

The last condition is Zone III where $n_{sm} > n_{co}$. Here, propagation by TIR is no longer supported although a very small portion of optical power can still be guided due to the phenomenon of external reflection. This can be explained by Fresnel equations for a beam incident at an interface between two media of different RI values as illustrated in Figure 2.5.

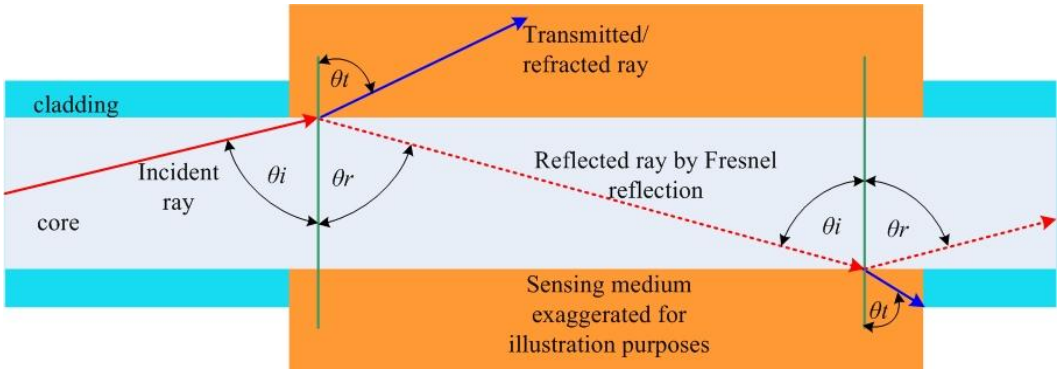

Figure 2.5. Optical power guided by external reflection in Zone III when $n_{sm} > n_{co}$. The majority of the power is transmitted to the exterior while a small portion is reflected back into the core. This mechanism again arises when the ray intersects the interface between the sensing region and the external medium. This phenomenon is more prominent for rays which have incident angles close to 90°.

Since $n_{sm} > n_{co}$, most of the optical power of the ray will be transmitted to the exterior. Furthermore, as illustrated in Figure 2.5, the sensing medium is much thicker than the core diameter, and, hence, the transmitted ray will not be back-reflected into the core. However, a small proportion of power is still reflected back into the core by the external reflection mechanism at the core-sensing medium interface. This proportion of back-reflected power can be obtained by calculating the reflectivity (R) for the light containing both the *p*-polarization (r_p) and *s*-polarization (r_s) components using the Fresnel equations in Equations (2.22), (2.23), and (2.24). Subsequently, the model to estimate the power response to variations in RI values in Zone III can mathematically be expressed by

$$P_L = \int_{\theta_b}^{90^\circ} P_0(\theta_i) R(\theta_i)^{N(\theta_i)L} d\theta_i \tag{2.29}$$

2.3. Experimental set-up

During the measurements, a differential probe configuration is employed, as shown in Figure 2.6. One MMF serves as the reference fiber while the other MMF is exploited as the sensing fiber. The differential set-up allows to compensate common-mode noise produced by both MMFs. The sensor, based on the ratiometric intensities from the two MMFs, thus measures the transmitted power for both the reference and sensing MMFs using two identical Thorlabs *Ge*-type PDA50B photodetectors (PDs)

with a peak spectral response within 800-1800 nm. A single-mode fiber-pigtailed DFB laser diode from Modulight, Inc., emitting at 1550 nm and driven by precision current and temperature controllers, is employed to interrogate the fibers. The laser output beam is divided by a single-mode fiber coupler to obtain two equal or symmetrical beams. These are next collimated and then injected into the reference and sensing MMF arms of the sensor via two identical MOs with *NA* = 0.65 in order to transmit the launched beam over all acceptance angles in the fibers. The MMFs are plastic-clad silica (PCS) fibers exhibiting an *NA* of 0.48 ± 0.02, with 200 µm core diameter and 230 µm cladding diameter. The output powers detected from both MMF arms are then transmitted to a dedicated computer via a 14-bit 2-MHz Agilent data acquisition system (DAQ) for further processing.

a)

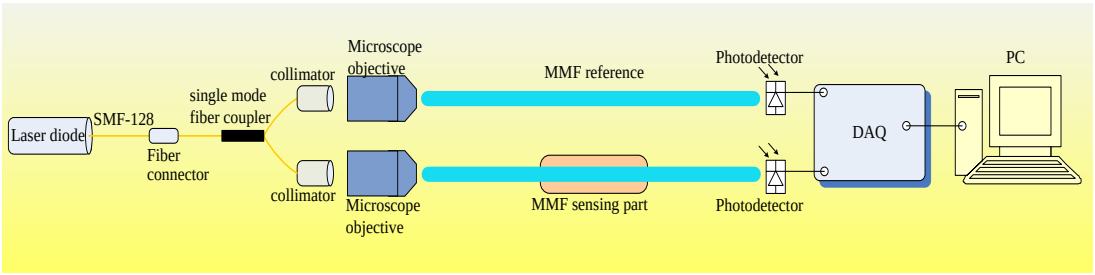

b)

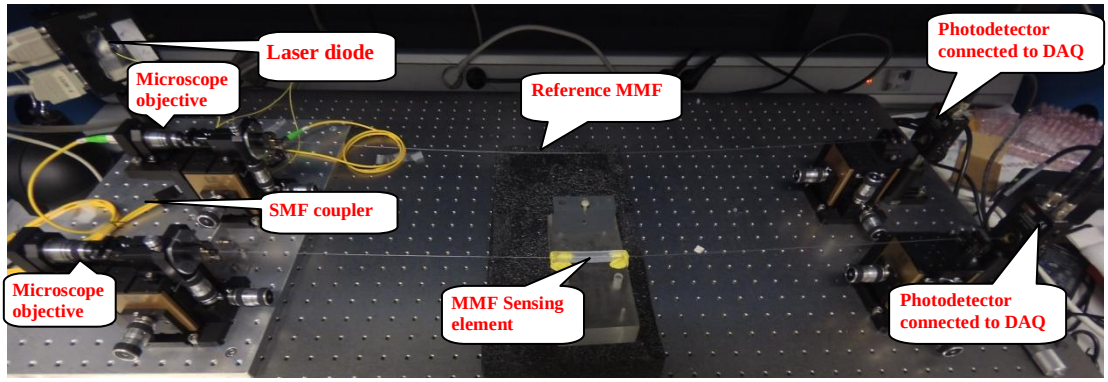

Figure 2.6. Experimental set-up of MMF-based refractometer under differential configuration to compensate common-mode noise: a) schematic set-up, b) photograph of experimental set-up. DAQ and PC not shown.

The MMF sensing region is realized by thermally removing 1 cm, 2.5 cm and 4 cm of cladding from three fibers using a thermal stripper (see Figure 2.7).

Figure 2.7. Thermal stripper for removing MMF cladding as well as fiber coating.

This is then followed by a simple procedure of cleaning the fiber core using acetone and isopropanol solutions, resulting in a typical MMF sensor structure as shown in Figure 2.8.

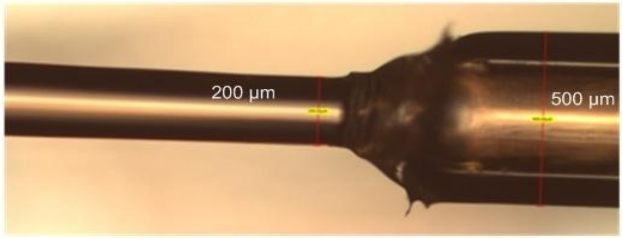

Figure 2.8. Stripped-cladding region of MMF sensing arm. The MMF core diameter is 200 µm and the outer (coating) diameter is 500 µm. A target liquid or fluid serves as the sensing medium to substitute the stripped cladding.

The sensing area where the cladding is stripped off the MMF is thus sensitive to variations in the RI value through variations of the optical power transmitted as a function of the target medium's RI. As previously mentioned, 3 different conditions or sensing phenomena can intervene in the MMF refractometer. These detection mechanisms are further elaborated below

2.4. Simulation and experimental results

A suite of simulations is next performed based on the above models and validated against experimental data for the three sensing Zones with three different sensor lengths. The sensing medium is composed of a combination of glycerol-water mixture which is adjusted [6] to obtain different RI values ranging from 1.3164 to

1.4571 RIU (refractive index unit) at a wavelength of 1550 nm as shown in Figure 2.9.

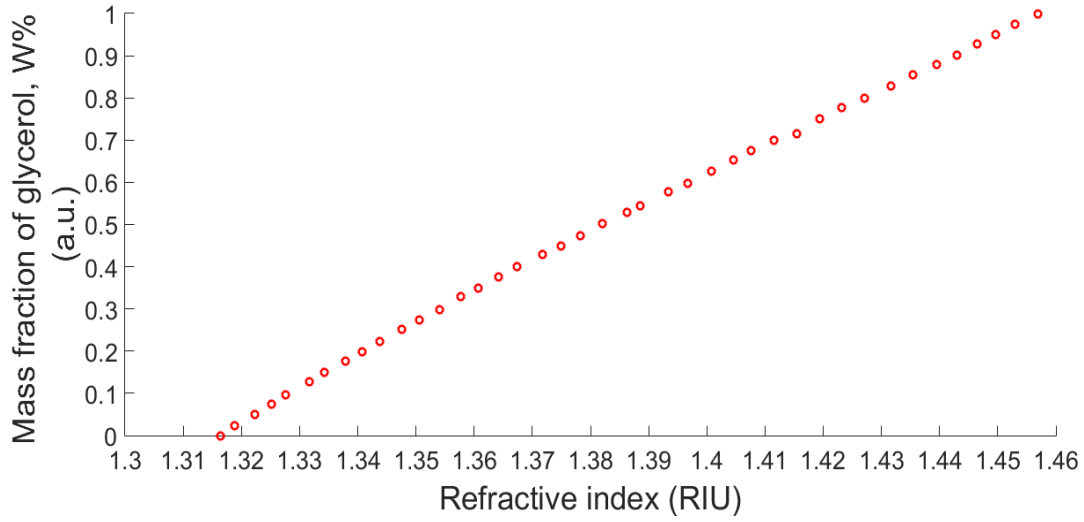

Figure 2.9. Refractive index of glycerol-water solutions at 1550 nm [6].

For RI values beyond 1.4571, calibrated RI liquids from Cargille Laboratories, Inc. were employed. Furthermore, different glycerol-water concentration levels exhibit varying absorption coefficients (α), with that of water being experimentally determined in a controlled environment to be 11.49 cm^{-1} and that of glycerol being 11.10 cm^{-1}. Assuming a linear relationship between the imaginary part or extinction coefficient of the mixture's RI (k_{mix}) and its volume fraction, which is a function of the glycerol (f_g) and water (f_w) fractions (with $f_g + f_w = 1$), and the extinction coefficients of glycerol (k_g) and water (k_w), we can estimate $k_{mix} = f_g\, k_g + f_w\, k_w$. The composite absorption coefficient of the solution α_{mix} can then be obtained via [98]

$$\alpha_{mix} = \frac{4k_{mix}\pi}{\lambda} \tag{2.30}$$

The simulation procedure is carried out according to the following flow chart in Figure 2.10. The subsequent simulation results illustrate the sensor response in terms of the normalized optical power as a function of RI.

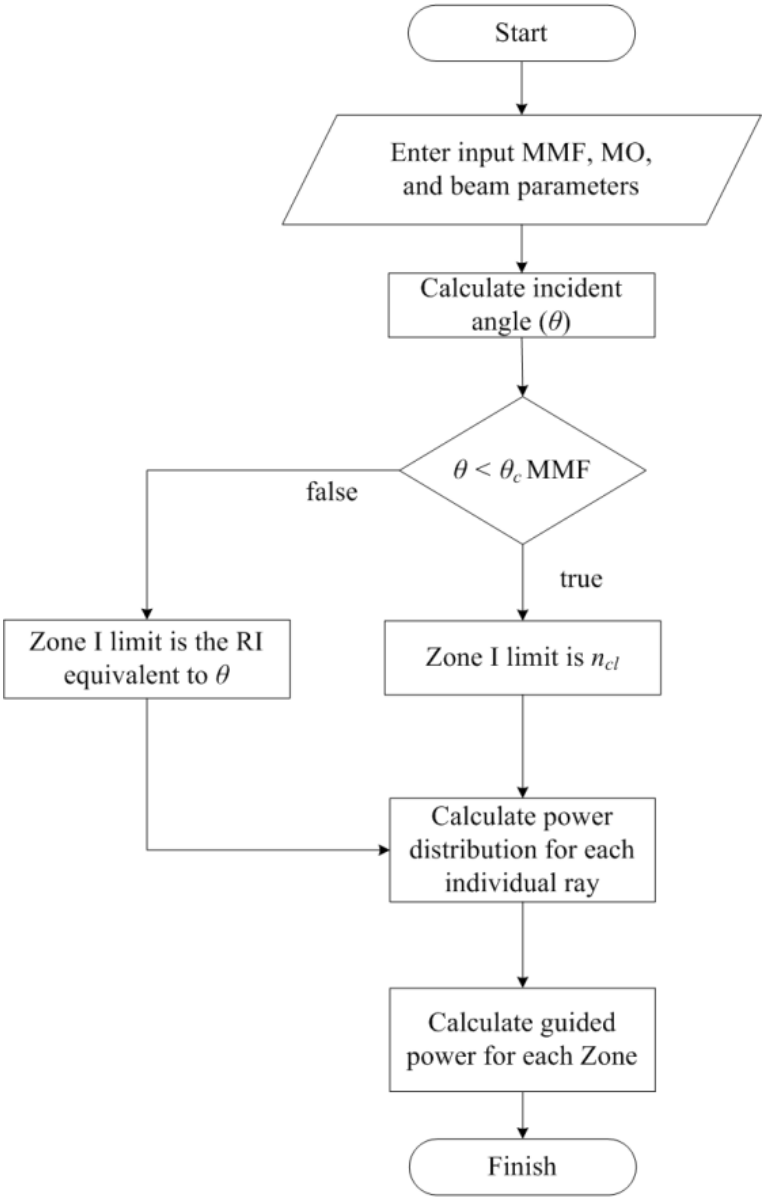

Figure 2.10. Flow chart to calculate RI-dependent guided power.

From the models in Equations (2.11), (2.26), and (2.29), the initial power (P_0) must be discretized into individual rays from θ_b to 90°. As explained above, discretization of the injected beam can be performed at the point z_2 by varying a' in discrete steps (from 100 μm to 0) corresponding to the θ_i value for each ray. The resulting power distribution injected into the MMF is plotted in Figure 2.11.

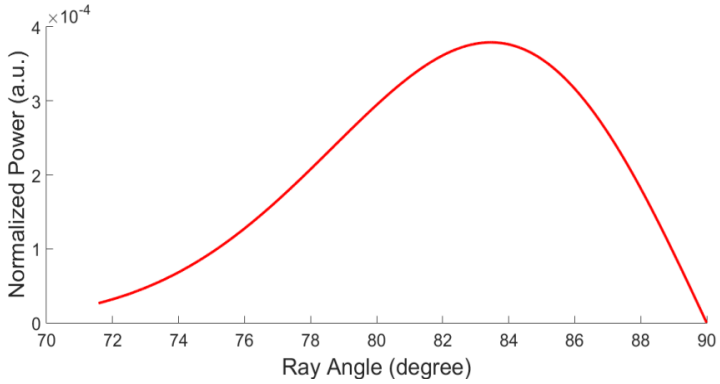

Figure 2.11. Simulated input angular power distribution density $P_0(\theta_i)$ injected into the MMF for incident angles from θ_b to 90°.

As illustrated in Figure 2.11, a peak occurs at ~83° and results from the fact that the resulting angular power density takes into account both the angular Gaussian beam distribution (Figure 2.12(a)) as well as its corresponding illuminating angular area (Figure 2.12(b)).

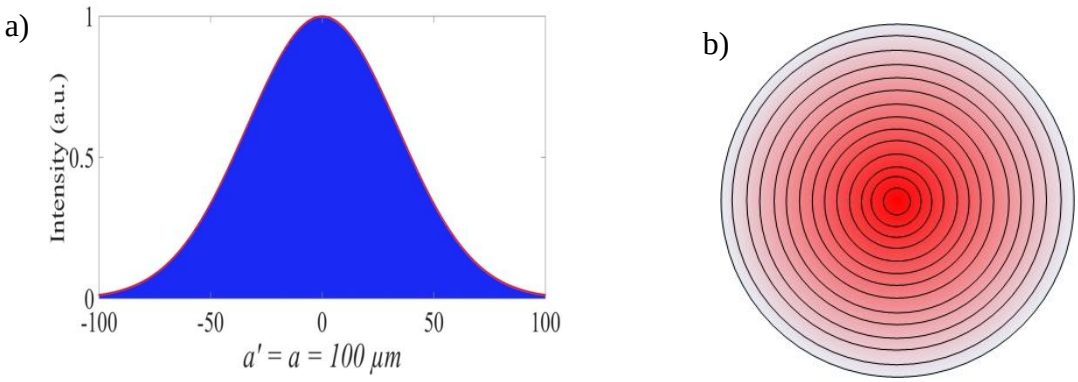

Figure 2.12. a) Gaussian beam intensity, and b) cross-section of Gaussian beam for different radius a'.

The discretized ray powers across the incident angles are subsequently employed in the models defined by Equations (2.11), (2.26) and (2.29) which represent the power response in Zone I, Zone II and Zone III, respectively. The results are then experimentally validated and plotted in Figure 2.13 below.

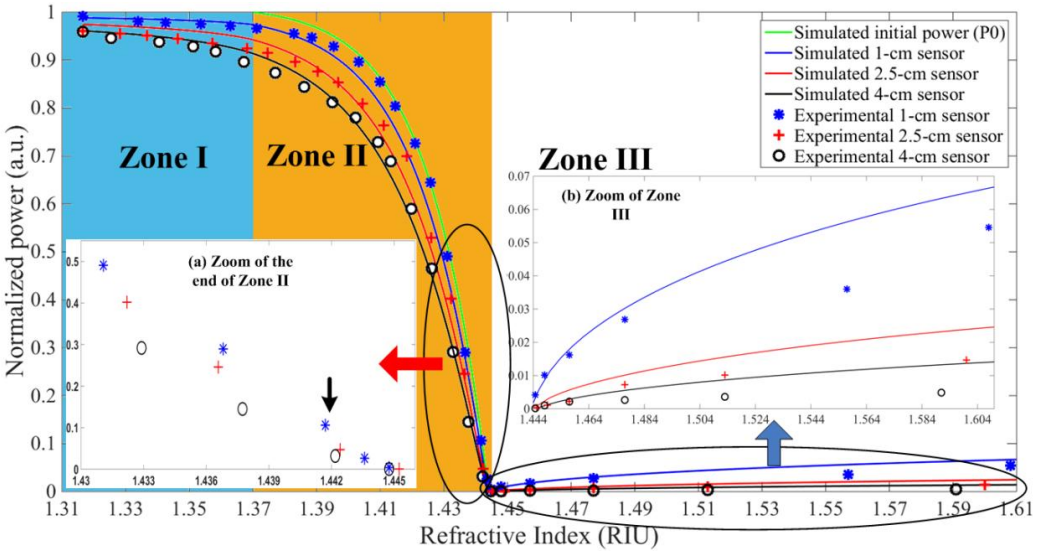

Figure 2.13. Response of three sensors across three different RI Zones. Continuous lines are simulation results. Green line represents variation of total initial power ($P_0(\theta_b, \pi/2)$) in Zone II due to modification of critical angle without EWA. Blue, red, and black lines are simulation results for 1-cm, 2.5-cm, and 4-cm sensors, respectively. Symbols '*', '+', and 'o' represent experimental results for 1-cm, 2.5-cm and 4-cm sensors, respectively. The black arrow in inset (a) indicates power response slowing down beyond this measured RI point, while inset (b) indicates sharp increases at the beginning which then slows down with increasing RI.

The sensitivity curves of the RI sensors are next obtained for each sensing region or zone and plotted in Figure 2.14. These curves are obtained by differentiating the fitted curves through the experimental data in Figure 2.13 based on the models for each zone.

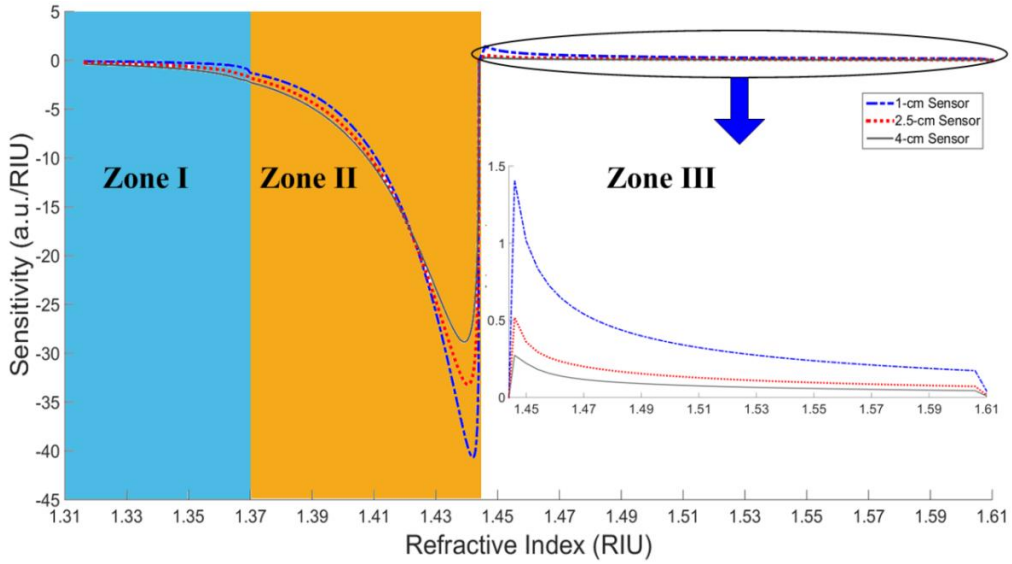

Figure 2.14. Sensitivity curves of RI sensors in three different Zones by derivation of the experimental curves (dP/dRI). '–·–·', '····', and '—', represent the sensitivity response for the 1-cm, 2.5-cm, and 4-cm sensors, respectively.

Here, the sensitivity for each sensor has been obtained by first fitting specific response curves to the 3 respective sensing Zones in Figure 2.13 followed by their derivation with respect to RI.

2.5. Discussion

Three complete models for the three different sensing zones of an MMF refractometer for RI measurement have, for the first time, been developed as a function of the injected lightwave characteristics into the fiber. The mathematical models for Zone I and Zone II are similar as a consequence of direct influences from EWA. Although the principal model for EWA has been defined by Equation (2.11) for Zone I and by Equation (2.26) for Zone II, these Zones are subject to different initial powers P_0. Hence, in Zone I, the initial power is $P_0 = P_0(\theta_b, \pi/2)$ for $\theta_b > \theta_c$ or $P_0 = P_0(\theta_c, \pi/2)$ if $\theta_b < \theta_c$, while in Zone II, it takes the form $P_0 = P_0(\theta_{csm}, \pi/2)$.

For the Zone I response, P_0 is conserved for each of the rays over the entire RI response of the sensing medium as all the rays within the sensing region are guided by TIR. Hence, if θ_b is less than θ_c of the MMF, the injected rays will propagate in the sensing region, from a fiber critical angle θ_c of ~70.60° (equivalent to a cladding RI of 1.362) to 90°, as predicted by Equation (2.1). However, in this work, θ_b = 71.57°, corresponding to an equivalent RI value n_b of ~1.370, which is higher than n_{cl} of 1.362. Subsequently, all incident rays from MO will be guided in the MMF core by TIR. The simulated results plotted in Figure 2.13 demonstrate good agreement with the experimental data, with the blue, red, and black continuous lines corresponding to simulation for the 1-cm, 2.5-cm, and 4-cm stripped-cladding sensors, respectively. The symbols '*', '+', and 'o' represent the respective experimental measurements. Longer sensing lengths will incur higher losses, hence the power measured decreases when the RI increases due to the increasing transmission (T) penetrating into the cladding, i.e. more power is absorbed at higher RI, as described by Equations (2.10) and (2.11), respectively.

For Zone II, where $n_{cl} < n_{sm} < n_{co}$ (n_{co} = 1.444), the variation of the optical power guided for different values of n_{sm} is due to two optical phenomena as illustrated in Figure 2.3. Here, the rays arrive in the sensing region guided by TIR since the

incident beam angle is 71.54° and thus, the beginning of Zone II is equivalent to an RI value of ~1.370. The green line in Figure 2.13 represents the simulated initial power variation $P_0(\theta_{csm},\pi/2)$ as a function of RI due uniquely to the modification of the critical angle θ_{csm} and does not reflect the influence of EWA. However, the contribution from EWA in the sensing region will lead to a smaller additional decrease in the total guided power along the fiber. This is clearly demonstrated through simulations in the form of continuous blue, red, and black lines for L = 1 cm, 2.5 cm, and 4 cm, respectively, as predicted by Equation (2.26). Now, identical to the EWA phenomenon in Zone I, the longer sensing region in Zone II is subject to higher absorption (Figure 2.13). The high agreement between the simulated results and the experimental measurements clearly demonstrates that the higher power losses occurring in Zone II are due to the contribution of both modification of the critical angle and EWA. The contribution of losses due to modification of the critical angle is also found to be more dominant than EWA in this Zone. Further, the power variation is observed to increase slowly at the beginning of Zone II toward the end of the Zone where it then decreases sharply. This sharp decrease is due to the power distribution of the Gaussian beam which increases sharply from the sides or wings of the distribution (i.e. top-hat radius) towards the peak (i.e. circular aperture) of the Gaussian curve, but which decreases at the peak area (i.e. circular aperture area with top-hat profile) [96]. Hence, the optical power response in Figure 2.13 will exhibit a flat response or inflexion point at exactly the boundary between Zone II and Zone III.

The last operating regime of the MMF refractometer is Zone III which can be employed for probing a medium with $n_{sm} > n_{co}$. Under this condition, there is no propagation by TIR. Nevertheless, the incorporation of the Fresnel relations in Equations (2.22), (2.23) and (2.24) into Equation (2.29) postulates the existence of guided power in the core by the phenomenon of external reflection, in particular, from the rays which have incident angles θ_i in the sensing medium close to 90°. Although the guided power is relatively weak, this will increase for further increases in the value of RI beyond that of n_{co}. This is validated experimentally in Figure 2.13 through the measurement of increasing power at the fiber output end as n_{sm} increases beyond that of the core. Complementary to this, Equation (2.29) further correctly predicts a higher power guided over shorter lengths of sensing region in the MMF

since there are fewer reflections (*NL*) which, in turn, reduce the transmitted power or number of rays to the exterior through the sensing medium. Nonetheless, the respective discrepancies between the simulations and the experimental results for the different sensing lengths in Zone III could be due to non-ideal conditions during the experimental study, such as the existence of very small bends in the MMF which can alter the optical power distribution and/or modify the beam quality factor (M^2) by inducing changes to the MMF index profile in the bending area [99]. There could, in addition, be minute influences from the mechanical stability of the experimental set-up (minor variation of the focal points of the MOs, slight mechanical drifts in the translation stages, etc, induced by temperature variations).

The sensitivity curves plotted in Figure 2.14 illustrate the best sensitivity being achieved in Zone II for the shortest sensing length (i.e. 1-cm stripped-cladding fiber) as the shortest sensor is subject to the least EWA. Consequently it suffers higher losses through modification of the critical angle (mode loss mechanism) as predicted by the continuous green line in Figure 2.13. Toward the end of the Zone II response, there is more power variation for a small RI variation. The three sensitivity curves first increase sharply from the middle of Zone II, and then decline less sharply toward almost the end of this Zone before decreasing back toward zero at the core index (1.444) which is the minimum point of the optical power response (see Figure 2.13). The respective inflexion points of the sensitivity curves in Figure 2.14 occur before the end of Zone II and correspond to the beginning of the decreasing gradient of the optical power response as described above with respect to the circular aperture area (with top-hat type peak profile) of the Gaussian beam. A zero sensitivity value could potentially be obtained when the power response in Figure 2.13 occurred over very small RI variations (i.e. tending toward 0 or $\Delta RI \rightarrow 0$) of the sensing medium. However, since the practical RI variations induced in this work cannot be infinitesimal, the sensitivity of the three sensing lengths obtained at the end of Zone II cannot reach zero value. Nevertheless, the sensitivity curves plotted in Figure 2.14 decrease toward zero when the measured RIs approach the end of Zone II (i.e. close to the core index).

Conversely, for Zone I, the longest sensor has better sensitivity since the principally EWA contributions to the sensing mechanism are cumulative over the entire sensing length. There is thus more absorption by the longest sensor resulting in the largest power variation as a function of RI. In Zone III, on the contrary, the shortest sensor is again more sensitive since less power is lost to the exterior, and consequently more power is guided in the fiber core. Hence, according to Equations (2.22), (2.23), (2.24) and (2.29), the guided power increases with increasing RI, with the increasing power being sharper at the beginning of Zone III, and subsequently declines less sharply with increasing RI. Thus, the sensitivity decreases with increasing RI in the sensing medium since the rate of power variation with RI decreases. Nevertheless, although this sensor theoretically has virtually unlimited dynamic range for operation over Zone III, its performance could be limited to only a certain RI range when the sensitivity approaches the noise level.

Based on the sensitivity (S) curves in Figure 2.14, the sensor resolution is determined with respect to the measurement noise level using the 6σ-definition (6 times RMS noise (σ_{rms}) corresponding to ~99.7% confidence level) [100] as given by Equation (2.31) with only ~0.3% of the samples lying outside this distribution.

$$resolution = \frac{6\sigma_{rms}}{S} \tag{2.31}$$

The best resolution achieved is 2.2447×10^{-5} RIU by the 1-cm sensor in Zone II. It is also in this Zone that the 2.5-cm and 4-cm sensors have the best relative resolutions of 2.9919×10^{-5} RIU and 3.2634×10^{-5} RIU, respectively, compared to the other two Zones. For Zone I, the best resolution is achieved by the 4-cm long sensor with a minimum detection level of 1.5438×10^{-3} RIU while the 1-cm and 2.5-cm sensors are capable of resolutions of 5.1952×10^{-3} RIU and 1.7462×10^{-3} RIU, respectively. The achievable sensor resolution in Zone I is not very high due to the induced multiplicative noise from multiple reflections in the sensing region as well as the relatively low sensitivity in this zone. For the Zone III response, the noise level is relatively low since most of the injected power, including the noise from multiple reflections, are transmitted to the exterior. In this zone, the normalized noise level ranges from approximately 1.2×10^{-4} (a.u.) – 1.6×10^{-4} (a.u.) and is typically

dominated by the measured photodetector noise, normalized to 8.66×10^{-5} (a.u.). The minimum RI resolution that can be detected in Zone III are 1.0031×10^{-3} RIU, 1.8070×10^{-3} RIU, and 3.1920×10^{-3} RIU for the 1-cm, 2.5-cm, and 4-cm sensing lengths, respectively. The low resolution obtained in Zone III can simply be understood by the low sensitivity in this zone as a consequence of higher losses arising from external reflection, as explained previously. Table 2.1 below summarizes the performance of the three MMF refractometers.

Table 2.1. Performance comparison between three MMF refractometers characterized by three distinct stripped-cladding lengths.

	MMF refractometer (1 cm)			**MMF refractometer (2.5 cm)**			**MMF refractometer (4 cm)**		
	Zone I	**Zone II**	**Zone III**	**Zone I**	**Zone II**	**Zone III**	**Zone I**	**Zone II**	**Zone III**
Dynamic range (RIU)	1.316 - 1.37	1.37-1.444	1.444–1.61	1.316 - 1.370	1.4351-1.444	1.444–1.61	1.316 - 1.37	1.37-1.444	1.444–1.61
Highest resolution (mRIU)	5.295	0.02245	1.003	1.746	0.02992	1.807	1.54	0.0326	3.192

2.6. Conclusions

Three models have been proposed based on a combination of analytical wave optics to obtain the EWA equation, Gaussian beam optics to describe the injected power distribution, and ray optics to explain the principle of optical mode losses in an MMF configured for refractive index measurements. These models have been adapted to consider the three different sensing mechanisms as a function of the relative cladding and core RIs. Nonetheless, the models for Zone I and Zone II are fundamentally similar, whereby both zones are subject to EWA as the fundamental loss mechanism. However, Zone II involves the additional phenomenon of critical angle modification, which modifies the model employed through the use of different values of $P_0(\theta_{csm},\pi/2)$ as a function of RI variation. Further, since the incident beam angle in the fiber is higher than θ_c, the boundary between Zone I and Zone II is no longer the cladding RI value (1.362 RIU), but the RI which corresponds to the incident beam angle (RI ~1.370 RIU). Finally, the model for Zone III exploits Fresnel relations, where the rays propagating in the sensing region exhibit different power variations as

a function of the ray angle with respect to their initial $P_0(\theta_b, \pi/2)$ for an acceptance angle carried over from Zone II. These models are, however, limited to a certain length of MMF cladding to be removed without any residual cladding remaining in the sensing area.

The experimental measurements performed are found to validate the simulation results derived from the models to describe the three different optical sensing mechanisms in the MMF refractometer. The results confirm that in Zone I, the sensing mechanism is uniquely via EWA which induces the largest losses in the sensor with the longest sensing region. For Zone II, the best sensor resolution of 2.2447×10^{-5} RIU is achieved for the 1-cm sensor. The sharp power decrease occurring in Zone II is a consequence of the losses induced by modification of the critical angle for a Gaussian beam, where most power is concentrated at the center axis (top-hat area), corresponding to an incident angle close to 90° (i.e. close to the core RI). However, at the beginning of Zone II, the losses are relatively small due to the weaker power distribution at the edges of the Gaussian beam which corresponds to an RI approaching that of the cladding, such that the losses are dominated by EWA. Last, but not least, in Zone III, when the external reflection mechanism intervenes, only a relatively small initial guided power exists, which subsequently increases as the external medium's RI increases due to the increasing reflectivity of the rays back into the fiber core. As predicted by the models, the longest sensor will guide less optical power since more reflections are induced by a longer sensing region, resulting in more rays being transmitted toward the exterior.

CHAPTER III

Hybrid Single Mode – Multimode Fiber-based Refractometer

3.1. Introduction

In the previous chapter, a functional and accurate model has been developed to explain the three sensing conditions or RI zones in the stripped-cladding multimode fiber (MMF)-based refractometer, as a function of different sensing phenomena or mechanisms and their subsequent responses to RI variations. Also, as explained and demonstrated in Chapter II, the first Zone has been classified as the RI regime in which the sensing mechanism is due uniquely to evanescent wave absorption (EWA). The second Zone or regime describes sensing mechanisms combining both EWA and mode losses. The third or last Zone has been defined as the RI regime in which the sensing mechanism is stimulated only by Fresnel reflections which occur when the sensing medium index is higher than the core index.

Three models were next proposed and developed in Chapter II integrating Snell's law, Fresnel reflections, and the analytic equation for EWA which are supported by Gaussian beam analysis. Gaussian beam analysis was employed to fully characterize the launching conditions through a microscope objective (MO) at the input end of the MMF, while wave optic analysis permitted to predict the absorption characteristics of the evanescent waves. Subsequently, both Gaussian beam and wave optic principles were employed to reinforce ray optic analysis of the propagating modes in the MMF, leading to highly accurate and robust models for Zone I and Zone II. In addition, to develop the model for Zone III, Gaussian beam analysis was combined with Fresnel's reflection equations in a ray optic analysis to accurately estimate the power response for a sensing medium index which was higher than that of the core.

The previous models applied to the stripped-cladding MMF-based refractometer have successfully predicted the power response curves over three sensing zones which were experimentally validated. According to simulation and experimental

results, the classic sensitivity curves can be obtained, where the best sensitivity and resolution were achieved for Zone II. However, less sensitivity and a lower resolution were achieved in Zone III. In addition, since the previous experimental set-up employed mechanical translation stages for adjusting the beam injection condition into the MMF, any minute vibrations or mechanical perturbations could influence the sensor performance.

To overcome those problems, a hybrid compact all-fiber set-up is proposed in this chapter through the use of a single-mode fiber (SMF) and MMF combination without the inconvenience of opto-mechanical elements such as translation stages and MOs. The laser beam is launched into a lead-in SMF which is fusion-spliced to an MMF. This ensures that the beam is injected directly from the SMF into the MMF with an incident angle closer to 90° (or more precisely ~83.6°) at the MMF core-cladding (or external medium) interface in the present set-up compared to ~71.57° when MOs were used. Subsequently, the total number of reflections (*NL*) decreases along the sensing region, leading to lower losses by refraction across the interface when the sensing medium index, n_{sm}, is higher than the MMF core index, n_{co2}. This will consequently increase the guided optical power and, hence, the sensitivity in Zone III due to contribution from higher Fresnel reflections when compared to Chapter II. A key objective of this chapter is thus to develop and validate a realistic and practical model of an all-fiber RI sensor with direct injection of light from an SMF coupled to an MMF. This model should accurately estimate the optical power response as a function of the measured RI for different sensing lengths, which are the lengths of the fiber sections where the cladding and the coating or buffer have been removed. Two different lengths of 2-cm and 5-cm de-cladded regions are theoretically analyzed and corroborated experimentally to very good agreement.

3.2. Modeling of hybrid SMF-MMF refractometer

3.2.1. Determination of the input power into the MMF

A hybrid SMF-MMF refractometer is realized using an SMF which is fusion-spliced to a plastic-clad silica (PCS) MMF with a core diameter (a_2) of 200 µm and a numerical aperture (NA_2) of 0.50. This has been carried out using a fusion splicer as

shown in Figure 3.1(a), resulting in a hybrid SMF-MMF architecture in Figure 3.1(b). The subsequent injected lightwave will then be diffracted according to the principles illustrated by Figure 3.1(c).

a)

b)

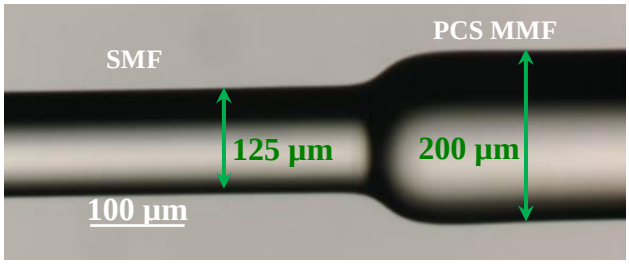

c)

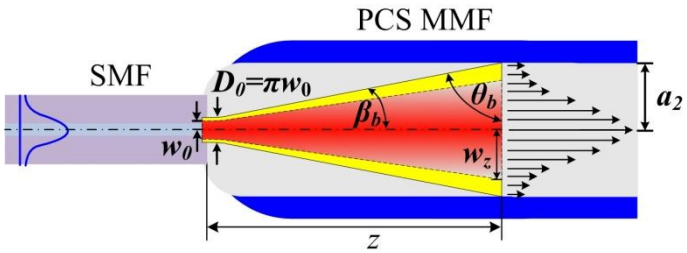

Figure. 3.1. Coupling between SMF and MMF: a) fusion splicer,b) photo image of fusion-splicing region between SMF and MMF, and c) illustration ofprinciples of lightwave injection and diffraction at interface of both fibers from incoming single-mode laser through lead-in SMF, with radiated beam angle β_b into MMF and incident beam angle θ_b.

Here, it is supposed that the guided beam output from the lead-in SMF has similar characteristics to a collimated beam with a Gaussian distribution, where the fiber's mode field diameter (MFD_{SMF}) is defined as at $1/e^2$ of the beam intensity with a spot radius of $w_0 = 0.5MFD_{SMF}$. Thus, 99% of the beam intensity in the SMF is contained within a diameter $D_0 = \pi w_0$ [96]. Furthermore, as illustrated by Figure 3.1(c), the laser beam is diffracted from the lead-in SMF into the MMF with an incident beam angle $\theta_b = 90°-\beta_b$, where the radiated beam angle β_b is calculated in terms of both the SMF's numerical aperture (NA_1) and the core index of the MMF (n_{co2}) as

$$\beta_b = \sin^{-1}\left(\frac{NA_1}{n_{co2}}\right) \tag{3.1}$$

For an SMF, the numerical aperture cannot be trivially calculated as for an MMF, i.e. as a function of the core index (n_{co}) and the cladding index (n_{cl}) using the relation $NA = \sqrt{{n_{co}}^2 - {n_{cl}}^2}$. In practice, for an SMF, *NA* is defined by measuring 99% of the optical power level at distance *z* after diffraction [97] as illustrated in Figure 3.2.

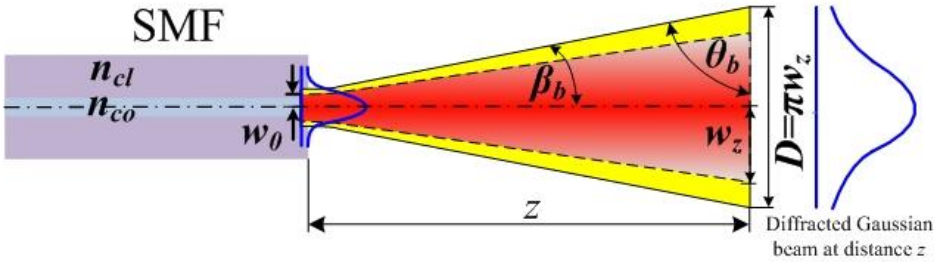

Figure 3.2. Beam radiated by an optical fiber where the red area represents 1/e² of the optical power while the yellow region represents more than 99% of the optical power.

Thus, β_b can be obtained using the following trigonometric relation

$$\beta_b = \tan^{-1}\left(\frac{0.5D}{z}\right) \tag{3.2}$$

This β_b can then be simplified with respect to the β_b value approaching 0 radian, resulting in

$$\tan^{-1}\left(\frac{0.5D}{z}\right) \cong \frac{0.5D}{z} \tag{3.3}$$

and, hence

$$\sin\beta_b \cong \frac{0.5D}{z} \tag{3.4}$$

Also, since $NA = n \sin\beta_b$, NA_1 can therefore be approximated by

$$NA_1 \cong n_{co2}\left(\frac{0.5D}{z}\right) \tag{3.5}$$

where $D = \pi w_z$ is the beam diameter at 99% of the optical power at distance *z*, resulting in a relation between NA_1 and the beam radius at distance *z* (w_z) which can be given as

$$NA_1 \cong n_{co2}\left(\frac{0.5\pi w_z}{z}\right) \tag{3.6}$$

Now, w_z is the beam radius at distance z which is diffracted from the SMF with a beam spot radius w_0 using the following relation

$$w_z = w_0\sqrt{1+\left(\frac{\lambda z}{n_{co2}\pi {w_0}^2}\right)^2} \tag{3.7}$$

where distance z can be obtained using a simple trigonometric function in terms of the MMF radius a_2 and β_b in the form

$$z = a_2 \cot\beta_b \tag{3.8}$$

Further, as w_0 is the SMF beam spot radius which is half its mode field diameter (MFD_{SMF} = $2w_0$), MFD_{SMF} must be estimated. Theoretically, MFD_{SMF} can be estimated by taking the diameter at 35% of the Gaussian intensity distribution of the fundamental mode [101]. Here, the fundamental mode of SMF is obtained using FEM simulation in COMSOL, as illustrated in Figure 3.3, from which MFD_{SMF} is ~9.7 µm. This is equivalent to w_0 = 4.75 µm.

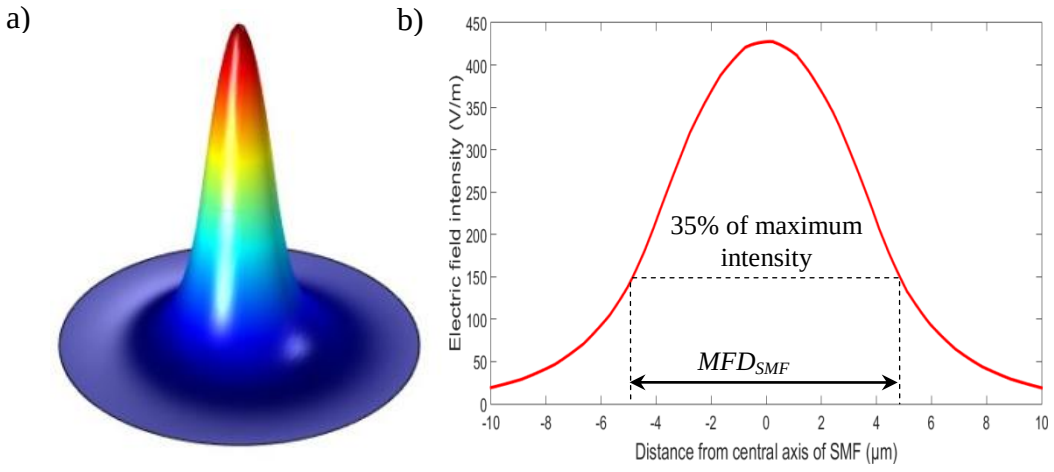

Figure 3.3. Gaussian distribution of fundamental mode in SMF, a) under 3D representation, with b) its equivalent electrical field intensity.

Since z in Equation (3.8) is much larger than the confocal distance or Rayleigh length z_0 (= $\pi {w_0}^2/\lambda$), w_z in Equation (3.7) can be approximated by

$$w_z \cong \frac{\lambda z}{n\pi w_0} \tag{3.9}$$

Hence, by substituting Equation (3.9) into Equation (3.6), NA_1 can be expressed by

$$NA_1 \cong \frac{\lambda}{2w_0} \cong \frac{\lambda}{MFD_{SMF}} \tag{3.10}$$

From Equation (3.10), the numerical aperture of SMF (NA_1) is 0.16 which corresponds to a β_b of 7.3°, obtained by Equation (3.1). The optical intensity at distance z (I_z) of this Gaussian beam can then be expressed by [90, 95]

$$I_z(a_2) = I_0 e^{\left(-\frac{2a_2^2}{w_z^2}\right)} \tag{3.11}$$

The input optical power into MMF, P_z, can be obtained by integrating the optical intensity in Equation (3.11) over the transverse plane of the beam with respect to the beam radius, followed by normalizing through $I_0 = \pi w_z^2/2$ to result in [90, 95]

$$P_z(a_2) = 1 - e^{\left(\frac{-2a_2^2}{w_z^2}\right)} \tag{3.12}$$

With NA_2 = 0.50, and only the middle region of MMF stripped of its cladding, θ_b in MMF is thus always higher than its critical angle (θ_c). Therefore, this beam will completely be propagated within MMF by TIR without any part of the beam (rays) being transmitted or refracted into the cladding.

3.2.2. Sensing mechanisms

As explained and demonstrated in the previous chapter, the sensing mechanisms in the stripped-cladding MMF-based refractometer are classed according to 3 conditions or RI zones. Zone I is defined for the condition when the light is fully guided by TIR in the sensing region and, therefore, only EWA occurs as the sensing mechanism as illustrated by Figure 3.4.

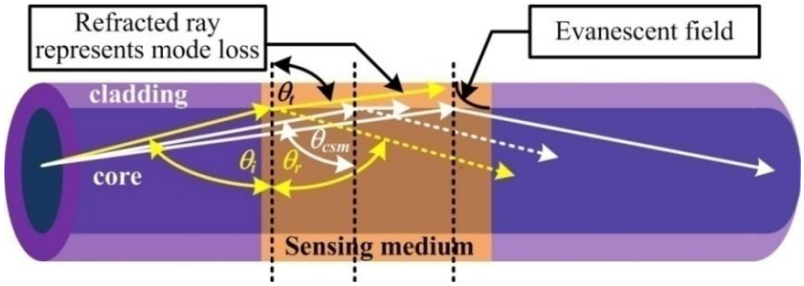

Figure 3.4. Sensing mechanism in Zone I based on EWA.

When $\theta_b > \theta_c$, Zone I range will be limited to measuring a sensing medium index n_{sm} lower than the equivalent index (n_b) associated with θ_b. This can be expressed as

$$n_b = n_{co2} \sin \theta_b \tag{3.13}$$

In Zone I, the guided optical power along MMF for a sensing region length, L, can then be estimated by integrating the optical power for each ray (θ_i) from θ_b to 90° through

$$P_L = \int_{\theta_b}^{90^\circ} P_0(\theta_i) e^{(-N(\theta_i)T(\theta_i)L)} \, d\theta_i \tag{3.14}$$

where P_0 represents the input power into MMF while N and T are the number of reflections per unit length and the transmission coefficient of the penetrating evanescent waves into the external sensing medium, respectively. These two parameters can be given by [93]

$$N(\theta_i) = \frac{\cot \theta_i}{2a_2} \tag{3.15}$$

$$T(\theta_i) = \frac{\alpha \lambda n_{co2} \cos \theta_i}{\pi n_{sm}^{\,2} \cos^2 \theta_{csm} \sqrt{\cos^2 \theta_{csm} - \cos^2 \theta_i}} \tag{3.16}$$

Here, α is defined as the absorption coefficient of the sensing medium, and θ_{csm} the equivalent critical angle at the interface core-sensing medium ($\theta_{csm} = sin^{-1}(n_{sm}/n_{co2})$). Now, the integral function in Equation (3.14), which will require both Equations (3.15) and (3.16), is relatively complicated to be solved analytically. Hence, to solve Equation (3.14) numerically, the input optical power in Equation (3.12) must consequently be discretized as individual rays to obtain P_0 for each θ_i value, from θ_b

to 90°. Discretizing the input beam into its individual rays can be carried out by injecting varying a_2 values into Equation (3.12) as explained in Chapter II.

A clearer and more intuitive illustration of the sensing mechanism in Zone I from which the results in Figure 3.5 physically demonstrate the evolution of the evanescent waves as a function of RI values is next performed. In this work, 2D wave optics simulation in the COMSOL Multiphysics environment is used since simulation in 3D would require excessively high computational load due to the extremely high number of meshes to be generated. In addition, 3D simulation is not necessary due to the cylindrical symmetry of the MMF structure. In this simulation, a core diameter of 60 µm is used instead of 200 µm, to avoid high load computation. A functional cladding defined by the simulator is used as the equivalent external sensing medium.

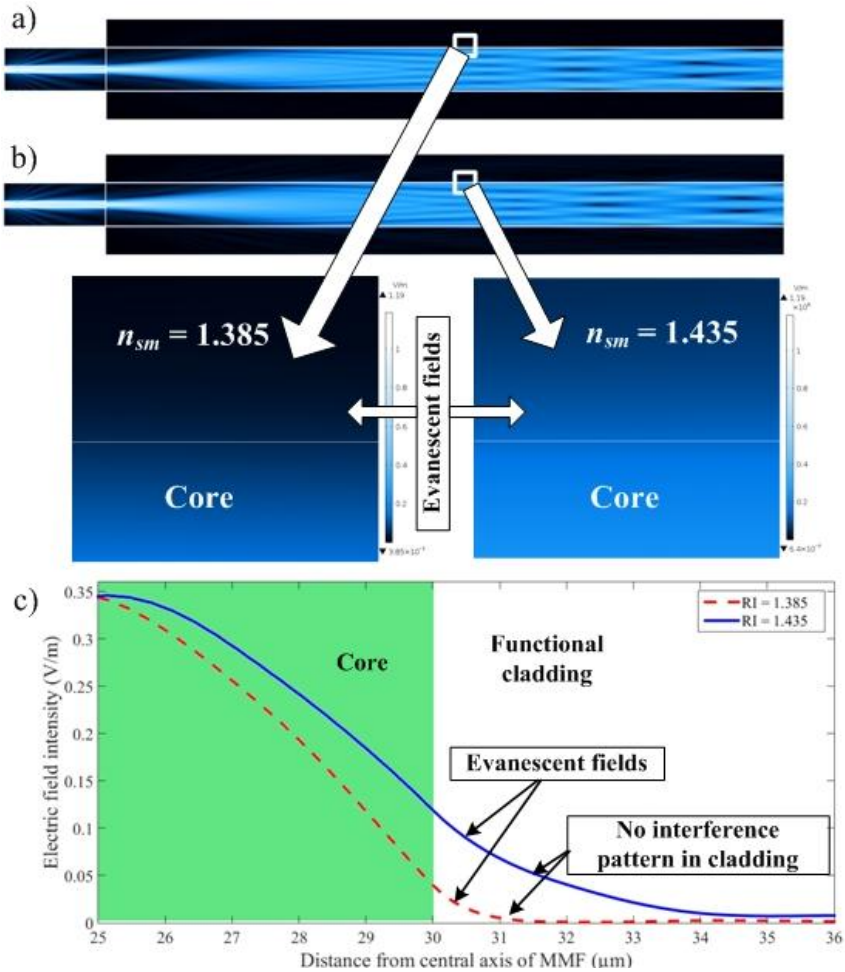

Figure. 3.5. COMSOL 2D wave optics simulation of wave propagation for Zone I for a) n_{sm} = 1.385, b) n_{sm} = 1.435, and c) evanescent waves penetrating with exponential decay of the electric fields into functional cladding.

As illustrated in Figures 3.5(a) and 3.5(b), where θ_b is higher than θ_{csm}, the beam from lead-in SMF is propagated totally in MMF by TIR. Moreover, the penetration of the evanescent waves into the external medium, represented by a functional cladding during simulation, increases with increasing cladding index as illustrated in Figure 3.5(c). As can be clearly explained by Equation (3.16), the square root in the denominator decreases towards zero when θ_{csm} increases towards θ_i, which leads to an increase in T. This is illustrated in the insets of Figures 3.5(a) and 3.5(b), where, for a functional cladding or sensing medium index (n_{sm}) of 1.435 (inset of Figure 3.5(b)), more evanescent wave power (more intense blue color in the cladding) is observed in the functional cladding area compared to that for a lower index of 1.385 in the inset of Figure 3.5(a). This will consequently contribute to decreasing optical power being guided along the fiber since more power is absorbed in the functional cladding due to evanescent waves (i.e. by EWA).

In the case of the second condition or Zone II, where n_{sm} is higher than n_b but lower than n_{co2}, a different sensing mechanism occurs. Here, in parallel with EWA, there is also an additional contribution from mode losses due to the increase in critical angle in the sensing region. This is proportional to an increasing n_{sm}, as illustrated in Figure 3.6, and will induce a larger number of modes being transmitted or refracted into the external medium, hence leading to increasing mode losses. Nevertheless, there are also Fresnel reflections from rays with θ_i lower than θ_{csm} which are no longer guided by TIR. These Fresnel reflections are represented by the dotted yellow and white lines, for which the yellow rays represent rays with $\theta_i < \theta_{csm}$, subject to mode loss, while the white rays represent rays with $\theta_i \geq \theta_{csm}$ which are guided by TIR as well as subject to EWA.

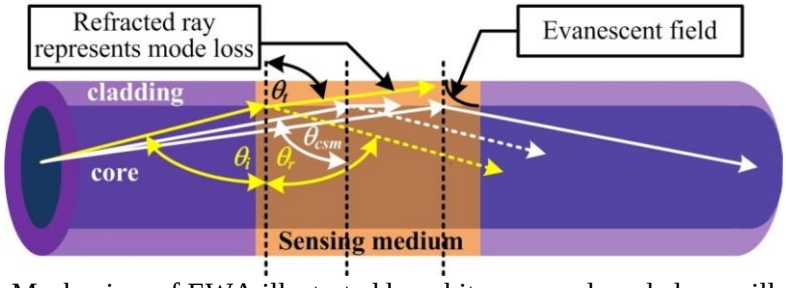

Figure 3.6. Mechanism of EWA illustrated by white rays and mode losses illustrated by yellow rays due to modification of θ_{csm} with respect to n_{sm} in Zone II.

The Fresnel reflections are very weak, and, hence, can be neglected for simplifying the model for Zone II to uniquely a combination of mode losses and EWA for rays which are still guided by TIR, similar to the first Zone. The input rays subject to EWA are thus considered from θ_{csm} to 90°. Subsequently the model for Zone II can be described by

$$P_L = \int_{\theta_{csm}}^{90^\circ} P_0(\theta_i) e^{(-N(\theta_i)T(\theta_i)L)}\, d\theta_i \tag{3.17}$$

Figures 3.7(a) and 3.7(b) illustrate the dual sensing mechanisms involved in Zone II using 2D wave optics simulation (COMSOL).

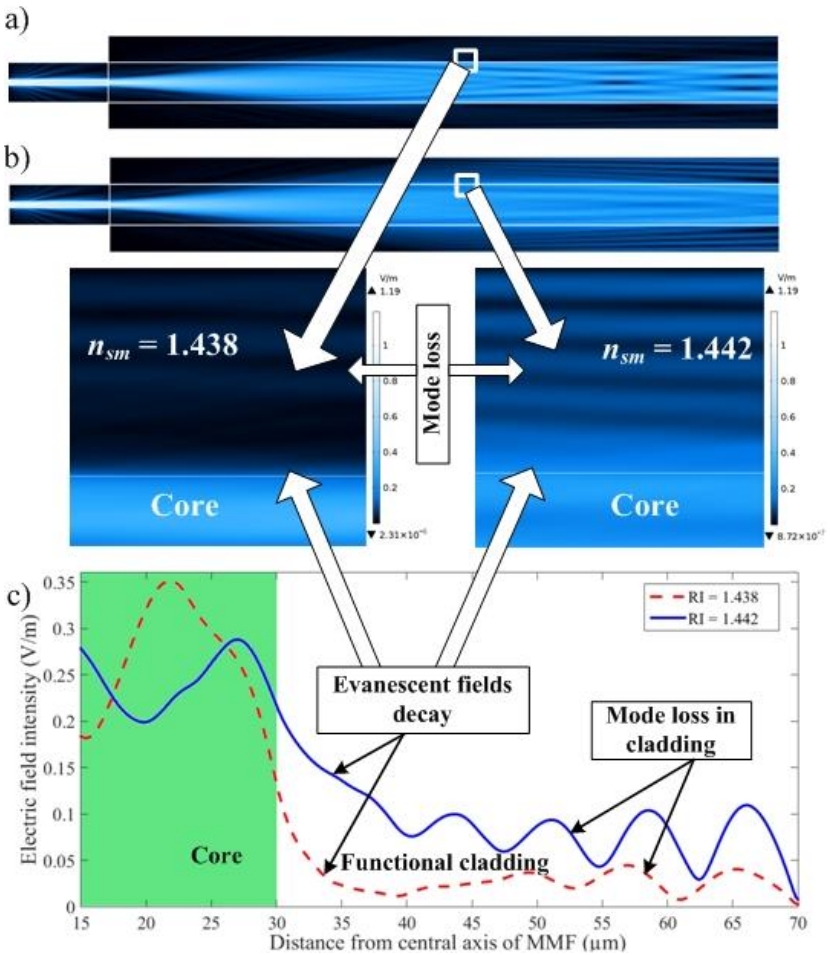

Figure 3.7. COMSOL 2D wave optics simulation of wave propagation for Zone II with a) n_{sm} = 1.438, b) n_{sm} = 1.442, and c) electric field intensity for both functional cladding indices.

Here, mode losses from the MMF core into the functional cladding (i.e. sensing or external medium) increase when the latter index is increased as a consequence of the

proportionally increasing critical angle of the sensing medium. Hence, mode losses will subsequently increase with increasing n_{sm} up to n_{co2}. Figure 3.7(b) thus shows more power being transmitted or refracted into the external medium due to its higher index when compared to the lower n_{sm} in Figure 3.7(a). In addition, evanescent waves which are generated by the rest of the rays guided along the fiber by TIR still remain at the core-external medium interface. This is evidenced from the electric field decay from the interface into the functional cladding, as illustrated by Figure 3.7(c) as well as by the insets of Figures 3.7(a) and 3.7(b).

A series of oscillating signals very akin to mode-field "interference" patterns (as if the mode fields interfere) which grow in amplitude as they penetrate further into the medium is also observed in Figure 3.7(c). This interference occurs in the external medium since during simulation, a scattering boundary condition (SBC) has been used which cannot perfectly absorb the electromagnetic waves, in particular for θ_i from 80° to almost 90°. These correspond to reflection coefficients from 25% to 90% [102], implying the loss of modes which normally exit the cladding being back-reflected into the cladding. Another observation in this RI zone (Zone II) concerns the frequency nature of the electric field intensities in the functional cladding, with the lower-index fields (n_{sm} = 1.438) oscillating at a lower frequency with respect to fields with a higher index (n_{sm} = 1.442). This could be understood by analogy to the multimode interference effect in a waveguide of relatively large lateral dimensions for which a lower index implies fewer reflections along the guide area (i.e. functional cladding in this simulation) per unit length. Hence, fewer interference can statistically occur between the propagating modes in the given medium (of n_{sm}), resulting in a series of low-frequency oscillations in the electric field intensity. A higher-index guide will, on the other hand, generate more reflections per unit length, resulting in the propagation of more refracted or transmitted modes along the guide area. A higher number of propagating modes per unit length (by reflection within the guide's radial extremity or boundary limit) are thus able to interfere, hence leading to the higher-frequency oscillations.

Finally, for Zone III, in which the sensing region of the refractometer is employed for measuring n_{sm} higher than that of the MMF core (n_{co2}), propagation by TIR is no

longer allowed. Nevertheless, some optical power will still be guided by the phenomenon of external reflection. This can be explained using Fresnel equations for the interaction of the optical rays at the interface of two media with different RI values, as illustrated in Figure 3.8.

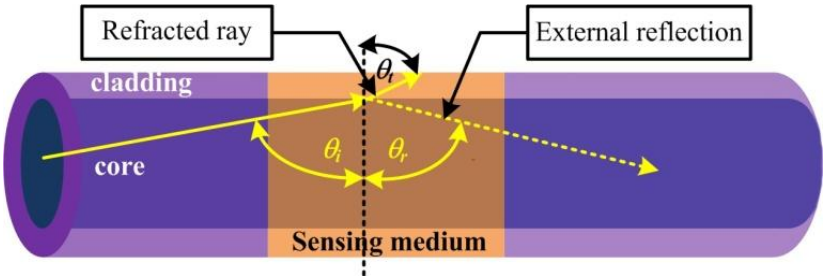

Figure 3.8. Illustration of sensing mechanism by Fresnel reflections in Zone III.

When $n_{sm} > n_{co2}$, the optical power from the core will be transmitted to the external region (sensing medium). In addition, there is also a small amount of optical power being reflected back into the core through Fresnel reflections with respect to Equations (3.19) – (3.21). The guided power in this condition can thereby be estimated by

$$P_L = \int_{\theta_b}^{90^\circ} P_0(\theta_i) R(\theta_i)^{N(\theta_i)L} d\theta_i \tag{3.18}$$

where R represents the reflectivity of the rays from θ_b to θ_{csm}, and can be calculated as a function of the reflectance under both p-polarization (r_p) and s-polarization (r_s) states, respectively, as [90]

$$R(\theta_i) = \frac{1}{2}(r_p(\theta_i)^2 + r_s(\theta_i)^2) \tag{3.19}$$

for which the reflectances under the respective polarizations are given by

$$r_p(\theta_i) = \frac{n_{sm}\cos\theta_i - n_{co2}\cos\theta_t}{n_{sm}\cos\theta_i + n_{co2}\cos\theta_t} \tag{3.20}$$

$$r_s(\theta_i) = \frac{n_{co2}\cos\theta_i - n_{sm}\cos\theta_t}{n_{co2}\cos\theta_i + n_{sm}\cos\theta_t} \tag{3.21}$$

The simulation results in Figure 3.9 clearly show that although the rays are principally transmitted or refracted to the external medium, there is still some portion of the optical power guided along the core due to external reflections when $n_{sm} >$

n_{co2}. Figure 3.9(a) shows more transmitted power in the external medium than in Figure 3.9(b), due to the presence of a lower index medium. In addition, as further demonstrated by Figure 3.9(c) as well as the insets of Figures 3.9(a) and 3.9(b), evanescent waves do not appear at the core-cladding interface, since propagation by TIR does not exist in Zone III, thus justifying the 3 sensing zone phenomena.

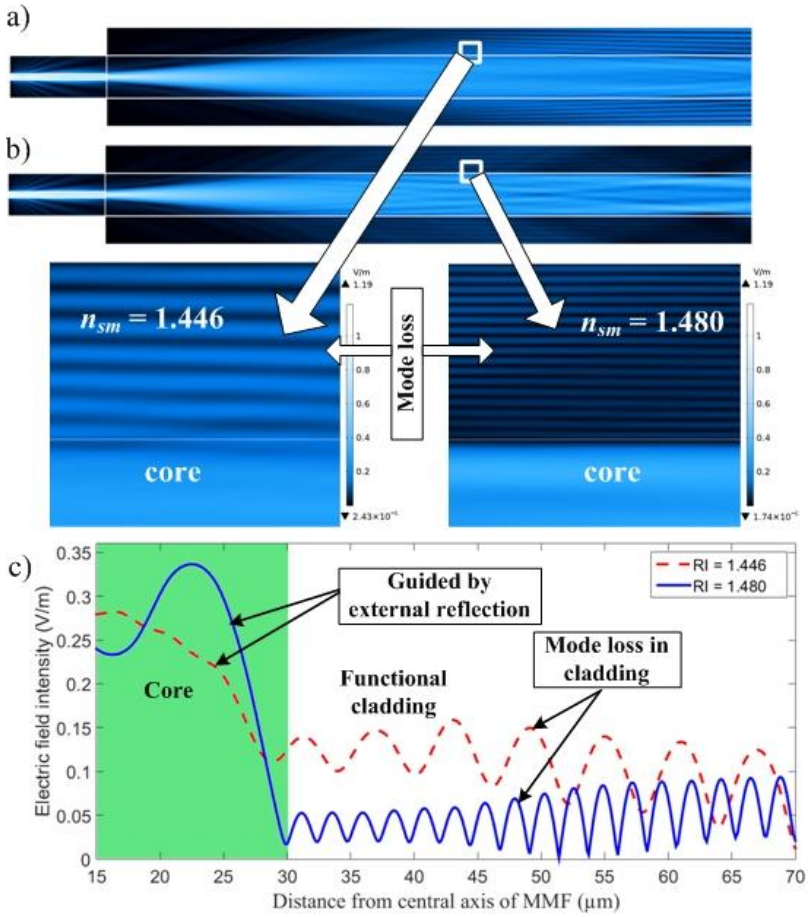

Figure 3.9. COMSOL 2D wave optics simulation of guiding mechanism in Zone III for a) n_{sm} = 1.446, b) n_{sm} = 1.480, and c) electric field intensities of both cladding indices (1.446 and 1.480).

Similar to observations made in Figure 3.7(c) of the electric field responses in Zone II, oscillations are generated in the electric field intensity of Figure 3.9(c) for both n_{sm} values and these, in particular, occur immediately after the interface and extend across the entire depth of the functional cladding region. These occur due to interference from the refracted modes since the limits of SBC exhibit reflection coefficients which are relatively high, from 25% to 90%, for corresponding incident angles from 80° to almost 90° [102]. Therefore, the loss of the modes which are

normally transmitted into and absorbed by the lossy high-index coating are back-reflected into the simulated functional cladding to induce interference along its entire length. A higher electric field intensity with a peak of ~0.15 V/m is observed for a lower n_{sm} of 1.446 RIU, while a lower peak intensity of 0.09 V/m is present for a higher n_{sm} (1.480 RIU) since more optical power is refracted when n_{sm} is close to n_{co2}, as predicted by the model for Zone III.

3.3. Experimental investigation and validation

The refractometer operates on the basis of ratiometric intensity measurement through a differential probe configuration, with one SMF-MMF serving as the sensing arm, while the other serves as the reference arm to compensate common-mode noises, as shown in Figure 3.10.

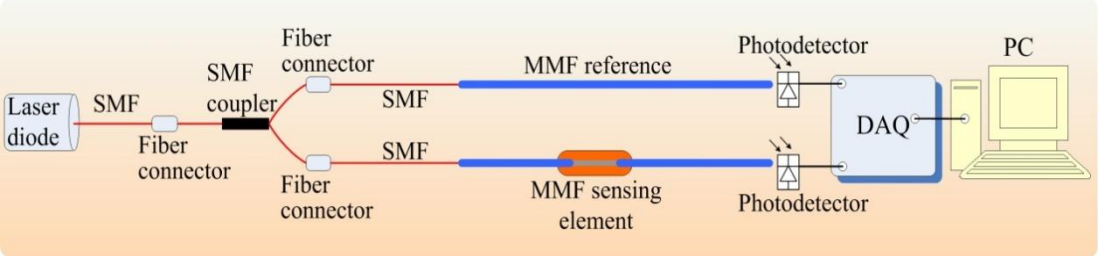

Figure 3.10. Experimental schematic of hybrid SMF-MMF refractometer for RI measurement in differential configuration for common-mode noise compensation.

The emitted beam from a 1550 nm single-mode fiber-pigtailed DFB laser diode is transmitted via a single-mode 50/50 fiber coupler to obtain two equal beams. Since the SMF is directly spliced to a Thorlabs FP200ERT MMF [103] with NA_2 = 0.50, the injected beam will be diffracted at the SMF-MMF interface, then guided into and along the latter fiber. Two identical *Ge*-type Thorlabs PDA50B photodetectors are used for measuring the guided optical powers in the fibers at their output ends. The measured data are next recorded by a dedicated National Instrument data acquisition system (DAQ) for further processing by a PC.

A combination of water-glycerol mixture with different concentrations is employed as the sensing medium to obtain a range of RI values from 1.3164 to 1.4571 RIU at 1550 nm, similar to [6]. Nonetheless, this mixing process also modifies the extinction coefficient of the glycerol-water mixture which has to be determined experimentally.

Using a linear relation, one can thus estimate the extinction coefficient of the sensing medium is given by Equation (2.30) in Chapter II. To obtain RI values beyond those of glycerol (i.e. RI > 1.4571), calibrated oils from Cargille Laboratories ranging from 1.468 to 1.608 RIU are employed.

3.4. Results and discussions

The 2D wave optic simulation results by FEM under COMSOL in Figures 3.5, 3.7, and 3.9 clearly describe three different sensing mechanisms in the hybrid SMF-MMF refractometer. However, FEM-based simulation cannot be used to support 3D MMF simulation since its dimension with respect to the operating wavelength will contribute to a very high mesh number and, thus, computational load. Hence, the most effective simulation to estimate the response of this refractometer is by combining the models from Gaussian beam analysis, ray optic principles, and the analytical equation of wave optics.

Equation (3.1) is firstly used to calculate θ_b ($\theta_b = 90°-\beta_b$), where β_b corresponds to the NA_1 value which can then be estimated using Equation (3.10) for a given MFD_{SMF}. MFD_{SMF} can, in turn, be obtained by COMSOL mode analysis as illustrated in Figure 3.3. Subsequently, the z-distance can be calculated through Equation (3.8), giving $z \cong 896.94$ µm. w_z is next calculated using Equation (3.7) for w_0 of the SMF ($w_0 = 4.85$ µm) given as $0.5MFD_{SMF}$. Subsequently, using Equations (3.11) and (3.12), the optical intensity and power at z can be obtained as shown in Figure 3.11.

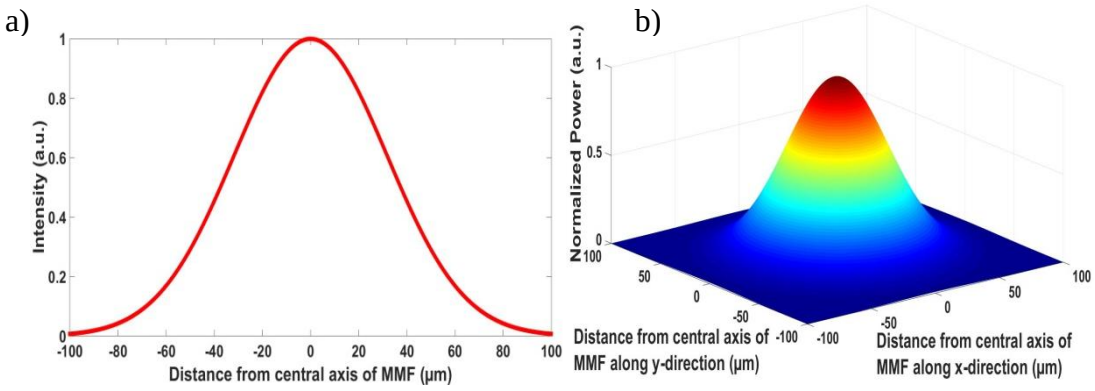

Figure 3.11. Simulated input beam characteristics at distance z, with a) the input beam intensity, and b) the input beam power at distance z in the MMF.

Inferring from the sensing principles, the boundary between Zone I and Zone II will be at an index equivalent to θ_b, due to NA_2 (MMF) being higher than NA_1 (SMF). From Equation (3.13), this boundary is determined to be at $n_b \cong 1.4351$, and, consequently, the beam from the lead-in SMF will be entirely guided by TIR for $n_{sm} < n_b$. Additionally, for estimating the guided power by the phenomenon of EWA in Zone I, as expressed by Equation (3.14), the input power distribution density $P_0(\theta_i)$ in Figure 3.12 for each angle has to be known. This is obtained using the method proposed in Chapter II for an input power distribution $P_0(\theta_i)$ from θ_b to 90°, as shown in Figure 3.12.

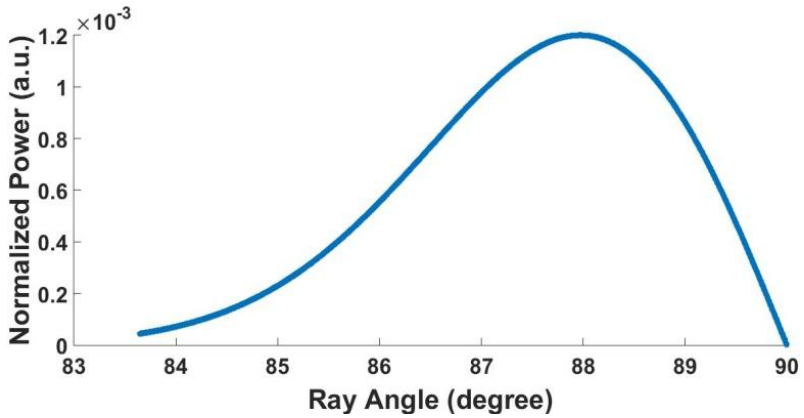

Figure 3.12. Simulated input power distribution $P_0(\theta_i)$ injected into MMF for incident angles from θ_b to 90°.

Hence, by substituting the values of $P_0(\theta_i)$ for all incident rays (from θ_b to 90°) into Equations (3.14) – (3.16), the guided power under any perturbation in Zone I, i.e. for $n_{sm} < 1.4351$ (= n_b), can thus be accurately estimated. On the other hand, for $n_{sm} > 1.4351$ and up to 1.444 (n_{co2}), the Zone II sensing response is obtained by integrating $P_0(\theta_i)$ from θ_{csm} to 90° with Equation (3.17). Finally, for Zone III, the guided power can be estimated by employing Equations (3.18), (3.19), (3.20) and (3.21) for all incident rays from θ_b to 90°. The complete simulation results of the RI response across the 3 zones are plotted and corroborated experimentally in Figure 3.13 for two sensing lengths of 2 cm and 5 cm ± 0.1 cm.

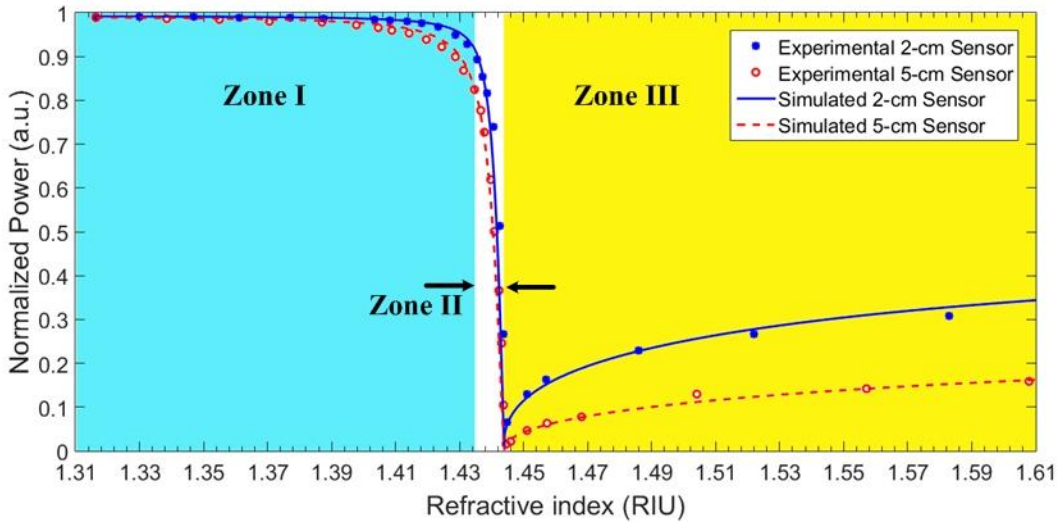

Figure 3.13. Response of refractometer based on hybrid coupling of SMF and MMF for varying RI values.

The response curves show that, in comparison with previous results in Chapter II, the dynamic range of Zone I is wider in this hybrid SMF-MMF refractometer (from 1.3164 RIU to 1.4351 RIU), contrary to Zone II, due to the injected θ_b from lead-in SMF into MMF being higher (i.e. closer to 90°). For the Zone I response, a higher power loss is achieved for the longer 5-cm sensor, and the measured optical power decreases for increasing RI due to increasing EWA as predicted by Equation (3.14).

Higher power losses are also achieved by the 5-cm sensor in Zone II since in this zone, there is still EWA which additionally contributes to the response. Furthermore, the sharp decrease in Zone II response for both the 2-cm and the 5-cm sensors results from the mode losses due to the modification of the critical angle for increasing RI values. This leads to a higher number of modes being continuously lost through refraction.

For Zone III response, the dynamic range for this zone undergoes no change compared with previous results in Chapter II since the characteristics of the MMF core are identical, i.e. PCS fiber with a silica core. However, the power response significantly increases compared to previous results in Chapter II, in particular for the shorter 2-cm sensor since the incident beam angle from lead-in SMF into MMF, θ_b, is closer to 90° compared to the previous chapter. Hence, the total number of

reflections along the sensor decreases, resulting in more power being guided along the MMF, according to Equation (3.18).

The power response curves are next derived based on the models, as a function of RI across all 3 zones, to obtain the sensitivities for both sensors as plotted in Figure 3.14.

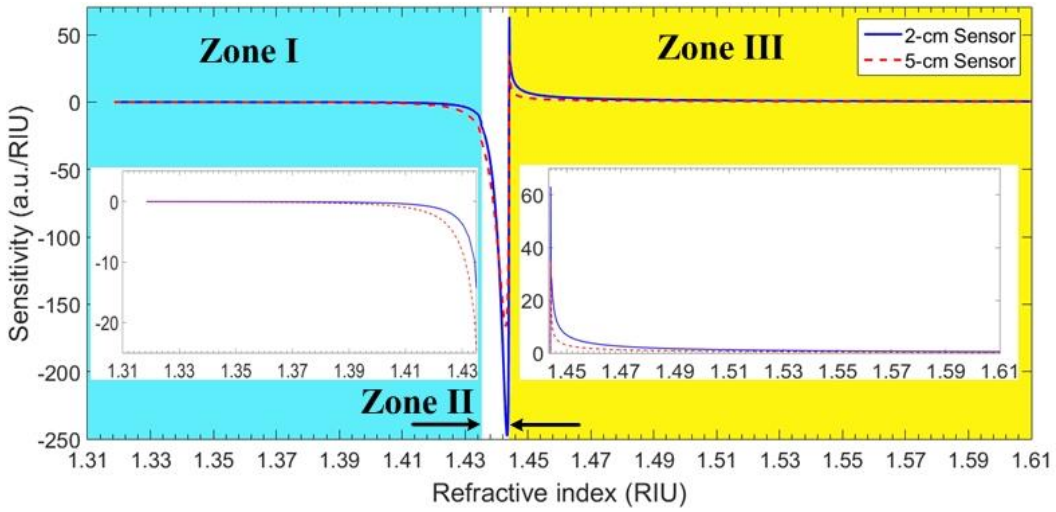

Figure 3.14. Sensitivity curves of 2-cm and 5-cm SMF-MMF hybrid refractometers.

Very high sensitivities are achieved in Zone II for both the 2-cm and 5-cm sensors, with the best sensitivity (of -248 a.u./RIU) achieved for the 2-cm stripped-cladding MMF. This is justified by the sharp decrease in the optical power response in Figure 3.13 as the shorter sensor is subject to the least EWA. Consequently, it suffers higher losses through modification of the critical angle (mode loss mechanism) as previously explained in Chapter II. This sharp decrease then declines less sharply when the measured index approaches the core index at the end of Zone II. The optical power response in Figure 3.13 then exhibits a flat response at the exact boundary between Zone II and Zone III, consequently resulting in a zero sensitivity value.

The sensitivity at the beginning of Zone I, on the contrary, is very low (-0.016 a.u./RIU and -0.0399 a.u./RIU for the 2-cm and the 5-cm sensors, respectively) since the slow gradient of the optical power response in this zone is affected by the low penetration of evanescent waves into the cladding and lower total reflection number (*NL*) along the de-cladded area. This is due to the incident beam angle into MMF

being near 90° (~83.6°). Consequently, a higher sensitivity for Zone I is achieved by a longer sensing region (5 cm) due to more EWA from a higher total reflection number in this sensor.

Further, the sensitivity curves in Zone III (Figure 3.14) describe a higher sensitivity being achieved for the 2-cm sensor. However, this sensitivity then decreases for further increasing RI. The sensitivities for the 2-cm and 5-cm sensors in Zone III are higher (22.07 a.u./RIU and 12.05 a.u./RIU) compared to the previous Zone III in Chapter II, and even when compared to the shortest (1 cm) previous sensor with a sensitivity of 1.20 a.u./RIU.

The refractometer resolution is next determined through the sensitivity curves in Figure 3.14 by taking 6 times the RMS measurement noise (6σ), corresponding to ~99.7% confidence level [100]. The best resolution in this work is 2.76×10^{-6} RIU achieved by the 2-cm sensor in Zone II. This resolution is an order of magnitude improvement over the refractometer in Chapter II where the best resolution was 2.2447×10^{-5} RIU. Further, the higher resolution for Zone III in this work is $\sim 2.83 \times 10^{-5}$ RIU, also achieved by the 2-cm sensor compared to 1.39×10^{-4} RIU for the 5-cm sensor. This is also a significant improvement compared to the resolution of the previous shortest sensor (of $\sim 1.45 \times 10^{-3}$ RIU). However, the resolution at the beginning of Zone I is 1.64×10^{-2} RIU, achieved by the 5-cm sensor, while the 2-cm sensor resolution is $\sim 3.39 \times 10^{-2}$ RIU. These resolutions are very weak compared to the best resolution of 8.34×10^{-3} RIU at the beginning of Zone I in the previous chapter, which was achieved by the 4-cm sensor. The performance of the two fiber refractometers are summarized and compared in Table 3.1 below.

Table 3.1. Performance comparison between two hybrid refractometers with different sensing lengths.

	Hybrid SMF-MMF refractometer (2 cm)			**Hybrid SMF-MMF refractometer (5 cm)**		
	Zone I	**Zone II**	**Zone III**	**Zone I**	**Zone II**	**Zone III**
Dynamic range (RIU)	1.316 -1.4351	1.4351-1.444	1.444–1.61	1.316 -1.4351	1.4351-1.444	1.444–1.61
Resolution (mRIU)	33.9	0.00276	0.0283	16.4	0.00397	0.139

3.5. Conclusion

Two hybrid SMF-MMF fusion splice-coupled refractometers have been realized to reduce mechanical perturbations as well as, in particular, to improve the sensitivity in Zone II and Zone III. Since the injected beam angle from the lead-in SMF corresponds to its *NA*, this then determines the equivalent angle to the RI value for the boundary between Zone I and Zone II. Accordingly, the ray power distribution density which propagates along the MMF can theoretically be obtained using Gaussian beam analysis. Subsequently, the optical power response for both the 2-cm and 5-cm refractometers can be estimated by applying the ray power distribution into the model for Zone I and Zone II through ray optic principles and the analytical equation for evanescent waves, while the model for Zone III employs the ray power distribution density combined with Fresnel equations.

The simulation results for the three sensing zones have been corroborated experimentally by de-cladding two MMFs over 2 cm and 5 cm in length, respectively, demonstrating very high agreement. In addition, since the incident beam angle (θ_b) from lead-in SMF is very close to 90°, the range of Zone II is consequently very narrow (1.4351 to 1.444 RIU), compared to the relatively wider range obtained in Zone I.

In terms of sensitivity, the results achieved with these hybrid SMF-MMF splice-coupled refractometers show significantly improved sensing performance by more than 8 and 51 times, in particular for the shorter 2-cm sensor in Zones II and III, respectively, compared to previous results in Chapter II. On the contrary, the sensitivity at the beginning of Zone I is very low (-0.016 a.u./RIU and -0.0399 a.u./RIU for the 2-cm and the 5-cm sensing lengths, respectively) while previous results in Chapter II exhibited a sensitivity of -0.392 a.u./RIU for the 4-cm sensor (which increased exponentially with increasing RI until the limit between Zone I and Zone II, as the described by the model for Zone I in Equation (3.14)). Nevertheless, to increase the sensitivity in Zone I, stronger EWA will be required. This potential improvement to the overall performance of the fiber refractometers will be discussed in Chapter IV.

CHAPTER IV

All-Fiber Hybrid Refractometer using Photonic Crystal Fibers

4.1. Introduction

The photonic crystal fiber (PCF), known also as micro-structured optical fiber (MOF), is a more recent class of optical fiber whose theoretical concept and propagation characteristics have been reported by Birks *et al.* [104]. The PCF was inspired from the planar photonic crystal (PC) waveguide which can guide lightwaves over a certain wavelength range by exploiting the photonic bandgap (PBG) mechanism [105]. Theoretically, the hollow-core PCF enables to guide the lightwaves with an effective index less than 1 ($n_{eff} < 1$) by PBG across a certain wavelength range and can potentially be a good candidate as gas sensors [104, 106].

However, the very first PCF fabricated was a solid-core PCF which did not support light guiding defined by PBG [107]. This solid-core PCF can guide the lightwaves within the core by modified total internal reflection (MTIR) with n_{eff} close to the silica index (n_{SiO2}) used as the core material. MTIR is similar to total internal reflection (TIR) in a conventional step-index (SI) fiber, in which the functional cladding index is replaced by the fundamental space-filling mode index (n_{FSM}) of the periodic cladding structure. Due to MTIR, the solid-core PCF allows propagation of the lightwaves in single-mode within the core over a broad wavelength range, from at least 458 nm to 1550 nm, despite the core diameter being bigger than a typical single-mode fiber (SMF) core [107-108] when the ratio between the air-hole diameter d and the hole-to-hole spacing Λ is inferior to 0.43 (i.e. $d/\Lambda \leq 0.43$). In addition, the solid-core PCF can guide single-mode laser radiation with a mode field diameter (*MFD*) which is smaller than the diameter of the core, while the MFD of the SI SMF is always bigger than that of the core [109]. This consequently leads to less evanescent waves penetrating into the PCF cladding, and, hence, less confinement loss occurring along the PCF.

Since its first successful fabrication, numerous researchers have been intensively involved in the study of the PCF characteristics, as well as its application areas, in particular for sensing applications. Numerous sensors have been developed using PCFs such as for displacement/strain measurements [110-113], temperature sensing [114-116], pressure measurements [117-120], as well as for bio-chemical [121-124] and gas detection [125-130]. Most PCF-based sensors require the introduction of measurands (gas or aqueous solution) into the air-hole micro-structure and/or the hollow core used as the sensing region. The presence of these measurands can be detected by measuring the absorption spectrum of the guided optical power in the hollow core [127-130] or by measuring the transmission power which is affected by evanescent waves in the micro-structured cladding (inner cladding) [125, 126, 131]. However, this technique is not highly efficient since the measurand has to be injected first into the air-holes of the hollow-core of the PCF and then continuously drained out during measurements. The fiber and, in particular, the air-holes then have to be cleaned each time for re-use, which not only significantly reduces the operating frequency of the system but also requires tedious additional steps to prepare the device for further operations.

As a consequence, the solid-core PCF is exploited in this chapter to improve evanescent wave absorption (EWA) in the outer cladding area (outer silica region) instead of EWA in the inner cladding zone (air-hole micro-structure). Here, the laser beam is injected mainly into the cladding area (inner and outer cladding), with only a small portion of the beam guided within the core. Consequently, most of the light is guided within the outer cladding region. Furthermore, with a very thin outer cladding thickness, several-fold increase in EWA can be achieved. The sensitivity of evanescent wave-based PCF sensors can consequently be increased, in particular for an all-fiber (or hybrid) sensor system in which the injected beam angle incident at the target PCF's outer diameter from the lead-in fiber can be made to be closer to 90°.

In an all-fiber SMF-MMF scheme, the incident beam angle (θ_b) of the sensor depends principally on the numerical aperture (*NA*) of the SMF, with the radiated beam angle (β_b) usually being less than 10° or, equivalently, the incident beam angle arriving at the outer diameter ($\theta_b = 90° - \beta_b$) being close to 90°. This consequently

results in a lower number of reflections along the sensitive outer region, thus inducing less EWA along the sensor. A lower sensitivity has been found in Zone I as demonstrated in Chapter III, i.e. the sensing regime in which the power response is affected only by EWA. On the other hand, an all-fiber hybrid system can improve the sensitivity in Zone II (defined as the regime in which the sensing mechanism is a combination of EWA and mode losses concurrently) and Zone III (regime affected only by Fresnel reflections for a sensing medium index (n_{sm}) higher than the MMF core index), compared to the results (see Chapter II) obtained when the beam is launched using microscope objectives. In addition, an all-fibered sensor configuration is less prone to mechanical vibrations while concurrently offering high flexibility in the experimental set-up.

To increase EWA in the outer cladding of the PCF, an SMF is first coupled to a multimode fiber (MMF_1) which, in turn, is spliced to a solid-core PCF serving as the sensing region. The MMF_1 core diameter must be larger than the inner cladding diameter of the PCF to enable (some) light or rays from MMF_1 to be injected into the outer cladding (outer silica region) of PCF as illustrated in Figure 4.1. Rays which fall within the acceptance angle of PCF and penetrate into the outer cladding (see the red ray in Figure 4.1) can be propagated in the outer cladding region if the surrounding medium index (or n_{sm}) is lower than the silica index (n_{SiO2}). This can occur when the outer cladding region is made of the same silica material as the PCF core having an index (n_{SiO2}) higher than that of the inner cladding (n_{FSM}) of the PC structure. Hence, light can be propagated within the outer cladding region when its radiated angle is lower than the PCF's acceptance angle, β_{PCF}, and $n_{sm} < n_{SiO2}$. This will subsequently contribute to higher EWA since the thickness of this region is relatively thin compared to the MMF or PCF diameter. The second extremity of the PCF is next coupled to a second MMF (MMF_2) by fusion splicing. Here, the core diameter of MMF_2 must be equal to or larger than the PCF's outer diameter in order to efficiently collect all the guided optical power from the PCF core as well as cladding.

In this chapter, a theoretical model of the PCF refractometer will be proposed and described. This is subsequently corroborated experimentally to validate the expected

higher rate of EWA obtained with this sensing approach using a configuration illustrated in Figure 4.1, in comparison with the previously proposed hybrid SMF-MMF scheme.

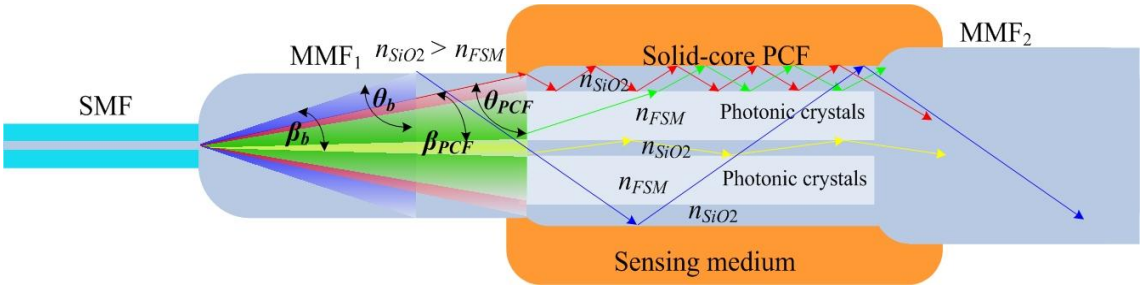

Figure 4.1. All-fibered PCF-based sensor scheme to increase EWA by injecting the lightwave into the outer silica cladding of the solid-core PCF.

Figure 4.1 shows the guiding mechanism in the all-fiber-based PCF sensor. Rays outside β_{PCF}, i.e. with radiated angles (β_i) > β_{PCF} (see blue ray), will cross the PC structure and be guided along the PCF. For rays within β_{PCF}, there are 3 possibilities, i.e. the rays will (1) penetrate into the outer cladding and be guided within the outer cladding as represented by the red line in Figure 4.1; (2) penetrate the inner cladding and subsequently be refracted into the outer cladding to be guided within the outer cladding (see green ray in Figure 4.1); and (3) reach the core and be guided within the PCF core by MTIR as illustrated by the yellow ray in Figure 4.1. Mathematical models to represent this physical phenomenon and the sensor response to variation in the sensing medium index (n_{sm}) will be discussed in the following sections.

4.2. Sensing mechanism and modeling

4.2.1. Determination of *MFD* and *NA*

The guiding mechanism in a solid-core PCF, shown in Figure 4.2(a), by MTIR is similar to TIR in an SI fiber. In the solid-core PCF, the functional cladding is replaced by n_{FSM} as the equivalent inner cladding index of the PC structure. Hence, the effective index n_{eff} (β/k) of the propagating mode in a solid-core PCF is bounded by

$$n_{FSM} < n_{eff} < n_{SiO_2} \tag{4.1}$$

Here, n_{FSM} can be determined using the FEM solver in COMSOL Multiphysics by employing the boundary conditions given in Table 4.1. These are applied to an elementary unit of the air-hole lattice structure to find the corresponding mode in both polarizations (x and y) [132].

Table 4.1. Boundary conditions to calculate n_{FSM} using perfect magnetic conductor (PMC) and perfect electric conductor (PEC) limits [132].

Polarization	**Γ_1 and Γ_2**	**Γ_3 and Γ_4**
x	PMC	PEC
y	PEC	PMC

The corresponding mode of the PC structure, illustrated in Figure 4.2(b), represents the cladding index of the PCF. Subsequently, the PCF structure can be represented by an equivalent model shown in Figure 4.2(c).

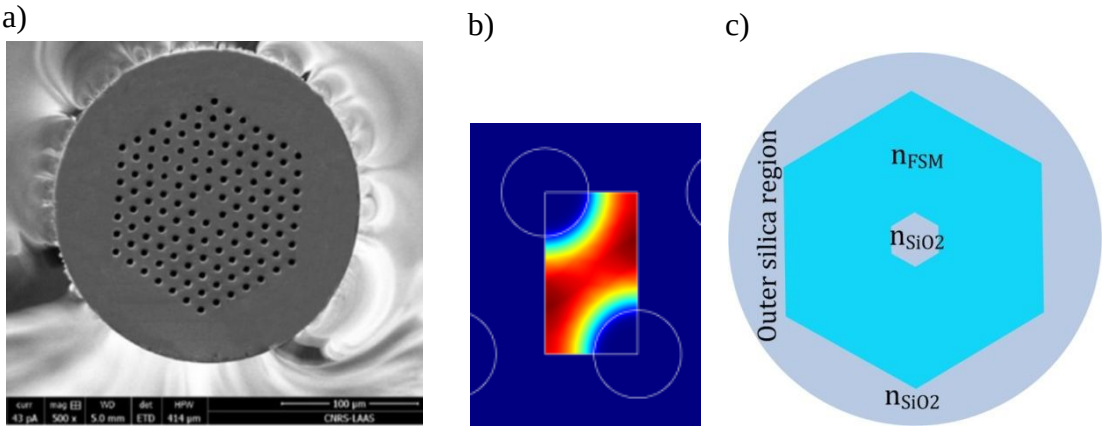

Figure 4.2. Transformation of PCF's cross-section for a) ESM-12 (Thorlabs) PCF cross-section, with b) n_{FSM} as cladding index obtained by COMSOL simulation of an elementary lattice, into c) equivalent PCF form where triangular air-hole lattice is represented by n_{FSM}.

Therefore, the lightwave for which the injection angle into the PCF core is less than or equal to its acceptance angle (β_{PCF}) can be guided in the core. B_{PCF} is a function of the PCF's numerical aperture NA_{PCF} (= n_{SiO2} sin β_{PCF}) which corresponds to an *MFD* (MFD_{PCF}) given by

$$NA_{PCF} \cong \frac{\lambda}{MFD_{PCF}} \tag{4.2}$$

This MFD_{PCF} value can be estimated by taking the 1/e intensity distribution diameter of the fundamental mode obtained by COMSOL as illustrated in Figures 4.3(b) and

4.3(c), for an LMA-20 PCF from Thorlabs, Inc. with a PC structure illustrated by Figure 4.3(a). Thus, for this fiber with air-hole and pitch diameters (d and Λ) of 5.9 µm and 12.6 µm respectively, as shown in Figure 4.3(a), an MFD_{PCF} of 17.33 µm is obtained. This corresponds to NA_{PCF} ~0.089 and an acceptance angle, β_{PCF}, of 3.55°. The incident angle that can be accepted by the PCF is thus given by θ_{PCF} (= 90°-β_{PCF}) of 86.45°.

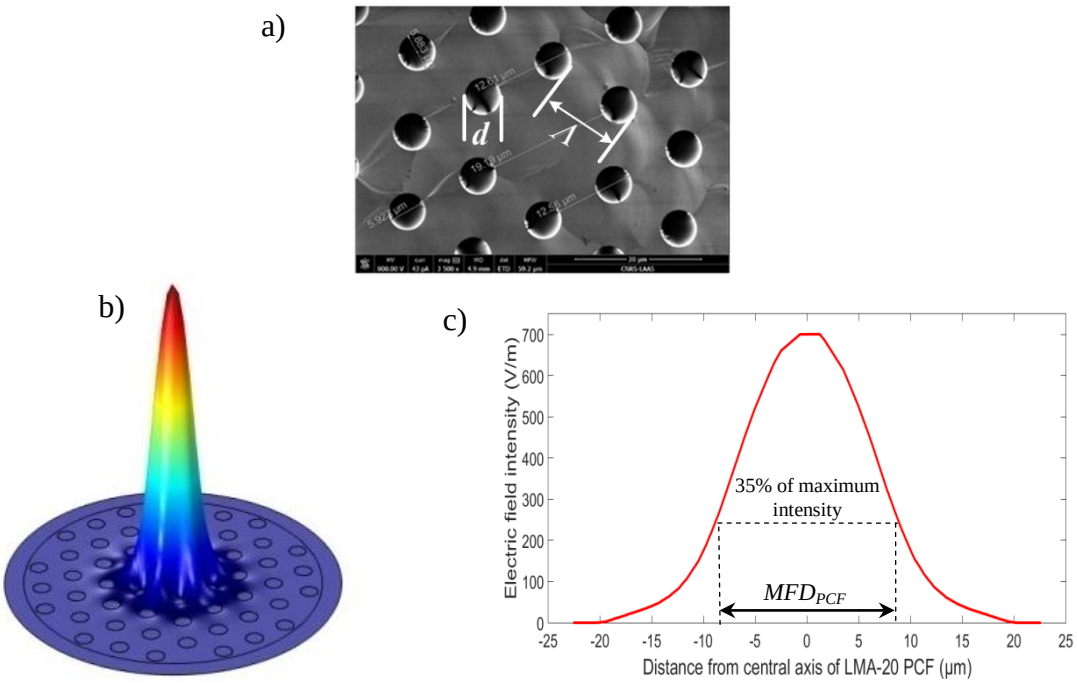

Figure 4.3. a) SEM image of LMA-20 PCF, b) its fundamental mode, and c) electric field distribution of fundamental mode.

In the case of the ESM-12B PCF, another variant of the solid-core PCF, with d ~3.5 µm and Λ ~7.7 µm as illustrated in Figure 4.4(a), the simulated electric field intensity of the fundamental mode is plotted in Figure 4.4(b).

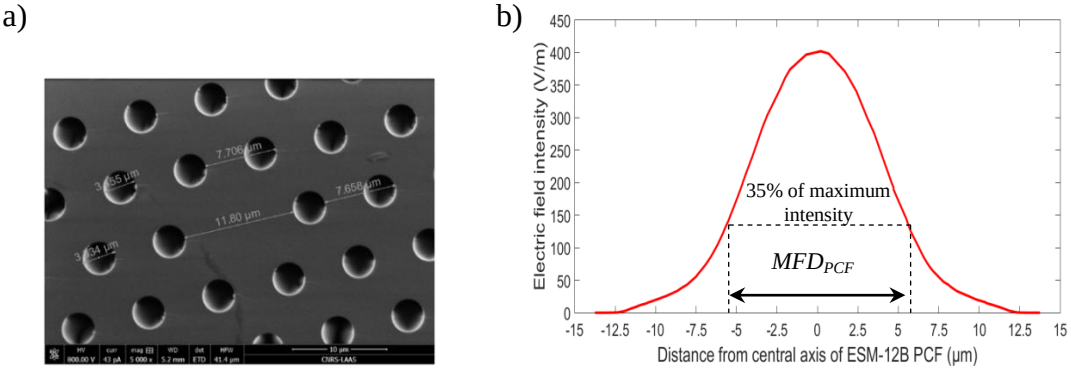

Figure 4.4. ESM-12B PCF: a) cross-section of ESM-12B PCF, and b) electric field intensity of its fundamental mode.

According to the simulation result in Figure 4.4(b), MFD_{PCF} of the ESM-12B PCF is ~11.12 µm which corresponds to NA_{SMF} ~0.14 , β_{PCF} ~5.54° and θ_{PCF} ~84.46°.

4.2.2. All-fiber PCF sensing mechanism and modeling

Enhancing EWA by exploiting a solid-core PCF in an all-fiber scheme can effectively be realized by injecting the lightwave into the outer cladding of the PCF as initially proposed in Figure 4.1. The radiated beam from lead-in SMF propagated into MMF_1 will remain guided within the PCF. Some portion of the beam, for which $\beta_i > \beta_{PCF}$, cannot be confined and guided in the core as illustrated by the blue ray in Figure 4.1. However, this beam can still be guided along the PCF by TIR, albeit not in the core, when the surrounding medium index n_{sm} is lower than the equivalent index at critical angle (see blue line in Figure 4.1). On the other hand, for another portion of the beam with radiated angles (β_i) lower than β_{PCF}, light can be guided within the outer silica cladding if the beam can penetrate the cladding (inner and outer cladding) as illustrated by the red and green lines in Figure 4.1, while the beam which penetrates the core (the yellow ray in Figure 4.1), i.e. respecting the β_{PCF} condition, will be guided within the PCF core.

The power response of the sensor varies accordingly with the target n_{sm} which conditions the propagation of the blue, red, and green rays (see Figure 4.1). The sensing mechanism is uniquely induced by EWA (in Zone I) for n_{sm} less than the equivalent index for the incident beam angle (n_b), as previously explained in Chapter III. According to the hybrid fiber system shown in Figure 4.1, the sensor response in Zone I can be estimated by

$$P_L = \int_{\theta_b}^{\theta_{PCF1}} P_0(\theta_i) e^{(-N(\theta_i)T(\theta_i)L)}\, d\theta_i + \int_{\theta_{PCF1}}^{\theta_{PCF2}} P_0(\theta_i) e^{(-N_{ex}(\theta_i)T(\theta_i)L)}\, d\theta_i + \int_{\theta_{PCF2}}^{\theta_{PCF3}} P_0(\theta_i) e^{(-N_{ex}(\theta_i)T(\theta_i)L_i)}\, d\theta_i + \int_{\theta_{PCF3}}^{90°} P_0(\theta_i)\, d\theta_i \quad (4.3)$$

where θ_{PCF1}, θ_{PCF2}, and θ_{PCF3} represent the rays angles which are within the PCF acceptance angle and such that all the rays in between $\theta_{PCF1} < \theta_i < \theta_{PCF2}$, $\theta_{PCF2} < \theta_i < \theta_{PCF3}$, and $\theta_{PCF1} < \theta_i < 90°$ reach the outer cladding, the inner cladding, and the PCF

core, respectively. N and N_{ex} are the number of reflections along the PCF and the number of reflections along the outer silica cladding respectively. N can be expressed as

$$N(\theta_i) = \frac{\cot\theta_i}{2a_{PCF}} \tag{4.4}$$

where a_{PCF} represents the PCF radius. On other hand, N_{ex} is given by

$$N_{ex}(\theta_i) = \frac{\cot\theta_i}{2a_{cl2}} \tag{4.5}$$

with a_{cl2} the outer cladding radius (thickness) of the PC structure (see Figure 4.5(c)). The PC structure serves as the inner cladding which has a hexagonal form with a radius of a_{cl1} as represented in Figure 4.5I. This structure can, however, be approximated by a circular form to simplify the model from Figure 4.1 by adapting the method proposed by Birks *et al.* [108]. This subsequently transforms the hexagonal structure in Figure 4.5(a) into a circular structure illustrated by Figure 4.5(b).

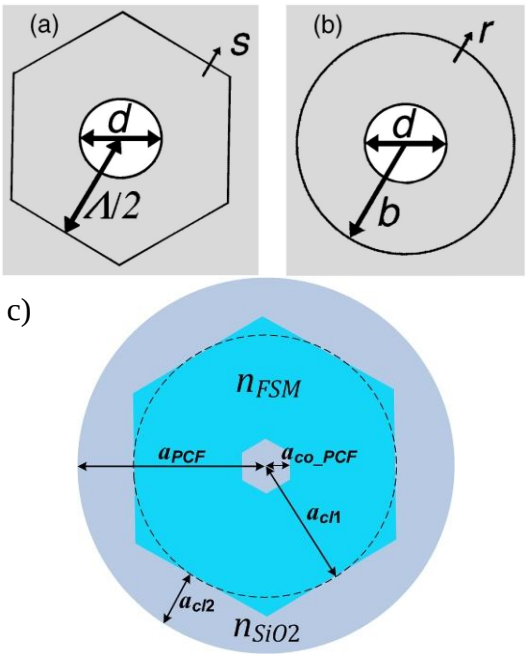

Figure 4.5. Circular approximation of hexagonal form of photonic crystal structure, where a) hexagonal form [108] is transformed approximately into b) circular form [108], and c) hexagonal form of PC structure approximated as circular form.

The transmission coefficient T of the penetrating evanescent waves into the sensing medium, previously given by Equations (2.9) in and (2.10) Chapter II, can be re-employed here.

Thus, for a PCF section illustrated in Figure 4.6, L represents the PCF sensor length, while L_i is the length of the PCF sensing area for rays within acceptance angles θ_i which reach and penetrate into the inner cladding, and are then guided within the outer cladding. L_i can be mathematically calculated by

$$\begin{aligned} L_i &= L - L_{xi} \\ L_i &= L - (a_{cl1} - a_y)\tan\theta_i \end{aligned} \tag{4.6}$$

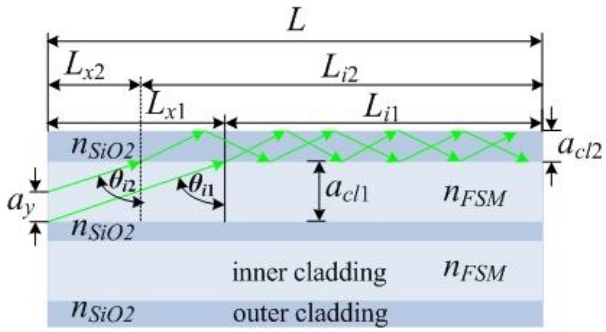

Figure 4.6. Illustration of PCF sensing region for rays which are injected via inner cladding of PC structure.

Equation (4.3) describes the physical mechanisms for light-guiding within the PCF whose input end is coupled by fusion splicing to both an MMF and an SMF in the order illustrated by Figure 4.1. The first term on the right of Equation (4.3) defines EWA which occurs for rays with incident angles which are higher than β_{PCF}, represented by the blue ray in Figure 4.1. The second term represents EWA for rays with radiated angles lower than β_{PCF} and which penetrate into the outer cladding (i.e. red ray in Figure 4.1). The third term, on the other hand, represents EWA for rays with incident angles lower than β_{PCF} but which are transmitted into the inner cladding, and then subsequently guided within the outer cladding, as illustrated by the green ray in Figure 4.1. The last term in Equation (4.3) describes the remaining beam which is guided within the core of the PCF. This does not reach the sensing zone and thus cannot be affected by variations in n_{sm}. Consequently, the second and third right terms in Equation (4.3) define the contributions to any eventual increase in

EWA since the rays under these conditions have a higher number of reflections due to a relatively thinner outer cladding layer.

The mathematical model in Equation (4.3) can be employed when n_{sm} is lower than the equivalent index n_b defined by the incident beam angle θ_b which is given by

$$n_b = n_{SiO_2} \sin\theta_b \tag{4.7}$$

When n_{sm} becomes slightly higher than n_b, some modes which are not guided within the core will be lost through refraction into the sensing medium if its incident angles $\theta_i < \theta_{csm}$. The remaining modes will still be guided both within the PCF and within the outer cladding PCF for $\theta_i \geq \theta_{csm}$, thereby resulting in evanescent waves being induced at the interface between the fiber and the sensing medium. Under this condition (Zone II), two concurrent sensing mechanisms thus occur, i.e. mode losses and EWA for which rays are still guided and reach the sensing medium. This phenomenon is similar to the Zone II behavior in the MMF refractometer.

In the all-fiber PCF sensor, however, the mathematical model for Zone II operation is divided into two complementary sub-models. The first of these determines the power response for which n_{sm}, with a corresponding angle θ_{csm}, is both higher than n_b and lower than the equivalent index (n_{PCF}) to θ_{PCF}. The values of θ_{csm} and n_{PCF} can be obtained by Snell's law as

$$\theta_{csm} = \sin^{-1}\left(\frac{n_{sm}}{n_{SiO_2}}\right) \tag{4.8}$$

$$n_{PCF} = n_{SiO_2} \sin\theta_{PCF} \tag{4.9}$$

The first sub-model for Zone II can subsequently be given by

$$\begin{aligned} P_L = &\int_{\theta csm}^{\theta_{PCF1}} P_0(\theta_i) e^{(-N(\theta_i)T(\theta_i)L)}\, d\theta_i + \int_{\theta_{PCF1}}^{\theta_{PCF2}} P_0(\theta_i) e^{(-N_{ex}(\theta_i)T(\theta_i)L)}\, d\theta_i \\ &+ \int_{\theta_{PCF2}}^{\theta_{PCF3}} P_0(\theta_i) e^{(-N_{ex}(\theta_i)T(\theta_i)L_i)}\, d\theta_i + \int_{\theta_{PCF3}}^{90^\circ} P_0(\theta_i)\, d\theta_i \end{aligned} \tag{4.10}$$

The second sub-model estimates the power response for which $n_{sm} > n_{PCF}$ and up to n_{SiO2}. In this case, the portion of the beam which is not within β_{PCF} is no longer

guided along the PCF (i.e. the blue ray in Figure 4.1 no longer exists within the PCF). Consequently, the first term on the right of Equation (4.10) can be eliminated since the beam angle $\beta_b > \beta_{PCF}$ (i.e. the portion of the beam from θ_b to θ_{PCF} is lost to the sensing medium), thus simplifying into

$$P_L = \int_{\theta_{csm}}^{\theta_{PCF2}} P_0(\theta_i) e^{(-N_{ex}(\theta_i)T(\theta_i)L)}\, d\theta_i + \int_{\theta_{PCF2}}^{\theta_{PCF3}} P_0(\theta_i) e^{(-N_{ex}(\theta_i)T(\theta_i)L_i)}\, d\theta_i + \int_{\theta_{PCF3}}^{90^\circ} P_0(\theta_i) d\theta_i \quad (4.11)$$

To further verify the PCF guiding mechanisms as explained above, an SMF is first coupled to a solid-core ESM-12B type PCF by fusion splicing. The objective is to confirm that the portion of the beam with $\beta_b > \beta_{PCF}$ (= 90°-θ_{PCF}) will be transmitted or refracted through the first cladding layer to finally reach the outer cladding of the PCF. This will subsequently be guided along the PCF by TIR across the inner and outer cladding when $n_{sm} < n_b$, as illustrated by the yellow line in Figure 4.7.

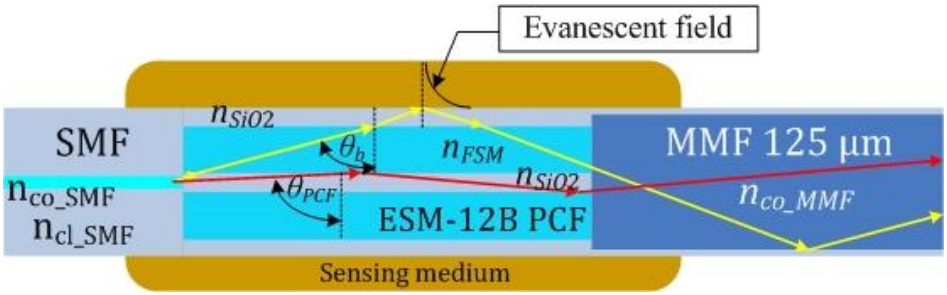

Figure 4.7. Illustration of coupling losses occurring for SMF coupled to ESM-12B type PCF using 125 µm MMF to recover the optical signal, with $NA_{SMF} > NA_{PCF}$ or for beam angles lower than θ_{PCF} as represented by the yellow ray.

Here, for NA_{SMF} (~0.16) > NA_{PCF} (~0.14), rays from lead-in SMF which are radiated into ESM-12B with $\theta_b < \theta_{PCF}$ will be refracted into the inner and outer cladding as illustrated in Figure 4.7. These refracted rays then reach the outer cladding and the sensing medium interface. Subsequently, ray guidance by TIR along ESM-12B PCF across its inner and outer cladding will induce evanescent waves at the interface between the outer cladding region and the sensing medium (see yellow ray in Figure 4.7). This can only occur under the condition that the induced equivalent critical angle due to the presence of the sensing medium θ_{csm} be lower than the incident ray angles θ_i.

Therefore, the complete model to estimate the total guided optical power corresponds to a combination of the guided power in the ESM-12B core by MTIR for rays with $\theta_{PCF} < \theta_i < 90°$, and for all the other refracted beams with $\theta_b < \theta_i < \theta_{PCF}$. These latter beams are affected by EWA which consequently reduces the optical power transmitted to the end of the fiber. This is similar to the mechanism present in Zone I in the MMF based-refractometer, as previously explained in Chapters II and III. The resulting total guided power can thus be given as

$$P_L = \int_{\theta_{PCF}}^{90°} P_0(\theta_i) d\theta_i + \int_{\theta_b}^{\theta_{PCF}} P_0(\theta_i) e^{(-N(\theta_i)T(\theta_i)L)} d\theta_i \tag{4.12}$$

However, when n_{sm} increases such that the associated θ_{csm} becomes higher than θ_b, mode losses will be induced for the refracted beam or rays with angles less than θ_{csm}. The remaining refracted rays with $\theta_{csm} < \theta_i < \theta_{PCF}$ are still guided by TIR within ESM-12B, across the inner and outer cladding (see yellow ray in Figure 4.7) and will thus be subject to EWA in the sensing medium. This will further reduce the optical power transmitted to the end of the fiber. On the other hand, the beam which is within the PCF's acceptance angle (i.e. from θ_{PCF} to 90°) is guided within the ESM-12B core by MTIR. Hence, for $\theta_{csm} > \theta_b$, the optical power losses are induced by both the losses due to the reduction of propagation modes and EWA of the refracted rays (i.e. from θ_b to θ_{csm}). Consequently, the optical power guided along the fiber can be expressed mathematically as

$$P_L = \int_{\theta_{PCF}}^{90°} P_0(\theta_i) d\theta_i + \int_{\theta_{csm}}^{\theta_{PCF}} P_0(\theta_i) e^{(-N(\theta_i)T(\theta_i)L)} d\theta_i \tag{4.13}$$

Hence, maximum losses occur when n_{sm} is equal to n_{SiO2}, resulting in all refracted rays being rejected from the PCF toward the sensing medium surrounding the external diameter of the fiber. The remaining optical power for rays between θ_{PCF} and 90° is, however, guided in the ESM-12B core. This condition is determined as the coupling losses of the SMF fusion-spliced to ESM-12B due to the higher *NA* of the SMF which radiates the beam with $\beta_b > \beta_{PCF}$. This will lead to a portion of the beam between β_{PCF} and β_b (i.e. $\beta_{PCF} < \beta_i < \beta_b$) being lost to exterior.

4.3. Results and discussions

4.3.1. Fusion splicing of SMF-ESM-12B PCF-MMF

To validate the principle of the guiding mechanisms in the solid-core PCF previously described in Figure 4.7, an SMF is fusion-spliced to one end of ESM-12B PCF the outcome of which is illustrated in Figure 4.8. The lossy high-index polymer coating of ESM-12B is first removed thermally before the fusion splicing process. Although effort has been made to sufficiently adjust the fusion power to avoid a collapse in the air-holes at the SMF-ESM-12B interface, slight deformation, however, occurred in the PC structure, as shown in Figures 4.8(a) and 4.8(b). This can potentially result in undesired mode field excitation in the ESM-12B cladding.

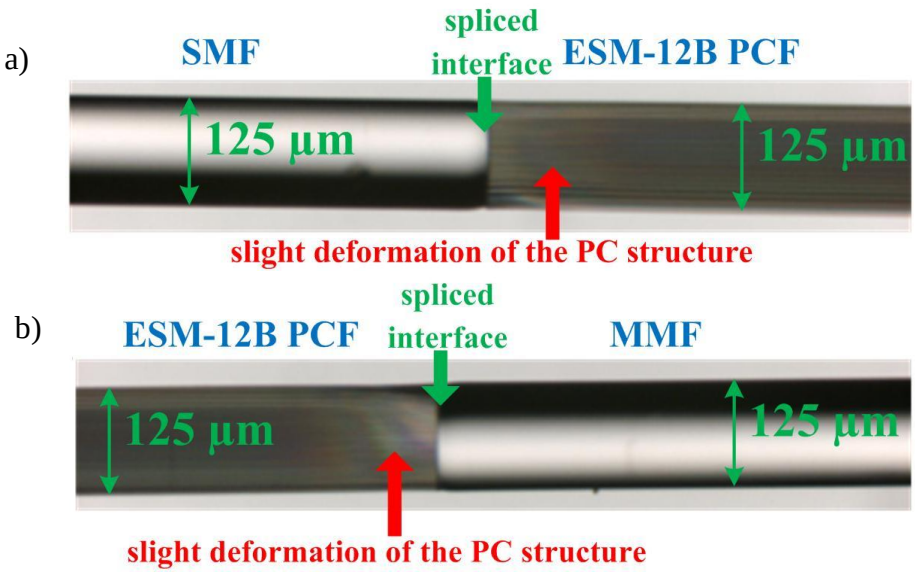

Figure 4.8. Fusion splicing between ESM-12B and step-index fiber, a) SMF spliced to ESM-12B, b) ESM-12B spliced to MMF with diameter of 125 µm.

The other extremity of ESM-12B PCF is spliced to an MMF with a 125-µm diameter for light collection purposes. This hybrid fiber sensing structure is then immersed into a sensing medium with n_{sm} for characterization using a differential set-up scheme illustrated in Figure 4.9.

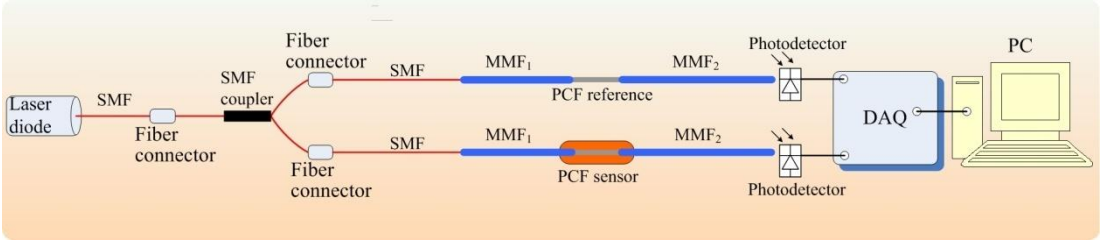

Figure 4.9. Experimental set-up of hybrid SMF-ESM-12B-MMF sensing architecture in differential configuration.

To investigate the loss mechanism at the splice induced by the refracted beam beyond θ_{PCF}, a variation in the glycerol-water solute concentration from 0% to ~91.3% has been carried out. This enables n_{sm} to be varied from 1.3164 to 1.444 RIU at 1550 nm [6]. The various solute parameters have been determined in accordance with the procedure in Section 2.4 of Chapter II. Here, the principal parameter contributing toward the absorption of evanescent waves at the sensing medium-ESM-12B interface is again the solute's absorption coefficient α_{mix} as described by Equation (2.29). These waves are generated by the refracted rays from θ_b to θ_{PCF}, as predicted by Equations (4.12) and (4.13).

Since the beam is radiated from the same SMF type as in Chapter III, the same radiated optical power density, illustrated in Figure 4.9, can therefore be employed. Rays from θ_b = 83.638° to θ_{PCF} = 84.46° (red shaded area in Figure 4.10) are then refracted towards a 5-cm long ESM-12B cladding and will subsequently reach the interface between its outer cladding and the sensing medium. These will be totally reflected and guided along ESM-12B by TIR. Additionally, they will also be subject to EWA, similar to Zone I in the MMF-based refractometer in Chapters II and III, when $n_{sm} < n_b$. The remaining beam from θ_{PCF} = 84.46° to 90° (represented by the unshaded area in Figure 4.10) will, however, be guided in the ESM-12B core and thus will not be affected by any n_{sm} variation.

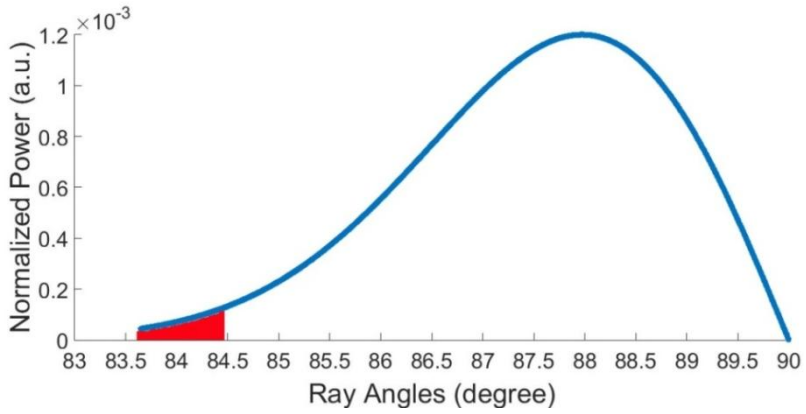

Figure 4.10. Simulated angular power distribution density radiated from lead-in SMF to ESM-12B PCF from θ_b to 90°.

Both the refracted and guided beams in the ESM-12B core are then substituted into Equation (4.12) to obtain the power response from 1.3164 to ~1.4351 RIU (Zone I response), corresponding to n_b (= 1.4351) at θ_b = 83.638°. However, when n_{sm} increases beyond 1.4351 RIU or equivalently $\theta_{csm} > \theta_b$, the model in Equation (4.13) is used instead (i.e. Zone II response). The simulation results are then compared with the experimental measurements in Figure 4.11 for a 5-cm long ESM-12B.

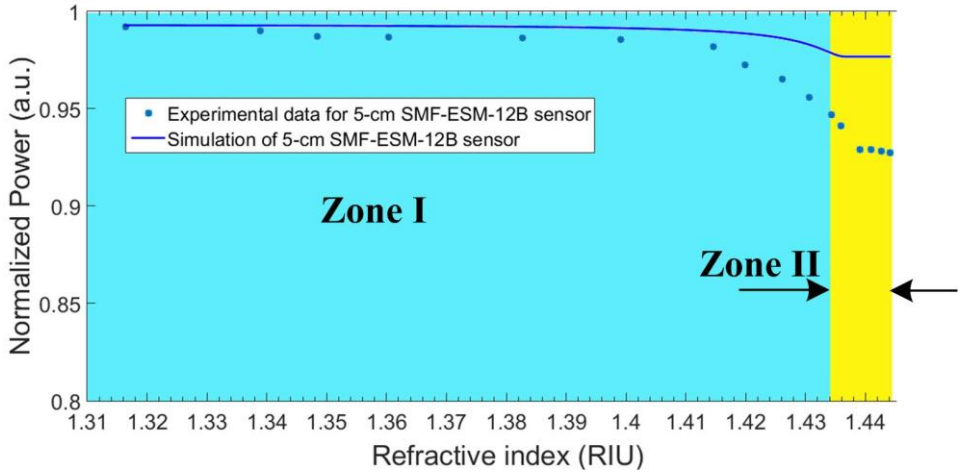

Figure 4.11. Simulated (blue line) and experimentally-measured (blue dots) power responses of SMF fusion-spliced to 5-cm long ESM-12B.

The simulated response for an SMF fusion-spliced to an ESM-12B has a theoretical maximum coupling loss of ~2.32% in terms of optical power, as illustrated by the continuous blue line in Figure 4.11, for which $n_{sm} \cong n_{SiO2}$ = 1.444. This corresponds to a combination of refracted rays from θ_b = 83.64° to θ_{PCF} = 84.46° (illustrated by the red shaded area in Figure 4.10), which are transmitted or refracted into the sensing medium since they are no longer guided or supported by TIR. The flat

responses in both the simulation and the experimental results illustrate the remaining beam guided in the ESM-12B core (unshaded area in Figure 4.10) which is not affected by RI variations in the sensing medium.

The experimental results also show comparatively more losses occurring when $n_{sm} \cong n_{SiO2}$. This discrepancy between simulation and experiment occurs since the splicing process potentially deforms the PC lattice (see Figure 4.8). This thus induces a reduction of the air-hole diameter d, thereby increasing the pitch distance Λ at the SMF-ESM-12B interface (see Figure 4.3(a)). Increasing Λ leads to an increase in MFD_{PCF} as explained by Ju *et al.* [133]. This relationship is plotted in Figure 4.12. NA_{PCF} is subsequently reduced, thereby inducing a decrease in β_{PCF}, consequently reducing the optical power guided along the PCF core.

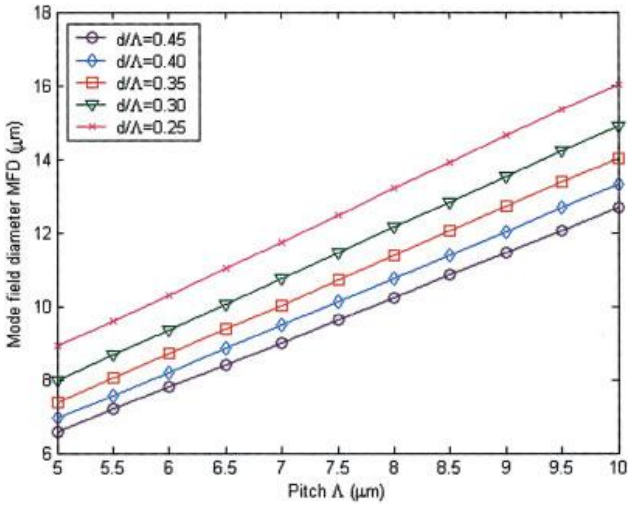

Figure 4.12. MFD_{PCF} in relation with Λ [133].

From the experimental results above, a maximum power loss of ~8.72% occurs when $n_{sm} \cong 1.444$. This is equivalent to the combined ray power from $\theta_b \cong 83.64°$ to the adapted $\theta_{PCF}' \cong 85.54°$, illustrated by the green shaded area in Figure 4.13, which physically explains the modification of $\theta_{PCF} = 84.46°$ into the adapted $\theta_{PCF}' \cong 85.54°$. These refracted rays (from $\theta_b = 83.64°$ to $\theta_{PCF}' \cong 85.54°$) then reach the sensing medium-ESM-12B interface, from where they are subject to optical power losses estimated by the models in Equations (4.12) and (4.13). On other hand, the remaining beam within the boundary of the PCF's acceptance angle (unshaded area in Figure 4.13) is guided in the ESM-12B core.

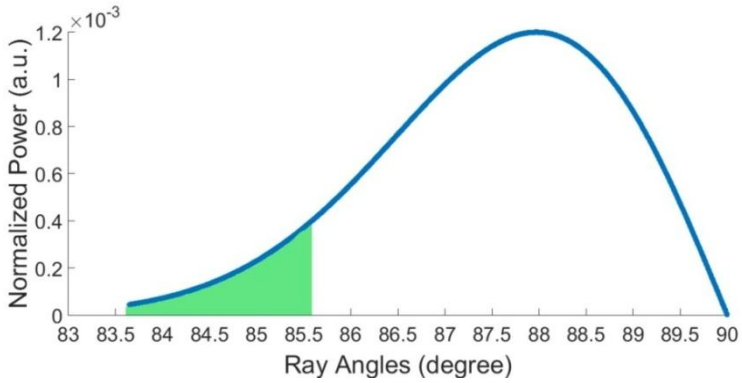

Figure 4.13. Angular power distribution density using adapted refracted rays based on experimental loss measurement for 5-cm long ESM-12B.

It is thus by considering both the refracted and core-guided ray contributions according to the models in Equations (4.12) and (4.13) that the simulated power response can be more accurately estimated. This is validated experimentally as illustrated by the continuous simulated red line in Figure 4.14(a) plotted against the "*"-dotted measured data.

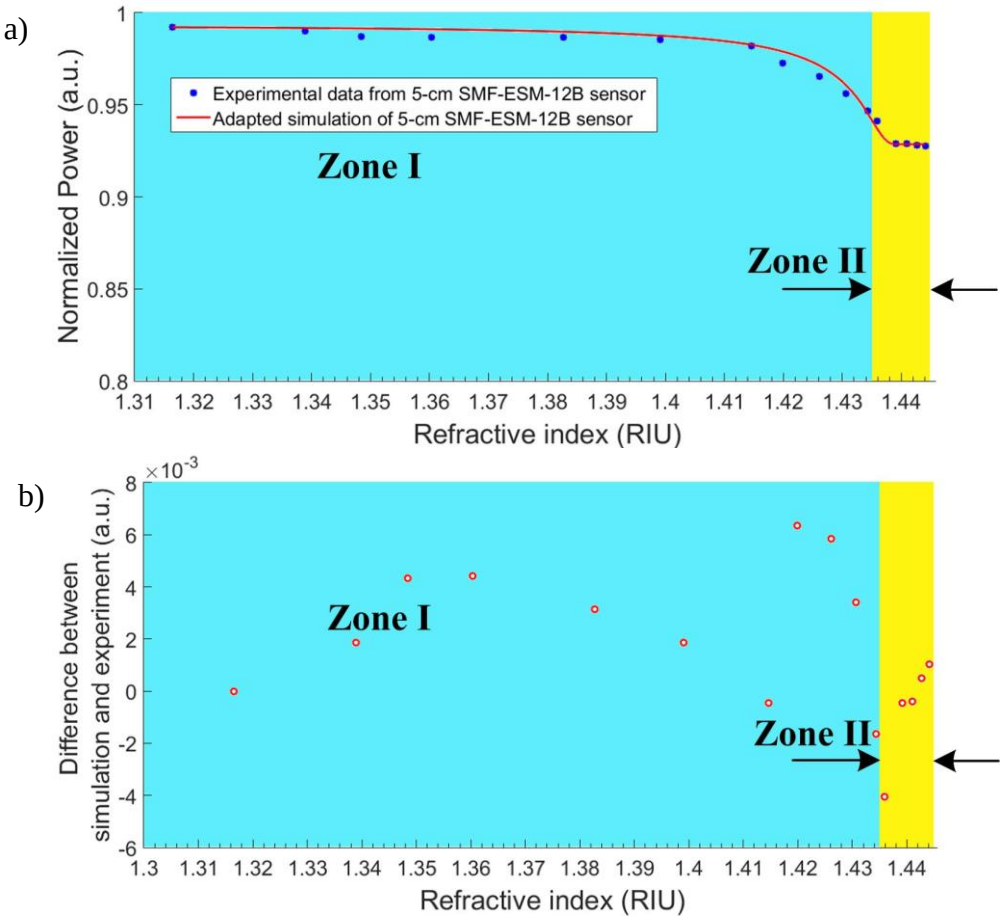

Figure 4.14. a) Experimental and adapted simulation responses based on measured power loss for n_{sm} variation up to ≅ 1.444, and b) difference between both responses.

The simulation results exhibit a relatively high agreement with the experimental data when the adapted angular power distribution density in Figure 4.13 is employed in the power response models. Here, the flat response previously observed for n_{sm} up to ~1.4391 RIU and again for $n_{sm} \sim n_{SiO2}$ (~1.439 RIU) and beyond is still present in both experiment and simulation. This characteristic is a consequence of the contribution from the remaining ray power guided in the ESM-12B core which does not reach the sensing medium and from the refracted rays which are rejected out towards the sensing medium. Nevertheless, the experimental data and the simulated curve for the given condition are now a much better fit when compared to previous results in Figure 4.11. Their difference is plotted in Figure 4.14(b) for which a maximum deviation of only 0.0063 a.u. or 0.63 % has been achieved. Hence, the simulation results in Figure 4.14 clearly show that the proposed experimental-based approach can accurately predict the loss mechanism for an SMF-ESM-12B splice, as a consequence of the fusion splicing process which can potentially modify the air-hole PC dimensions.

Higher splice loss thus occurs when a collapse of the air-holes intervenes over a short length of the ESM-12B. This is illustrated in Figure 4.15 for another end-side ESM-12B spliced to a larger-diameter MMF of 200 µm. The collapse occurs since the latter fiber requires more fusion power to achieve a homogenous splice but which, on the other hand, induces a collapse in the PC structure. Consequently, a certain length about the ESM-12B's collapsed region will function similarly to an MMF which can excite modes from the ESM-12 core. These modes will then propagate toward and finally reach the sensing medium, contributing to more losses as in the MMF-based refractometer. Here, the increased power losses are induced by the modes excited from the ESM-12B's collapse region which is assimilated to a short length of MMF of ~125 µm in diameter (similar to the diameter of ESM-12B). This short section thus operates as an equivalent MMF-based refractometer with the characteristics of higher power reduction or losses as a function of n_{sm}.

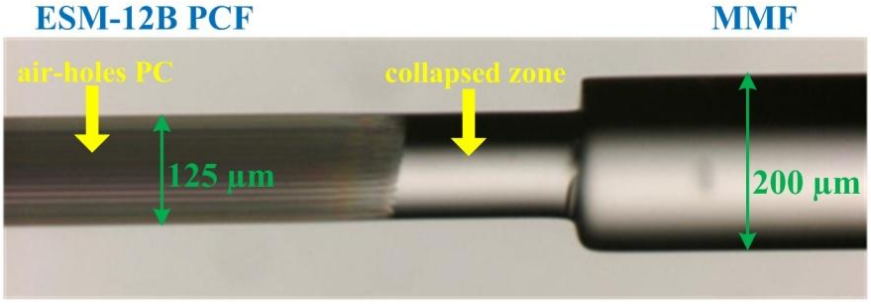

Figure 4.15. Collapse of air-hole structure when one side of ESM-12B is coupled by fusion splicing to an MMF of 200 µm.

However, as illustrated by the experimental results in Figure 4.16, most power is still guided without coming into contact with the sensing medium, despite n_{sm} = 1.444, since the collapse length is relatively short (estimated at ~200 µm). Hence, only a small proportion of the previously guided rays in the ESM-12B core will reach the sensing medium. In addition, the end of Zone II is no longer a flat response, since mode loss still occurs from the excited modes as well as EWA which can occur in the collapsed area which originate from the guided rays in the ESM-12B core.

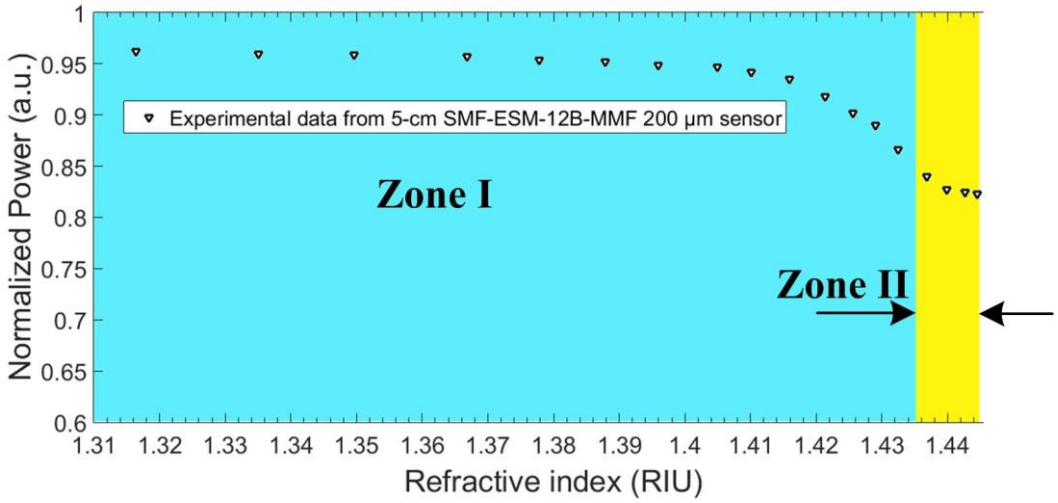

Figure 4.16. Higher losses occurring in experimental power response of SMF-ESM-12B-MMF 200 µm configuration compared to SMF-ESM-12B-MMF 125 µm configuration in Figure 4.14 due to collapse in ESM-12B photonic crystal structure.

According to the above results, propagation in the solid-core PCF can thus be predicted by the step-index fiber propagation principle. This implies replacing the cladding index by n_{FSM} which can be approximated from the effective index of the PC structure as illustrated in Figure 4.2(b). This approach is then employed to analyze the solid-core PCF sensor. More significantly, this sensor is used

advantageously to enhance EWA in Zone I, zone over which the MMF sensor has a very low sensitivity level.

4.3.2. Fusion splicing of SMF-MMF$_1$-LMA-20 PCF-MMF$_2$

An all-fiber hybrid refractometer architecture using an SMF-MMF$_1$-PCF-MMF$_2$ coupling, illustrated in Figure 4.1, to increase EWA in Zone I has been realized. An SMF is first fusion-spliced to MMF$_1$ of 200 µm diameter as shown in Figure 4.17(a). The other end of MMF$_1$ is then spliced to one end of an LMA-20 PCF with a diameter of 230 µm (see Figure 4.17(b)). The other end of LMA-20 PCF is finally spliced to MMF$_2$ with a core diameter of 300 µm (see Figure 4.17(c)) to form a hybrid all-fiber system (c.f. Figure 4.1). The LMA-20 PCF is employed in this work for its diameter compatibility with that of the MMF core diameter (200 µm) thus enabling a comparison of the enhancement level of EWA obtained with this PCF.

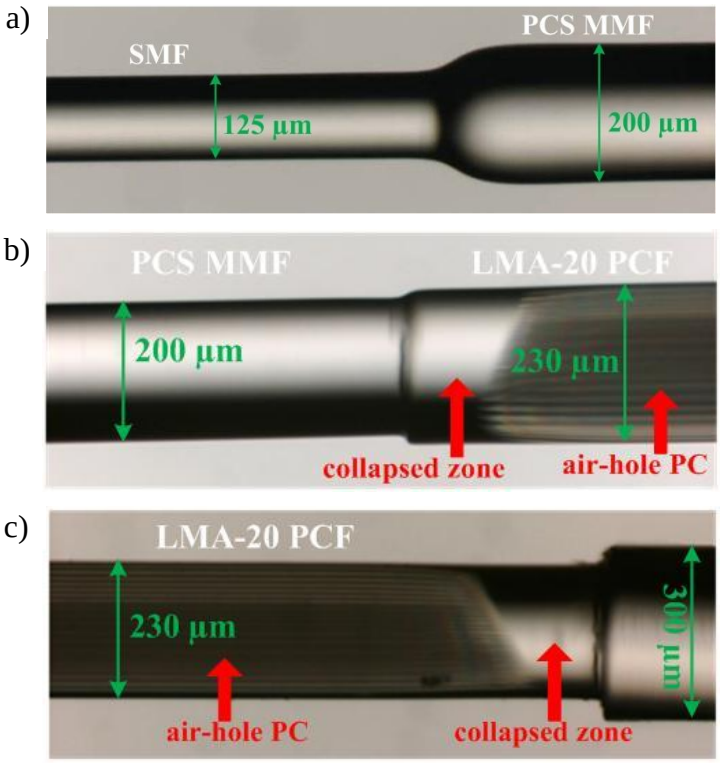

Figure 4.17. Fusion splicing of a) SMF-MMF$_1$, b) MMF$_1$- LMA-20 PCF, c) LMA-20 PCF – MMF$_2$.

The differential scheme employed in Figure 4.9 is next realized to perform experimental characterization of the coupling losses from the all-fiber hybrid set-up.

The same sensing medium as in Section 4.3.1 is also exploited. The MFD_{PCF} of LMA-20 PCF is determined to be ~17.33 µm which corresponds to NA_{PCF} ~0.089. This NA_{PCF} value consequently results in an acceptance angle (β_{PCF}) of 3.55° corresponding to an incident angle θ_{PCF} of ~86.45°. Therefore, part of the beam with incident angles $\theta_i < 86.45$ (θ_{PCF}), illustrated by the green shaded area in Figure 4.18, will be refracted into the cladding. The refracted beam will then reach the PCF outer cladding-sensing medium interface as well as propagate along the PCF subject to EWA, represented by the green shaded area in Figure 4.18 and by the blue ray in Figure 4.1. The unshaded area, on the other hand, represents part of the beam with incident angles $\theta_i > \theta_{PCF.}$

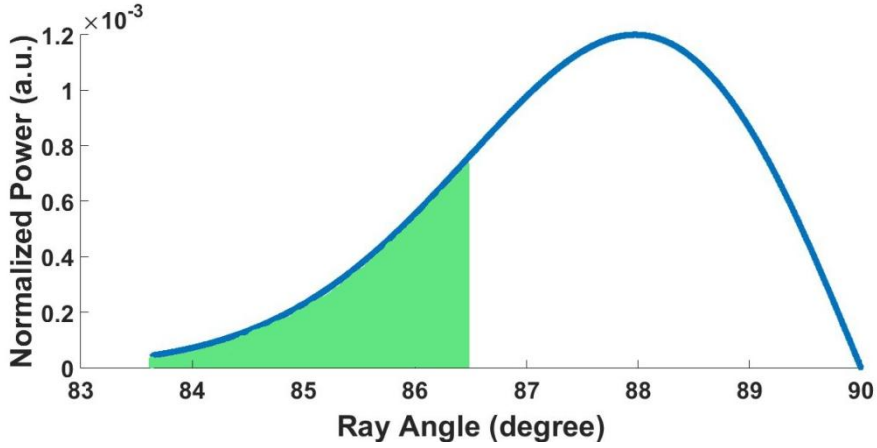

Figure 4.18. Input ray power density distribution $P_0(\theta_i)$ as a function of incident angles from θ to 90°. Green shaded area represents portion of refracted beam .

The simulation and experimental results of the LMA-20 PCF sensor are plotted in Figure 4.19 for a sensing length of 5 cm. As clearly demonstrated, a small discrepancy is observed between simulation and experimental results with a maximum deviation of 0.106 a.u. or 10.6 % (Figure 4.19(b)). This discrepancy could result from the splicing process during the MMF-LMA-20 PCF coupling, leading to a collapse in the air-hole PC structure at the splice interface, as illustrated by Figures 4.17(b) and 4.17(c). Such a collapse could consequently diffract the beam which is injected into the LMA-20 PCF core, and, hence, induce a higher power loss from the core. This has been experimentally analyzed previously such that when n_{sm} ~1.444, the normalized measured optical power is almost 0 a.u., while simulation still results in a normalized power of ~0.092 a.u. In addition, this phenomenon would

subsequently reduce θ_b or equivalently increase β_b from the lead-in MMF, and consequently could displace the boundary between Zone I and Zone II toward the lower RI region. Furthermore, the deformation occurring in the air-hole PC structure at the splicing point can reduce MFD_{PCF}. This, in turn, leads to a decrease in β_{PCF}, as demonstrated in Section 4.3.1, where a relatively high agreement has been achieved by exploiting the adapted simulation results (Figure 4.14) with respect to the original simulation results in Figure 4.11 for an SMF coupled to an ESM-12 PCF. This would simultaneously induce a sharper power response in Zone I experimentally, as is illustrated in both Figure 4.19 and Figure 4.11 since more power should be refracted.

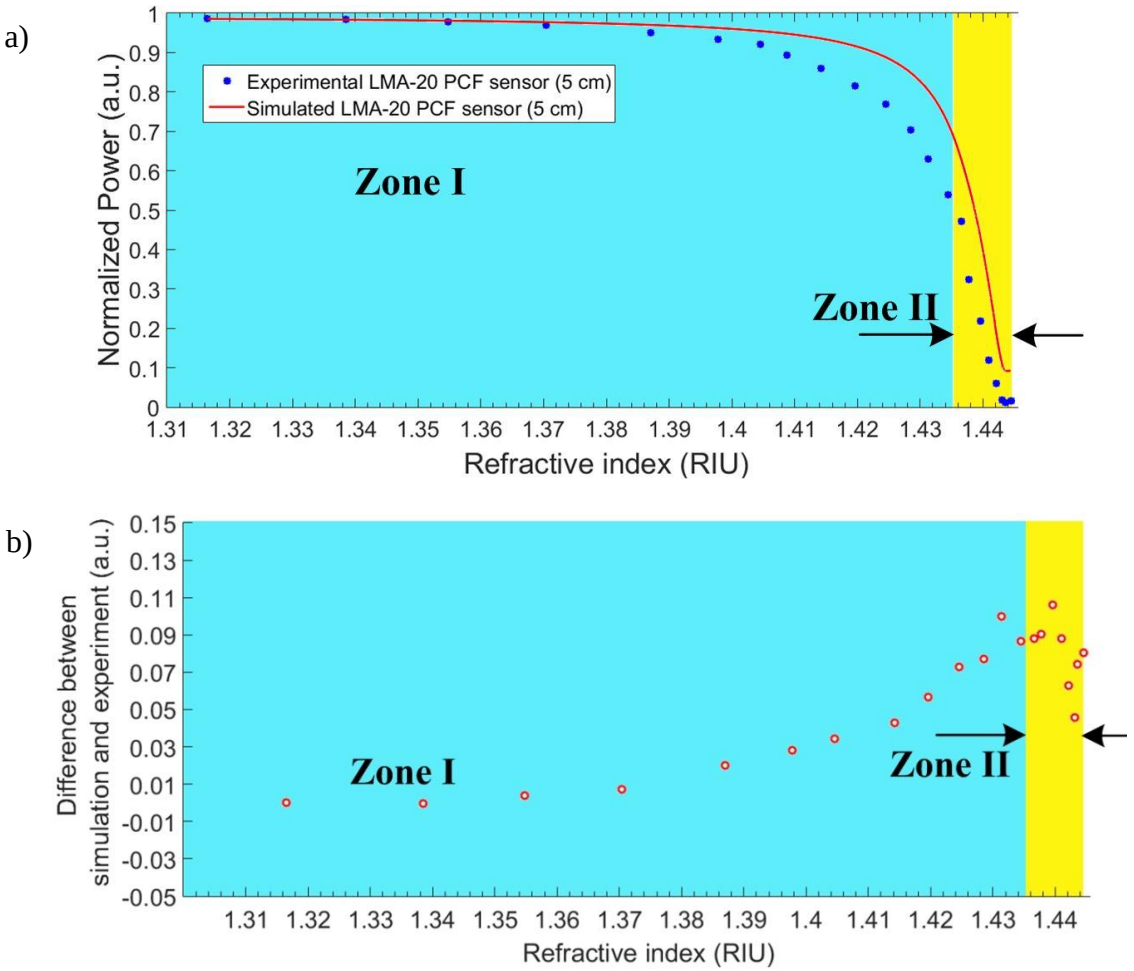

Figure 4.19. a) Power response of LMA-20 PCF sensor with variations of n_{sm}, and b) difference in response between simulation and experimental results for LMA-20 PCF sensor, with a maximum difference of 10.6%.

To further validate EWA enhancement along a solid-core PCF, the power response from a 200-µm core PCS MMF sensor is compared to that from the similar-diameter

LMA-20 PCF sensor (~230 µm) over a similar sensing length of 5 ± 0.1 cm. Higher EWA can even be obtained by employing smaller-diameter PCFs, for example by using the ESM-12B PCF with a diameter of 125 µm and the same sensing length of 5 ± 0.1 cm. The power responses for these 3 sensors are subsequently plotted in Figure 4.20 for comparison.

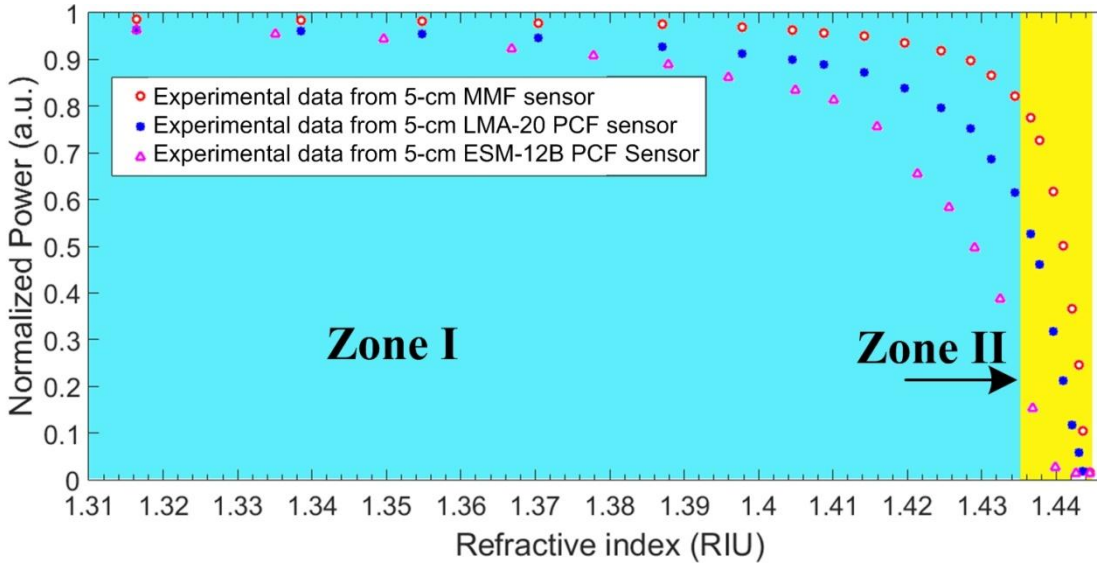

Figure 4.20. Power response of MMF sensor ('o'), LMA-20 PCF sensor ('*') and ESM-12B PCF sensor ('Δ').

Under typical conditions (c.f. conventional step-index MMF), a larger-diameter MMF will exhibit smaller EWA as well as a lower sensitivity. Nevertheless, the results in Figure 4.20 experimentally demonstrate a higher overall sensitivity level for the larger-diameter LMA-20 PCF sensor than for the MMF sensor (230 µm vs 200 µm) in Zone I (uniquely EWA mechanism). This is indicated by a sharper decrease in the response of the LMA-20 PCF sensor. Hence, the PCF can be exploited in refractometric-type sensing to improve the sensitivity at the beginning of Zone I despite having a larger diameter (by 30 µm). The increased EWA in the solid-core PCF-based sensor results from the modes which are propagated within the PCF's outer cladding which has smaller thickness. Hence, more evanescent waves can be absorbed, as described by Figure 4.1 as well as by Equation (4.3).

Further, the power response at the beginning of Zone I of the ESM-12B PCF sensor decreases more sharply than that of the LMA-20 PCF device as well as the MMF sensor, thus inherently resulting in a higher sensitivity for the first sensor. The higher

losses in ESM-12B PCF occur since its relatively smaller diameter leads to higher absorption of the induced evanescent waves. Figure 4.21 subsequently compares the sensitivity level between the 200-µm MMF, LMA-20 PCF and ESM-12B PCF refractometers over a 5 ± 0.1 cm sensing length.

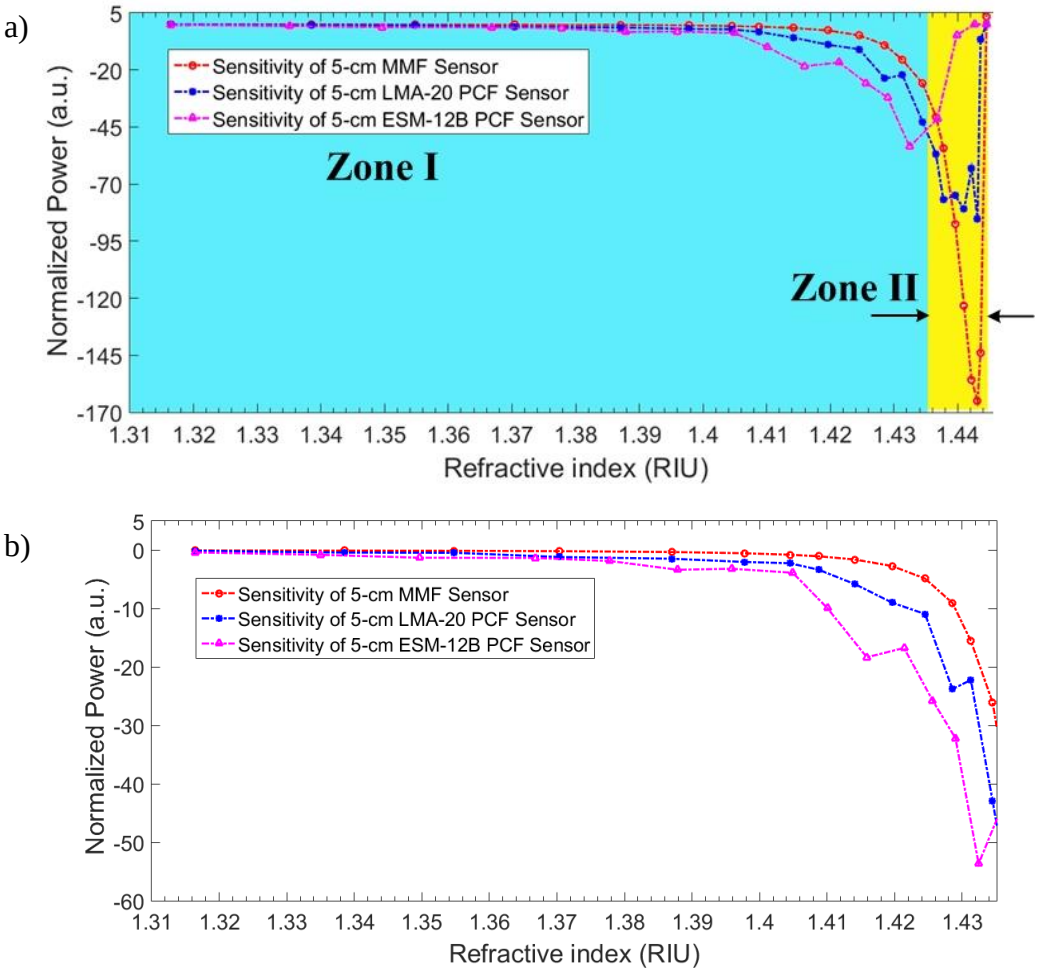

Figure 4.21. Sensitivity level comparison between 200-µm MMF , LMA-20 PCF, and ESM-12B PCF sensors. a) Sensitivity in Zone I and Zone II, and b) sensitivity only in Zone I for uniquely EWA-induced response.

As illustrated, PCF-based sensors have a better sensitivity in Zone I for which only EWA contributes to the sensor performance. In particular, the ESM-12B device has the highest sensitivity due to the strongest EWA since the fiber has a thinner outer diameter. Hence, the highest number of reflections and highest EWA are achieved by this sensor. A sensitivity -0.37 a.u./RIU is initially achieved at the beginning of Zone I by the ESM-12B PCF sensor, while the best sensitivity of -53.67 a.u./RIU is achieved at the end of Zone I. In the case of the LMA-20 PCF, despite its larger diameter compared to the 200 µm MMF, this PCF has a relatively better sensitivity

in Zone I of -0.085 a.u./RIU at the beginning of Zone I, compared to -0.039 a.u./RIU achieved by the MMF sensor. The sensitivity in Zone I increases exponentially with increasing the RI values, with -42.89 a.u./RIU and -28.5 a.u./RIU achieved by the LMA-20 PCF and MMF, respectively, toward the end of this zone. A higher sensitivity is achieved by the LMA-20 PCF sensor since it allows to guide the light within the outer cladding with a thinner thickness of ~45 µm compared to the 100 µm MMF core radius. This thin cladding layer can consequently thus absorb more evanescent waves due to a higher number of reflections. In Zone II, on the other hand, the highest sensitivity of -165 a.u./RIU is achieved by the 200-µm MMF due to the contribution from mode losses which are more dominant than EWA. This thus results in the sharpest decrease in its Zone II response with respect to the other 2 PCF-based sensors, for which sensitivities of -41 a.u./RIU and -85 a.u./RIU are achieved by the ESM-12B PCF and the LMA-20 PCF sensors, respectively.

Furthermore, based on the sensitivity results in Figure 4.21, the ESM-12B PCF and LMA-20 PCF resolutions can be estimated by considering 6 times the rms noise level. At the beginning of Zone I, a resolution of 1.97×10^{-3} RIU and 6.65×10^{-3} RIU are achieved by the ESM-12B and LMA-20 PCFs, respectively. The best resolutions are respectively 1.43×10^{-5} RIU and 1.41×10^{-5} RIU, achieved at the end of this zone. Improvement in resolution in Zone I is clearly achieved by the all-fiber hybrid SMF-MMF_1-PCF-MMF_2 sensors compared to the hybrid SMF-MMF sensor, where a resolution of only 1.64×10^{-2} RIU has been obtained at the beginning of Zone I, while the resolution at the end of Zone I increases to 2.66×10^{-5} RIU. Table 4.2 summarizes the performance of the hybrid SMF-MMF refractometer and hybrid refractometer based on LMA-20, ESM-12B PCFs for 5 cm of sensing length.

Table 4.2. Performance comparison between hybrid SMF-MMF and PCF refractometers.

	Hybrid SMF-MMF refractometer (5 cm)	**Hybrid refractometer based on LMA-20 PCF (5 cm)**	**Hybrid refractometer based on ESM12B PCF (5 cm)**
	Beginning of Zone I	**Beginning of Zone I**	**Beginning of Zone I**
Dynamic range (RIU)	1.316 -1.4351	1.316 -1. 4351	1.316 -1. 4351
Highest resolution (mRIU)	16.4	6.65	1.97

4.4. Conclusions

In Chapter III, a very high sensitivity in Zone II has been achieved by the all-fiber SMF-MMF refractometer. This device also has the highest sensitivity in Zone III. However, its sensitivity in Zone I, particularly at the beginning of Zone I, is very low due to a lower number of reflections. This is a consequence of the incident angle from the lead-in SMF being closer to 90°.

To improve the sensitivity in Zone I in which only EWA influences the sensing performance, the number of reflections along the sensing area must be increased. Increasing these reflections in an all-fiber refractometer has been realized by employing solid-core PCFs as the sensing element in a hybrid SMF-MMF_1-PCF-MMF_2 architecture. This enables propagation of the lightwaves within the outer silica cladding by rejecting the normally-core modes toward the outer area of the PCF. In this way, EWA can be significantly increased due to the thinner thickness of the outer cladding layer.

The models to estimate the power response of the PCF-based sensors have been developed and corroborated experimentally with relatively good agreement. Furthermore, for the same sensing length, the results show that a better sensitivity of up to 2 times (-0.085 a.u./RIU) has been achieved at the beginning of Zone I by the LMA-20 PCF-based sensor, while more than 8 times improvement of the sensitivity (-0.37 a.u./RIU) has been achieved by the ESM-12B PCF sensor in comparison with the MMF device (-0.039 a.u./RIU). A higher sensitivity at the end of Zone I is also achieved by both PCF-based sensors (-53.67 a.u./RIU and -42.89 a.u./RIU for the ESM-12B and the LMA-20 PCFs, respectively).

CHAPTER V

Application of Fiber Optic-based Refractometer in Methane Detection: Preliminary results

5.1. Introduction

One potential application of the fiber refractometer is in the detection of the methane (CH_4) gas whereby the sensing element can be functionalized to CH_4 by exploiting supramolecules of cryptophane-A. Cryptophane-A, which has a molecular structure illustrated in Figure 5.1, was first discovered by Gabard and Collet in 1981 [134]. It can entrap CH_4 gas effectively since the lipophilic internal cavity volume of cryptophane-A (~81.5 $Å^3$) is sufficiently spacious to incorporate the CH_4 molecule with an internal volume of ~28.4 $Å^3$ [135]. In addition, cryptophane-A has a relatively strong affinity towards CH_4, with a binding constant of 130 M^{-1} at 295 K. Hence, CH_4 molecules which penetrate within cryptophane-A can be efficiently entrapped.

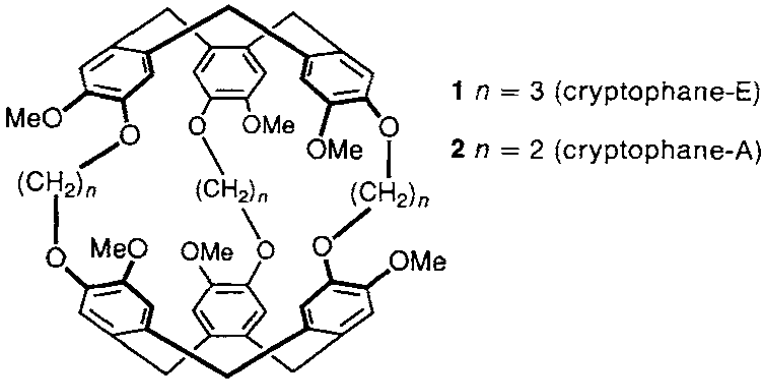

Figure 5.1. Molecular structure of cryptophane [135].

As widely reported in the literature [15, 86, 136-138], cryptophane-A, when incorporated into an organic transparent polymer host, can trap and then bind the CH_4 molecule by a weak Van Der Waals force. In addition, CH_4 molecules can also be reversibly released from cryptophane-A based on thermodynamic chemistry equilibrium [139]. This interaction leads to a variation of the host polymer's bulk refractive index (RI) which is then proportional to the CH_4 concentration. For

example, using polydimethylsiloxane (PDMS) as the host polymer and an LED as the light source operating at a wavelength of 830 nm in a surface plasmon resonance (SPR)-based sensor, Boulart *et al*. [86] reported the variation of RI as a function of dissolved CH_4 concentration in an aqueous environment. They reportedly obtained a linear response from their device, with a sensitivity of 5.5×10^{-6} RIU/nM CH_4, as shown in Figure 5.2. The initial index of the PDMS without CH_4 is ~1.4120. This implies that to measure CH_4 concentration of 1 nM order, a refractometer with a resolution of at least 5.5×10^{-6} RIU is required.

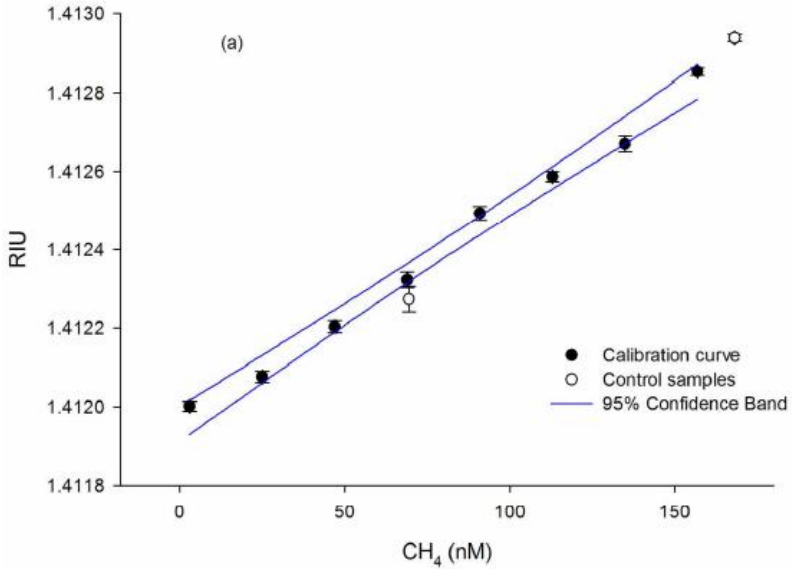

Figure 5.2. Measurement results of RI variation versus methane concentration in aqueous environment [86].

Methane sensors continue to attract intense interest and development since it is one of the most important greenhouse gases. Although second only to carbon dioxide (CO_2) in terms of emission, CH_4 strongly absorbs in the infrared and has a global warming potential 25 times stronger than that of CO_2 [140, 141]. This obviously makes CH_4 one of most significant greenhouse gases alongside CO_2, N_2O (nitrous oxide) and fluorinated gases which increasingly contribute to the global warming effect. As reported by the United States Environmental Protection Agency, CH_4 emission is estimated at 10%, rendering it the second greenhouse gas in the USA in 2016 [142]. Figure 5.3 shows a chart of greenhouse gas emission from the four most important gases in the USA [142]. An even higher global greenhouse gas contribution from CH_4 is, however, estimated at between 15-20% [140].

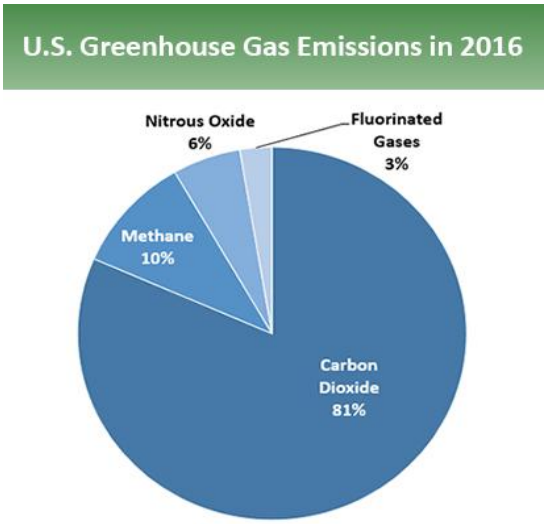

Figure 5.3. Percentage of emitted greenhouse gases in the USA in 2016 [142].

Methane is produced and released from both anthropogenic and natural sources. Naturally, CH_4 can be produced from biological degradation of organic matters by anaerobic microbes as a result of the methanogenesis process [143]. These organic matters can originate from, for example, detached or fallen leaves, as well as from human activities such as agricultural waste, household waste and wastewater. Furthermore, CH_4 can also be released into the atmosphere from leakages during natural gas production, gas and oil drilling, and coal mining [144]. Hence, continuously-growing human population and the associated energy-dependent activities would contribute an increasing CH_4 concentration in the atmosphere as forecast in Figure 5.4.

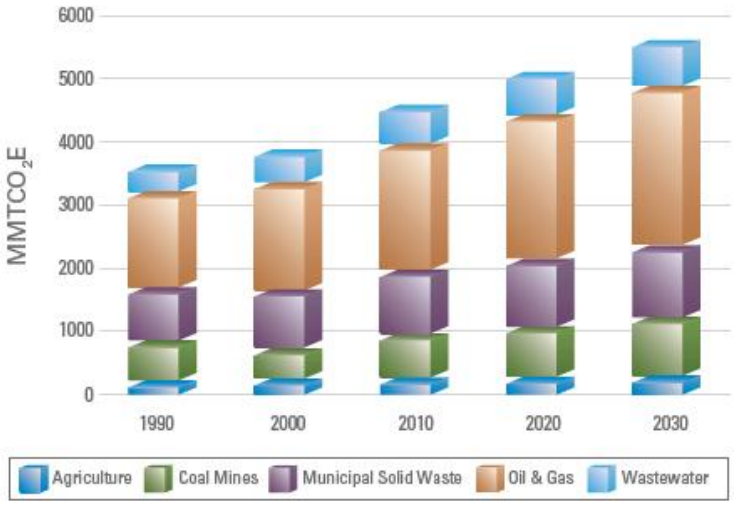

Figure 5.4. Global anthropogenic methane emission from 1990 to 2030 [144].

One consequence will evidently be the rise in temperature in both the atmosphere as well as the ocean. The subsequent increase in the ocean's temperature will potentially induce large amounts of CH_4 being released from the ocean floor as well as from the Artic, since CH_4 is stored as clathrates in the deep-sea floor and the Artic. Moreover, this warming will degrade the permafrost layer in the Artic as well as in other high-latitude regions, which contain vast quantities of trapped CH_4, potentially releasing it to the atmosphere [145].

With CH_4 playing such a critical role in the global warming effect, an intensive global monitoring and study effort thus needs to be implemented to observe the evolution of its concentration both in the atmosphere as well as from aquatic sources. To support this objective, various kinds of CH_4 sensors, such as the solid state-based sensor [146-148], calorimetric-based sensor [149, 150], and photoacoustic-based sensor [151], have been developed by researchers. Although these sensors are relatively low-cost and can be used for long-term measurement, most are, however, also often sensitive to other kinds of gases. In addition, since most, if not all, of these sensors require electrical supply, they consequently cannot be easily deployed for *in situ* monitoring in the natural environment.

The optical fiber sensor is one alternative solution which can be employed for long term *in situ* measurement involving no risk of explosion or short circuit since no on-probe electrical supply is necessary. Various optical fiber-based CH_4 sensors have been studied, such as the surface plasmon resonance (SPR) sensor [86, 152], the waveguide Mach-Zehnder interferometer [138], and the evanescent wave multimode fiber (MMF) sensor [15]. These sensors exploit cryptophane-A supramolecules incorporated into an organic transparent polymer of PDMS or styrene acrylonitrile (SAN) which selectively trap and bind CH_4 molecules. SPR sensors operate principally on spectral modulation and typically require an optical spectrum analyzer (OSA) or an optical time domain reflectometer (OTDR) both of which are relatively costly and fragile to operate. The Mach-Zehnder interferometer employs relative phase measurement, thus requiring relatively complex interrogation schemes and set-ups. The MMF evanescent wave sensor based on intensity modulation, on the other hand, while relatively simple and cost-effective to realize, has been reported to

potentially offer very good resolution and sensitivity [15, 153]. This chapter will thus describe development effort on intensity-based MMF sensors for methane gas detection through functionalized polymeric thin films encapsulating cryptophane-A supramolecular traps.

5.2. Sensor fabrication

As described in previous chapters, the MMF sensor can be realized by stripping a certain length of its cladding and buffer or coating, as shown in Figure 5.5. For a differential sensor configuration, the sensing fiber consists of one stripped-cladding length that is coated with a thin film of host polymer of either PDMS or SAN with cryptophane-A incorporated into its bulk volume while the reference fiber employs an identical stripped fiber length coated uniquely with the host PDMS or SAN polymer without any cryptophane-A.

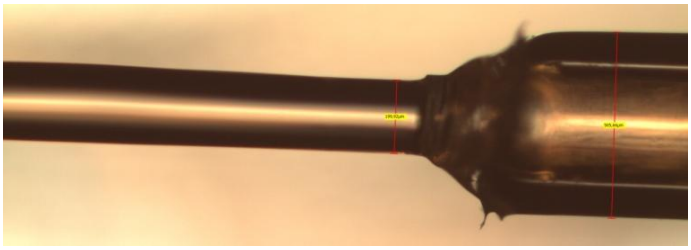

Figure 5.5. Stripped-cladding silica fiber as the sensing region.

During initial trials, PDMS is used as the host polymer incorporating cryptophane-A as the sensing layer which covers a length of 2 ± 0.1 cm of the MMF core. Here, 10 mg of cryptophane-A is first dissolved in 2 ml of tetrahydrofuran (THF) which is used as the solvent. The PDMS polymer host is prepared by mixing 1 ml of siloprene (K1000) with 0.1 ml of cross-linking agent (K11) for ~10 minutes. This PDMS solution is then mixed with the dissolved cryptophane-A and deposited onto the MMF core. To obtain a uniform sensing film layer, control the layer thickness as well as ensure the repeatability of the process, the coated MMF is placed and secured on a silicon wafer using adhesive paper, then mounted onto a spin-coater which was subsequently turned at 3000 rpm for 1 minute. This coated fiber is next cured in an oven at 100 °C for at least 120 minutes, resulting in a sensitized MMF sensor as illustrated in Figure 5.6.

a)

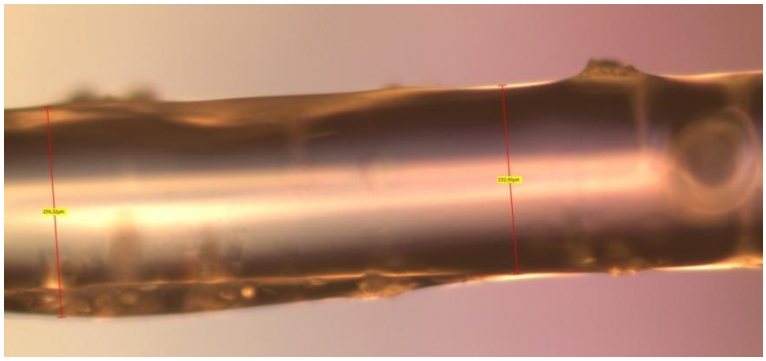

b)

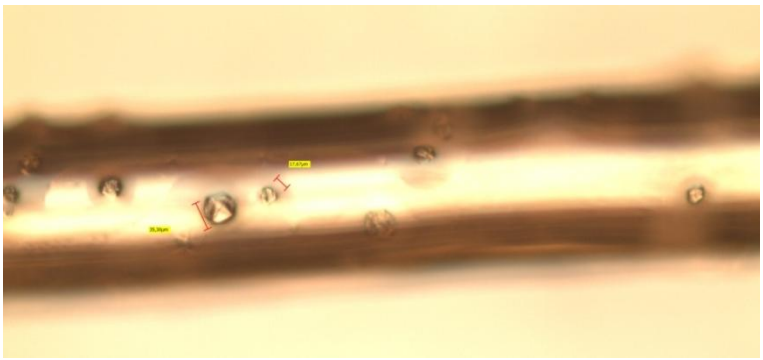

Figure 5.6. Sensitized MMF using host polymer film of PDMS incorporating cryptophane-A supramolecules showing a) non-uniform thickness of sensitive layer, and b) some cryptophane-A precipitates on film surface, implying that molecules were not completely dissolved in THF.

However, the sensitive polymeric film is not uniformly deposited along the bare MMF core as can be observed in Figure 5.6(a), with a measured outer diameter varying from 222 µm to 259 µm. In addition, there is also strong evidence that the cryptophane-A molecules are not perfectly or completely dissolved in the THF solvent. These are observed as residues or precipitates on the surface of the polymer film (see Figure 5.6(b)). One consequence of this problem would be a higher sensor noise floor since these residues could induce unwanted scattering effects at the interface of the MMF core and sensitive layer. More important, to achieve the necessary performance to detect very low concentrations of CH_4, the MMF sensor should be optimized to operate in the Zone II operating regime where sensitivity has been found to be highest (see Chapter III). However, more than 90% of the injected optical power has been transmitted by the sensitized arm of the MMF sensor suggesting that the sensor response is in Zone I as described in previous chapters. This occurs since the bulk RI of the PDMS is ~1.3997 RIU at 1550 nm, indicating an RI response in Zone I, with characteristics similar to that described for the hybrid

SMF-MMF refractometer in Chapter III. This subsequently means that only a relatively low sensitivity to RI variation would be obtained when PDMS is employed in the hybrid SMF-MMF system.

Consequently, in order to improve the refractometer sensitivity, it is necessary to use a host polymer with a higher RI that is situated in the Zone II regime. Another polymer variant, styrene acrylonitrile or SAN [136, 138, 154] with an RI value of 1.5496 RIU at a wavelength of 1052 nm, is also tested for use as another potential polymeric host. To synthesize the sensing film, a carefully-proportioned quantity of the 1,1,2,2,-tetrachloroethane solvent is used to dissolve both cryptophane-A and SAN, as reported in [155]. Here, 10 mg of cryptophane-A in powder form is first dissolved in 2 ml of 1,1,2,2,-tetrachloroethane after which 100 mg of SAN powder are then added. To enable complete solution of SAN as well as ensure a homogenous distribution of the cryptophane-A supramolecules, the mixture is shaken for a minimum of 30 minutes. The solution is then deposited onto a 2 ± 0.1 cm length of bare MMF core and smoothed by passing over an optical fiber stripper with a predetermined hole size of 250 µm in order to obtain a relatively homogenous sensing layer surface. The coated MMF is then heated in an oven to cure at 100 °C for 60 minutes, an example of which is illustrated in Figure 5.7.

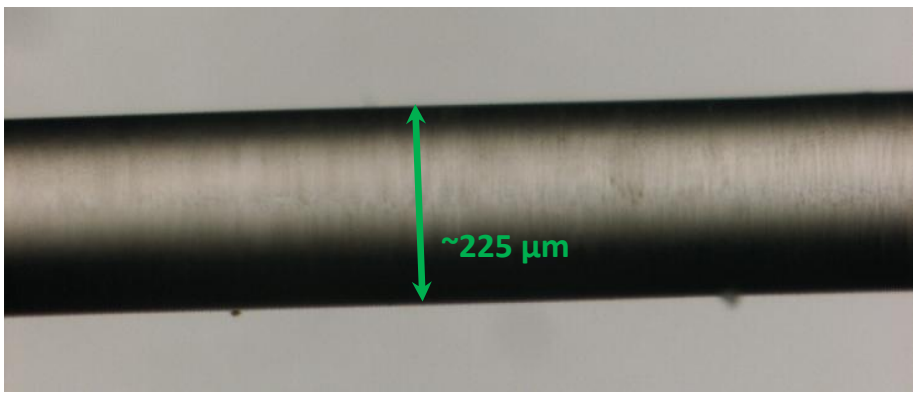

Figure 5.7. Surface smoothness of sensitized MMF coated with SAN plus cryptophane-A polymeric layer after curing in oven.

As clearly shown, the sensing layer is relatively homogenous and does not appear to contain any cryptophane-A residues or precipitates. This is subsequently employed for detecting CH_4 in parallel with an MMF reference arm which has been coated uniquely with SAN but without cryptophane-A. Both fiber arms are then mounted in

a differential configuration in order to compensate common mode noise (e.g. variation in ambient temperature, laser output power, vibration, etc).

5.3. Hybrid SMF-MMF set-up of for CH_4 measurement

The hybrid SMF-MMF-based refractometer to be used in this chapter for CH_4 detection has previously been studied in Chapter III where the best sensitivity has been found to occur in Zone II. Moreover, with the hybrid SMF-MMF system, a better sensitivity in Zone III has also been achieved, compared to the initial MMF refractometer in Chapter II which employed microscope objectives for beam injection. To set the SMF-MMF refractometer up for CH_4 measurement, the sensing region is held straight by a specially-designed support which also serves to avoid unwanted vibration or movement. The lead-in SMFs, being more resistant to bending and mechanical disturbances, are left free to be connected to the appropriate set-up.

A 5L-volume air-tight flask shown in Figures 5.8(a) and 5.8(b), into which the MMF sensing and reference arms are deployed together, is used to contain the CH_4 gas during the experiment. Light from a single-mode laser is equally injected into the pair of lead-in SMFs fusion-spliced to the MMFs (see set-up in Figure 5.8(a)). The outputs from the sensing and reference MMFs are detected by a pair of identical photodetectors which are connected to a 8-channel simultaneous 16-bit National Instrument data acquisition system (NI-DAQ). The experimental data are next transferred to a dedicated PC for processing.

A small flexible tube is used to introduce CH_4 from the top of the flask, while another similar tube at the bottom of the flask enables to drain and reduce the CH_4 concentration in the flask. A commercial MQ-4 CH_4 sensor from Hanwei Electronics has been deployed as the reference sensor for comparison as well as to quantify the CH_4 concentration in air over a dynamic range from 200 ppm to 10000 ppm.

a)

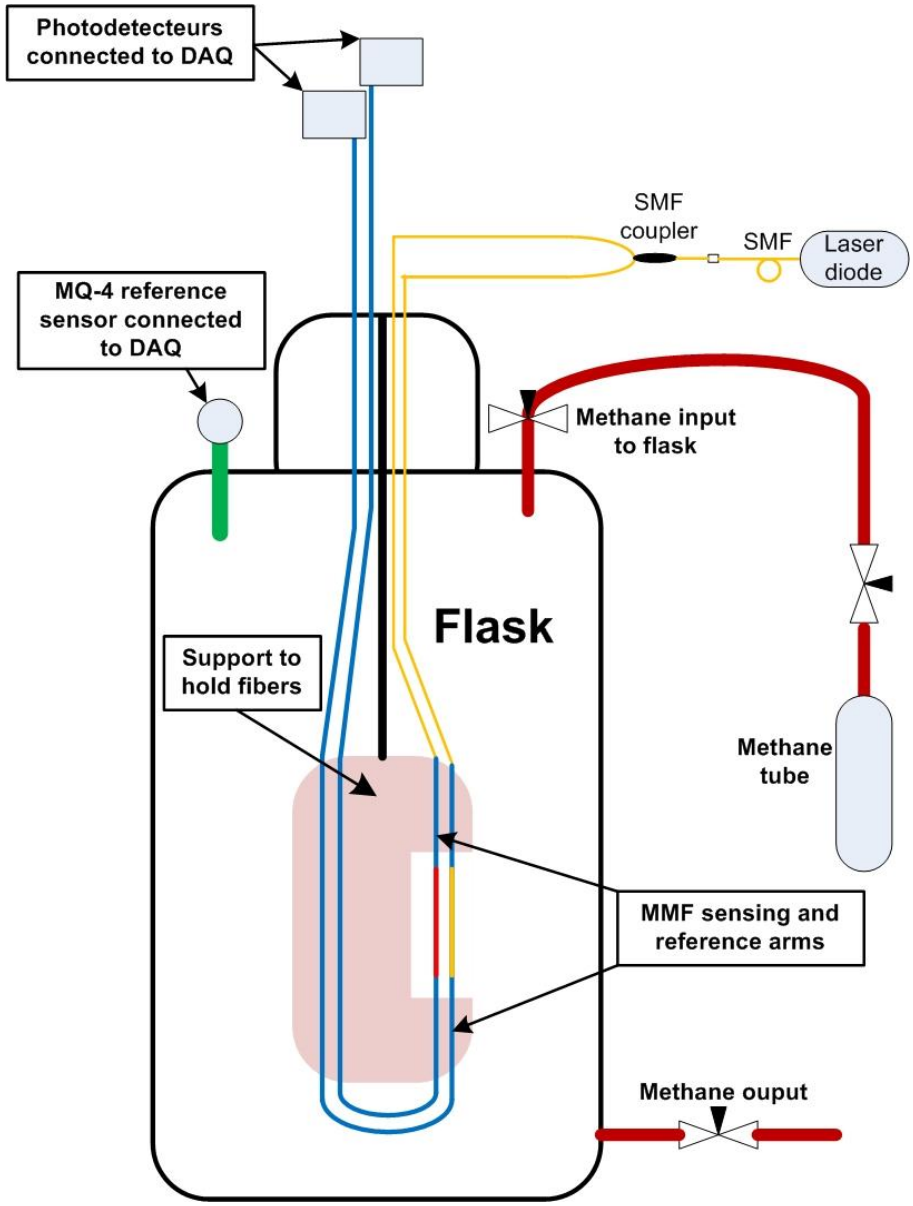
Photodetecteurs connected to DAQ
SMF coupler
SMF
Laser diode
MQ-4 reference sensor connected to DAQ
Methane input to flask
Flask
Support to hold fibers
Methane tube
MMF sensing and reference arms
Methane ouput

b)

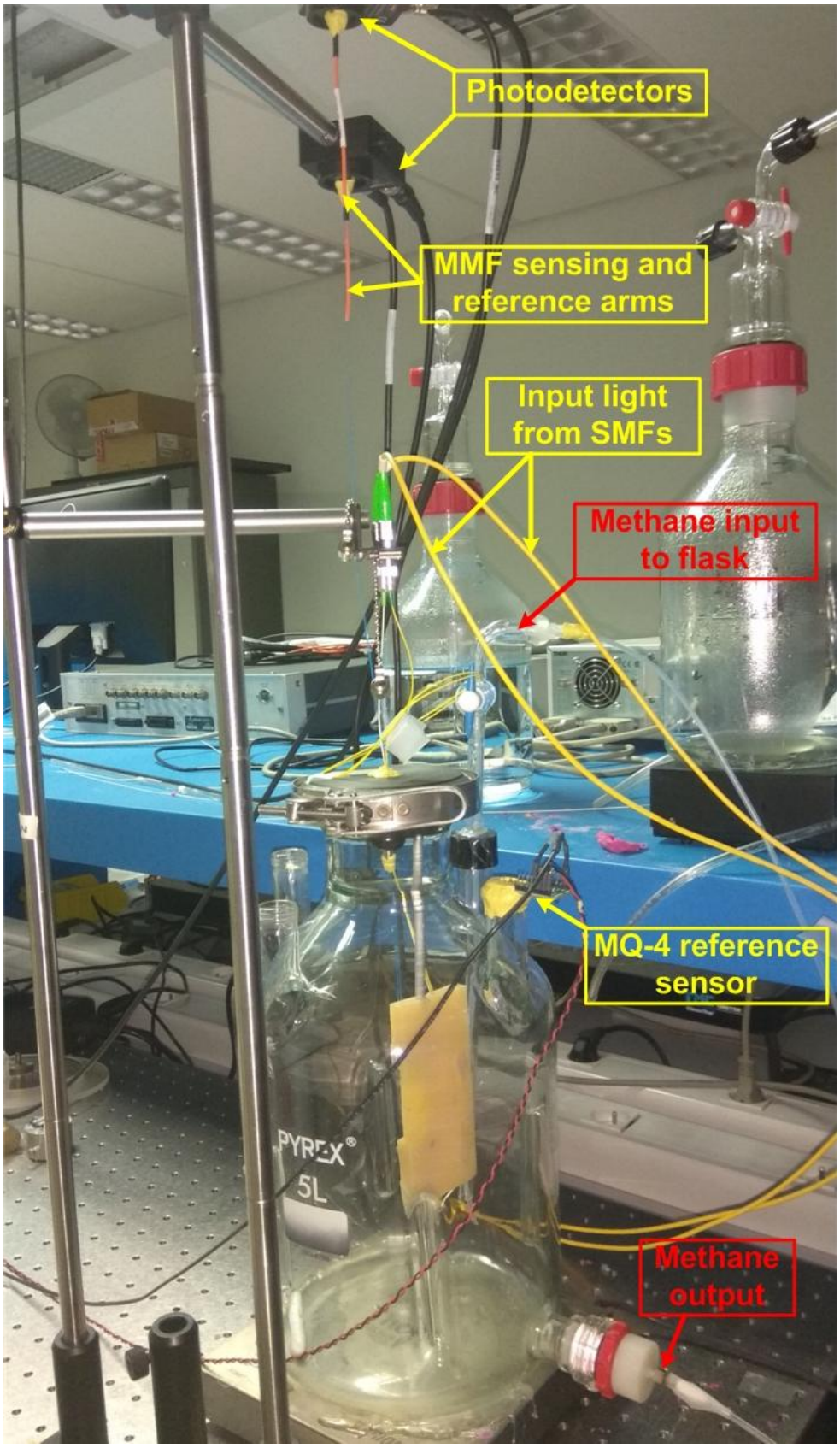

Figure 5.8. Experimental set-up to measure atmospheric and dissolved CH_4 concentration: a) schematic, and b) actual image.

5.4. Results and discussions

To measure atmospheric CH_4 concentration in a controlled volume using the experimental set-up shown in Figure 5.8, the output signals from the sensing and reference MMFs as well as that from the reference MQ-4 sensor are initially recorded in the absence of CH_4. Methane is then progressively introduced into the container by slowly opening a screw valve from the CH_4 input tube. This is subsequently closed when the output from reference MQ-4 sensor is at a maximum voltage, corresponding to a controlled CH_4 concentration of 10000 ppm or 1%. This thus enabling the entire sensor system to be calibrated. This level is maintained for approximately 60 seconds. The CH_4 gas is next drained by opening the small caps of the flask as well as the output valve to observe and record the response of the refractometric sensor during cyclic injection of CH_4. A sample of the measurement results for both increasing and decreasing CH_4 concentration is presented in Figure 5.9.

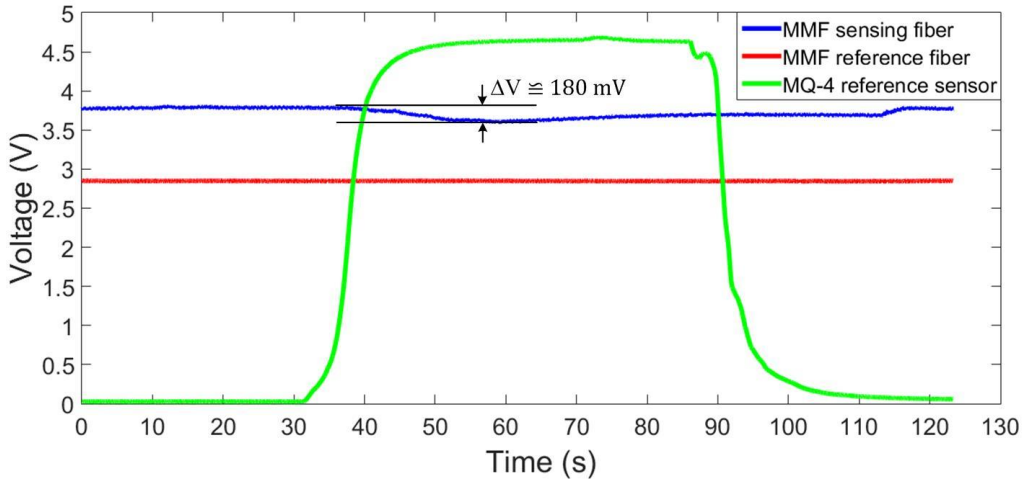

Figure 5.9. Response of SMF-MMF sensor and reference MQ-4 sensor to cyclic injection of 10000 ppm of methane.

The transmitted power of the MMF sensing fiber (blue line) decreases from an initial value of 3.78 V (i.e. without CH_4) to ~3.60 V, equivalent to 0.936 mW and 0.892 mW of optical power, respectively, and is detected by the photodetector set to a 10-dB gain level. These results represent a decrease of ~4.76 % of optical power for 10000 ppm of injected CH_4. The power subsequently increases back to its original value when the flask is drained of CH_4. This transmitted power variation could be

interpreted as the MMF sensor being in the Zone II operating regime of the hybrid SMF-MMF refractometer. In this highly sensitive zone, the optical power will decrease with increasing index (i.e. increasing CH_4 concentration) and vice versa. Further, a difference in the measured signal levels between the sensing MMF (blue line) and the reference MMF (red line) is observed in Figure 5.9. The sensing MMF which has been coated with a thin film of SAN incorporating cryptophane-A is observed to transmit a higher power of ~3.78 V compared to ~2.84 V transmitted by the reference MMF. This difference could be attributed to the dissolved cryptophane-A which could potentially contribute to decreasing the bulk index of the host SAN polymer and, hence, leading to an increase in the transmitted power.

Furthermore, while the sensing MMF responds to the presence of CH_4 as expected (blue line), the reference MMF (red line) remains stable throughout the experiments, thus exhibiting no sensitivity to CH_4. The optical power of the sensing MMF, measured in voltage by the photodetector, decreases when CH_4 is introduced. This clearly indicates an increase in the RI of the host polymer since the sensing MMF is in Zone II which exhibits a sharply decreasing power with increasing index. More important, the response of the sensing MMF to cyclic variations in CH_4 concentration is relatively fast (~25 seconds) compared to [86] which reported a response time of ~1.8 minutes. The MMF refractometer is thus highly suitable for applications where fast response is required, in particular to increase the temporal resolution of the measurements.

In terms of sensitivity, the MMF sensor (sensing arm) is found to exhibit a relatively low response (ΔV) of ~180 mV for 10000 ppm of CH_4 concentration. The reference MQ-4 sensor, on the other hand, is subject to a voltage variation of ~4.65 V. By assuming a linear variation of the polymeric SAN-Cryptophane-A index with CH_4 concentration as demonstrated in Figure 5.2 [86], as well as a linear response approximation in Zone II, the sensitivity (S) of the fiber sensor can then be predicted by

$$S = \left| \frac{\Delta V}{\Delta CH_4} \right| \tag{5.1}$$

where ΔV and ΔCH_4 represent the response of the sensing MMF and the corresponding CH_4 concentration variation, respectively. According to Equation (5.1), we thus obtain a sensitivity of 18µV/ppm (or 180 mV/10000 ppm). Corresponding to this sensitivity value, the limit of detection (LOD) can be estimated by [139, 154, 155]

$$LOD = \frac{2.821}{S}\sigma_{rms} \tag{5.2}$$

where σ_{rms} is the noise level of the sensing MMF which can subsequently be obtained by analyzing the power spectral density (PSD) of the direct output signal (i.e. without any pre-processing) in the frequency domain through the fast Fourier transform (FFT) function in Matlab. The estimated noise level is then presented in Figure 5.10 for a sampling frequency of 1 kHz, for which the measured signal is DC with a bandwidth of 500 Hz. The noise level achieved for the refractometer is currently ~1.187mV_{rms}, corresponding to an LOD of 186 ppm or 0.0186% CH_4 obtained by Equation (5.2) (LOD = 2.821×1.187 mV/18 µV/ppm).

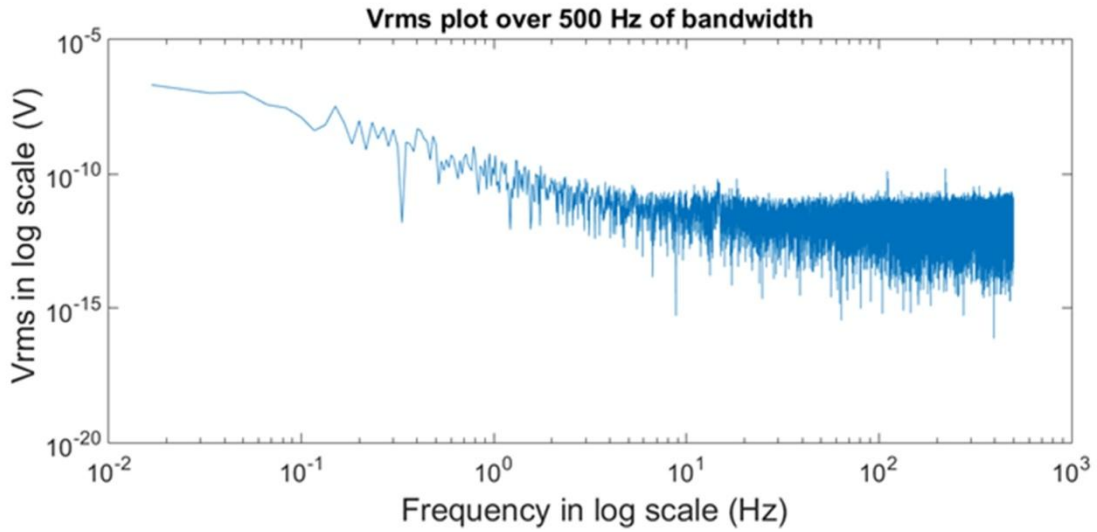

Figure 5.10. Noise signal figure of the MMF sensor in frequency domain at sampling frequency of 1 kHz.

However, this LOD has been improved by filtering the measured signal using a moving average filter (signal smoothing) to further reduce the "white" noise contribution of the system. This consequently results in a noise level of 1.11 mV_{rms} and translates to an equivalent LOD of 174 ppm or 0.0174% of CH_4 concentration in air. The LOD obtained is lower than another CH_4 sensor based on Mach-Zehnder

interferometry (MZI) which has a reported LOD of 17 ppm [138], and is due to a relatively lower sensitivity of our MMF methane sensor. This lower sensitivity could potentially originate from a lower index variation of cryptophane-A sensitized film in response to CH_4 variation. It is, however, to be noted that the MMF refractometer has been configured to operate in the highly-sensitive Zone II regime, which has the capability to easily detect minute RI variations (resolution ~2.7 x 10^{-6} RIU) as demonstrated in Chapter III. The current performance of the MMF refractometer is significantly influenced by the comparatively lower index variation of the sensitized polymer film in the presence of CH_4. This thus calls into question the quality of the cryptophane-A supramolecules which could not efficiently entrap the target CH_4 molecules. To investigate this hypothesis, a new batch of cryptophane-A has been tested by following an identical coating preparation procedure. Compared to the first batch of cryptophane-A, the new batch is found to be even less sensitive with an LOD of 1116 ppm or 0.1116 % CH_4 concentration. Nevertheless, the MMF refractometer exploiting the first batch of cryptophane-A is at least 100 times more sensitive than the evanescent wave absorption (EWA)-based fiber methane sensor using PDMS as the polymeric host, with a reported LOD of 2% [15]. It is also comparatively more sensitive than the 0.2% LOD (i.e. by more than 10 times) from the long-period fiber grating sensor reported in [136] which used SAN as the host polymer.

Nonetheless, the current MMF refractometric CH_4 sensor has been observed to exhibit a repeatability issue. For every first measurement with this sensor, the CH_4 concentration can be detected with a relatively good response. However, the performance (i.e. sensitivity) decreases or is degraded for subsequent measurements or repeated utilizations. Unfortunately, the origin of this repeatability problem has not yet been confirmed, and is still under investigation.

5.5. Conclusions

In initial trials, the sensing layer was fabricated by incorporating cryptophane-A supramolecules into PDMS hosts using THF as the solvent to dissolve cryptophane-A. However, it is found that THF apparently cannot efficiently dissolve the

supramolecules. As such white precipitates or residues of cryptophane-A have been observed to be suspended within the PDMS host substrate under the microscope. These residues could induce undesired scattering at the interface of the MMF core and the sensing layer, potentially contributing to a higher sensor noise floor. In addition, it has also been observed that the PDMS film was not uniformly distributed throughout the circular MMF core, which could affect the sensor's reproducibility in terms of performance as well as response time.

To overcome those problems, another polymer variant based on SAN (or styrene acrylonitrile) is employed. Here, 1,1,2,2,-tetrachloroethane has been used as the solvent to completely dissolve the cryptophane-A supramolecules, with no residues being observed under the microscope. The use of SAN as the polymeric host also enables a relatively uniform sensitized layer or film to be deposited on the fiber surface, contrary to the PDMS-based layer.

More important, the experimental work performed to characterize the sensor for CH_4 measurement has demonstrated a relatively fast response (~25 seconds) achieved by the sensitized or functionalized MMF refractometer. Nevertheless, a detection limit of only ~174 ppm or 0.0174 % has currently been obtained. This is 10 times inferior to that of the MZI-based CH_4 sensor where an LOD of 17 ppm has been reported. This result is, however, comparatively better than both the EWA-based CH_4 fiber sensor and the long-period grating sensor which had detection limits of 2 % [15] and 0.2 % [136], respectively. Last, but not least, the repeatability issue observed in the MMF refractometric methane sensor must be further investigated and solved before the full capability of the sensor can be characterized for real-world applications in the natural environment.

Conclusions and Perspectives

Conclusions

In this thesis, functional and accurate models to describe the sensing mechanisms in intensity-based fiber refractometers have been conceived and successfully implemented by combining Gaussian beam principles, ray optics, and wave optic analysis. On the one hand, Gaussian beam principles enable to characterize the injected beam (i.e. the input angular power distribution density) into the input end of the fiber refractometer. On the other hand, analytical equation wave optics can accurately describe and predict evanescent wave absorption (EWA) characteristics. Both Gaussian beam and wave optic principles are thus employed to support ray optic analysis of the propagation modes allowed in the MMF.

According to ray optic analysis, three sensing zones or regimes can be determined based on the different sensing mechanisms involved for each zone. In the first zone or Zone I, all rays or propagating modes along the sensor are guided by total internal reflection (TIR), generating evanescent waves as a result. Evanescent waves which penetrate into the cladding as well as into the sensing medium, can subsequently be absorbed. Hence, the sensing mechanism in Zone I is influenced only by EWA. In Zone II, two sensing mechanisms (i.e. mode loss and EWA) are concurrently involved in the sensor. In this Zone, the critical angle of the sensing medium is higher than the fiber's critical angle thereby inducing mode loss. In addition, EWA still occurs for the remaining modes which are still guided by TIR. The last sensing zone or Zone III describes the sensing mechanism due to Fresnel reflections when no propagating modes by TIR are allowed. As a result, the model for Zone I is typically employed when the sensing medium index (n_{sm}) is lower than the fiber cladding index (n_{cl}), while the Zone II model is employed for $n_{sm} \geq n_{cl}$, but $n_{sm} \leq n_{co}$ (the core index). However, the boundary between Zone I and Zone II cannot be defined as at n_{cl} when the incident beam angle θ_b is higher than the critical angle of the fiber θ_c. Under this condition, the boundary between Zone I and Zone II corresponds to the equivalent index (n_b) associated with θ_b ($n_b = n_{co} \sin \theta_b$), while the boundary n_{co}

between Zone II and Zone III remains unchanged, since the same plastic clad silica multimode fiber (MMF) is used.

The proposed models have then been developed for three types of refractometer namely, the MMF-based refractometer (Chapter II), the hybrid single-mode – multimode fiber refractometer (Chapter III), and the all-fiber hybrid refractometer based on solid-core photonic crystal fibers (PCFs) (Chapter IV), respectively. Good results (i.e. very small discrepancy of between simulation and experiment results) have been obtained by the second refractometer (hybrid single-mode – multimode fiber refractometer in Chapter III; see Figure 3.13). It can be explained by the fact that this refractometer does not have any inconvenience due to the use of opto-mechanical elements. It also has no optical components (e.g. lens and microscope objective) or fiber deformation structure which can alter the optical power density and/or modify the beam quality factor (M^2). On the contrary, for the first refractometer based on MMF (Chapter II), optical components such as collimators and microscope objectives could potentially modify M^2. In the case of the third refractometer (all-fiber hybrid refractometer based on solid-core PCFs in Chapter IV) deformations and collapses in the photonic crystal structure could change the optical power density. As a result, a relatively larger discrepancy has been observed for both refractometers, in particular for the third refractometer.

In terms of performance, all three types of refractometers have very high sensitivity in Zone II since in this zone, there are two sensing mechanisms (i.e. the mode loss and EWA) that lead to power loss. In addition, although the sensitivity of Zone III is low compared to Zone II, it was shown that this sensitivity can be increased by using hybrid single-mode – multimode sensor designs (the second refractometer), since it allows to launch the interrogating beam from a lead-in single-mode fiber (SMF) to the MMF with a small radiated angle. This will consequently reduce the number of reflections along the MMF, and thus leads to higher optical power being guided by Fresnel reflections. Likewise, the sensitivity in Zone I can also be increased by using the all-fiber hybrid solid-core PCF refractometer (the third refractometer), as it enables to propagate the light in the thin outer cladding, resulting in higher EWA. This is due to the fact that thin outer cladding of the PCFs enables to increase the

number of reflections along the sensor. Table A summarizes the performance of the refractometers which have been developed in this thesis.

Table A. Performance comparison between MMF refractometer, hybrid SMF-MMF refractometer, and hybrid refractometer based on PCFs.

		Dynamic range (RIU)	**Resolution (mRIU)**
MMF refractometer (1 cm)	**Beginning of Zone I**	1.316 – 1.37	17.7
	Zone II	1.37 – 1.444	0.02245
	Zone III	1.444 – 1.61	1.003
MMF refractometer (2.5 cm)	**Beginning of Zone I**	1.316 – 1.37	10.8
	Zone II	1.37 – 1.444	0.0299
	Zone III	1.444 – 1.61	1.807
MMF refractometer (4 cm)	**Beginning of Zone I**	1.316 – 1.37	8.34
	Zone II	1.37 – 1.444	0.0326
	Zone III	1.444 – 1.61	3.19
Hybrid SMF-MMF refractometer (2 cm)	**Beginning of Zone I**	1.316 – 1.4351	33.9
	Zone II	1.4351 – 1.444	0.00276
	Zone III	1.444 – 1.61	0.0283
Hybrid SMF-MMF refractometer (5 cm)	**Beginning of Zone I**	1.316 – 1.4351	16.4
	Zone II	1.4351 – 1.444	0.00397
	Zone III	1.444 – 1.61	0.139
Hybrid refractometer based on LMA-20 PCF (5 cm)	**Beginning of Zone I**	1.316 – 1.4351	6.65
Hybrid refractometer based on ESM-12B PCF (5 cm)	**Beginning of Zone I**	1.316 – 1.4351	1.97

Furthermore, one application of refractometers for gas sensing has been designed and fabricated to measure methane gas concentration using cryptophane-A supramolecules incorporated into a functionalized film of Styrene-Acrylonitrile (SAN) host using a hybrid SMF-MMF configuration. Once methane (CH_4) molecules are introduced into the target medium, cryptophane-A will trap the molecules of the gas. Subsequently, any variation of CH_4 concentration results in a

proportional variation of the refractive index of the sensing layer. Our present sensor offers a relatively fast response (~25 seconds). However, a detection limit of only ~174 ppm or 0.0174 % has currently been obtained. This result is 10 times inferior to the Mach-Zehnder interferometer-based CH_4 sensor which has a detection limit of 17 ppm [138]. Nevertheless, this sensor is still better than the long-period grating sensor with reported detection limits between 2 % [15] and 0.2 % [136]. Last, but not least, the current MMF refractometric methane sensor has been observed to exhibit a repeatability issue, where the sensitivity is degraded for subsequent utilization. The origin of this problem has unfortunately not been confirmed yet at the time of this manuscript write-up.

Perspectives

The current models can very accurately estimate the power response of the stripped-cladding MMF-based refractometers as demonstrated in Chapters II and III. These models, however, should be employed under the condition whereby the cladding is completely removed, without leaving any residual cladding material. In the case when the cladding is not totally removed, for example when using the etching process, where some µm (on the order of a wavelength) of the remaining cladding thickness might still exist in the sensing area, the models cannot be used to completely represent the sensing mechanisms. Under this condition, the current models have to take into account the additional mechanism of, namely, frustrated total internal reflection (F-TIR) [156]. With this additional model, the power response of the MMF refractometer for different thickness of cladding layer could then be efficiently estimated.

In terms of impact applications, the MMF refractometric methane sensor has demonstrated potentially good performance in terms of sensor response time. However, the origin of degradation in the measurement repeatability of this sensor must be further investigated and solved. Further studies should also be carried out to explore other host polymers compatible with cryptophane-A, in particular, for a refractive index range between 1.4351 to 1.444 RIU at 1550 nm (Zone II), since the

highest refractometer sensitivity is obtained in this range for the hybrid single-mode – multimode configuration.

The fiber refractometers could also be employed to detect other gases such as carbon dioxide (CO_2) and hydrogen sulfide (H_2S), or volatile organic compounds (VOC), for example BTEX (Benzene, Toluene, Ethyl benzene, and Xylenes). Using sensitive functional films based on phenol with didodecyl-dimethyl-ammonium hydroxide (DDMA) being used to deprotonate the phenols, CO_2 can then be detected due to the sensitized layer's index changes of the order of ~0.05 RIU for CO_2 concentration range from 10% to 90% [157]. Another low cost sensitive layer of poly(ethyleneimine) (PEI)/ poly(vinyl alcohol) (PVA) can also be used for detecting CO_2 with a concentration range of 7.6% – 86.9% [158]. Further, for detecting H_2S, zinc oxide (ZnO) film and nanorods can be used. An increase of the sensitized layer's index occurs when ZnO react with H_2S leading to the formation of zinc sulfide [159]. This sensor can detect very low concentrations of H_2S up to 60 ppm [159]. In the case of BTEX sensors, 0.01% of dichloro-methane (DCM) can be mixed with commercial polymers such as PDMS or poly[methyl(3,3,3-triflouropropyl)siloxane] (PMTFPS) as the sensitized polymeric film. The refractive index of the polymeric film will then vary reversibly as a function of BTEX concentration with a limit of detection of a few nanograms [160].

Moreover, the fiber refractometers can also be exploited as biochemical sensors, for example, for detecting thrombin, an important protein in the blood coagulation and homeostasis processes that are associated with certain diseases such as Alzheimer's disease, pregnancy-induced hypertension and thromboembolic disease. Thrombin can be detected by the refractometer because the RI of a functionalized surface of aptamers binding to thrombin varies about 1.3365 RIU depending on the concentration levels [161]. Finally, the fiber refractometers can also be employed as an electrochemical process sensor, for example, to monitor the state of charge in lithium batteries [162]. Here, the transmitted power along the MMF sensor varies when the battery is charged, due to the index variation of the graphite material.

List of publications

Conference paper

H. Apriyanto, G. Ravet, O. Bernal, M. Cattoen, F. Lizion, H. C. Seat, and V. Chavagnac, “A multimode fiber refractive index sensor,” in *Proc. IEEE Sensors*, 2016.

Journal paper

H. Apriyanto, G. Ravet, O. Bernal, M. Cattoen, F. Lizion, H. C. Seat, V. Chavagnac, F. Surre, and J. H. Sharp, “Comprehensive modeling of multimode fiber sensors for refractive index measurement and experimental validation,” *Sci. Rep.*, vol. 8, pp. 1-13, 2018.

Patent

H. Apriyanto, H. C. Seat, O. Bernal and F. Lizion, “Refractomètre à fibre optique hybride pour la mesure d’indice de réfraction d’un fluide et capteur correspondant,” *France Patent Application*, Reg. No. FR 1871600, submitted 20/11/2018.

References

[1] N. Cheung, "Charles K. Kao and other telecommunication pioneers," *IEEE Communications Magazine*, pp. S20-S27, 2010.

[2] K. T. V. Grattan, and T. Sun, "Fiber optic sensor technology: an overview," *Sens. Actuators A*, vol. 82, pp. 40–61, 2000.

[3] A. D. Kersey, "A review of recent developments in fiber optic sensor technology," *J. Opt. Fiber Tech.*, vol. 2, pp. 291–317, 1996.

[4] B. Lee, "Review of the present status of optical fiber sensors," *J. Opt. Fiber Tech.*, vol. 9, pp. 57–79, 2003.

[5] J. O. W. Norris, "Optical fiber chemical sensors: fundamentals and applications in Optical Fiber Sensor Technology," (eds K. T. V. Grattan and B. T. Meggitt,), pp. 337–375, Springer Science + Business Media, 2000.

[6] J. E. Saunders, C. Sanders, H. Chen, and H. P. Loock, "The refractive index of common solvents and solutions at 1550 nm," *Appl. Opt.*, vol. 55, pp. 947–953, 2016.

[7] G. Abbate, U. Bernini, E. Ragozzino, and F. Somma, "The temperature dependence of the refractive index of water," *J. Phys. D: Appl. Phys*., vol. 11, pp. 1167–1172, 1978.

[8] S. Valkai, J. Liszi, and I. Szalai, "Temperature dependence of the refractive index for three chloromethane liquids at 514.5 nm and 632.8 nm wavelengths," *J. Chem. Thermodynamics*, vol. 30, pp. 825–832, 1998.

[9] W. Xu, X. G. Huang, and J. S. Pan, "Simple fiber-optic refractive index sensor based on fresnel reflection and optical switch," *IEEE Sensors J.*, vol. 13, pp. 1571–1574, 2013.

[10] N. Yang, Q. Qiu, J. Su, and S. Shi, "Research on the temperature characteristics of optical fiber refractive index," *Int. J. Light. Electron Opt.*, vol. 125, pp. 5813–5815, 2014.

[11] T. Hu, Y. Zhao, and A. Song, "Fiber optic SPR sensor for refractive index and temperature measurement based on MMF-FBG-MMF structure," *Sens. Actuators B*, vol. 237, pp. 521–525, 2016.

[12] G. E. Badini, K. T. V. Grattan, A. W. Palmer, and A. C. C. Tseung, "Development of pH-sensitive substrates for optical sensor applications," *Springer Proc. In Physics Berlin*, vol. 44, pp. 436, 1989.

[13] B. D. MacCraith, V. Ruddy, C. Potter, B. O'Kelly, and J. F. McGilp, "Optical waveguide sensor using evanescent wave excitation of fluorescent dye in sol-gel glass," *Electron. Lett.*, vol. 27, pp. 1247–1248, 1991.

[14] S. Shibata, "Sol-gel-derived silica preforms for optical fibers," *J. Non-Crystalline Solids*, vol. 178, pp. 272–283, 1994.

[15] M. Benounis, N. Jaffrezic-Renault, J.-P. Dutastab, K. Cherif, and A. Abdelghani, "Study of evanescent wave optical fibre sensor for methane detection based on cryptophane molecules," *Sens. Actuators B*, vol. 107, pp. 32–39, 2005.

[16] Y.-C. Lin, "Characteristics of optical fiber refractive index sensor based on surface plasmon resonance," *Microwave Opt. Technol. Lett.*, vol. 55, pp. 574–576, 2013.

[17] A. K. Mishra, S. K. Mishra, and B. D. Gupta, "SPR based fiber optic sensor for refractive index sensing with enhanced detection accuracy and figure of merit in visible region," *Opt. Comm.*, vol. 344, pp. 86–91, 2015.

[18] S. K. Mishra, B. Zou, and K. S. Chiang, "Surface-Plasmon-Resonance Refractive-Index Sensor With Cu-Coated Polymer Waveguide," *IEEE Photon. Technol. Lett.*, vol. 28, pp. 1835–1838 2016.

[19] Y. Al-Qazwini, *et al.*, "Refractive index sensor based on SPR in symmetrically etched plastic optical fibers," *Sens. Actuators A*, vol. 246, pp. 163–169, 2016.

[20] L. Ji, *et al.*, "Surface plasmon resonance refractive index sensor based on ultraviolet bleached polymer waveguide," *Sens. Actuators B*, vol. 244, pp. 373–379, 2017.

[21] N. H. Wan, *et al.*, "High-resolution optical spectroscopy using multimode interference in a compact tapered fibre," *Nat. Commun.*, vol. 6, no. 7762, 2015.

[22] Y. Li, Z. Liu, and S. Jian, "Multimode interference refractive index sensor based on coreless fiber," *Photonic Sensors*, vol. 4, pp. 21–27, 2014.

[23] H. Fukano, T. Aiga, and S. Taue, "High-sensitivity fiber-optic refractive index sensor based on multimode interference using small-core single-mode fiber for biosensing," *Jpn. J. Appl. Phys.*, vol. 53, pp. (04EL08-1)–(04EL08-4), 2014.

[24] H. Fukano, T. Hashimoto, and S. Taue, "Reflection-type optical fiber refractive-index sensor using a multimode interference structure with high sensitivity," *Jpn. J. Appl. Phys.*, vol. 53, pp. (04EG05-1)–(04EG05-4), 2014.

[25] A. Iadicicco, A. Cusano, A. Cutolo, R. Bernini, and M. Giordano, "Thinned Fiber Bragg Gratings as High Sensitivity Refractive Index Sensor," *IEEE Photon. Technol. Lett.*, vol. 16, no. 4, pp. 1149-1151, 2004.

[26] W. Liang, Y. Huang, Y. Xu, R. K. Lee, and A. Yariv, "Highly sensitive fiber Bragg grating refractive index sensors," *Appl. Phys. Lett.*, vol. 86, pp. 151122–151122-3, 2005.

[27] J. F. Kuhne, A. M. Rocha, V. de Oliveira, H. J. Kalinowski, and R. C. Kamikawachi, "Experimental and numerical study on refractive index sensors based on fibre Bragg gratings inscribed in multimode fibre," *Meas. Sci. Technol.*, vol. 29, no. 025102, pp. 1-7, 2008

[28] Q. Wu, *et al.*, "Fiber refractometer based on a fiber Bragg grating and single-mode-multimode-single-mode fiber structure," *Opt. Lett.*, vol. 36, pp. 2197–2199, 2011.

[29] P. L. Swart, "Long-period grating Michelson refractometric sensor," *Meas. Sci. Technol.*, vol. 15, pp. 1576–1580, 2004.

[30] Jian Yang, Li Yang, Chang-Qing Xu, Chenglin Xu, Weiping Huang, and Yingfu Li, "Long-period grating refractive index sensor with a modified cladding structure for large operational range and high sensitivity," *Appl. Opt.*, vol. 45, pp. 6142-6147, 2006.

[31] V. Bhatia, "Optical fiber long-period grating sensors," *Opt. Lett.*, vol. 21, pp.692-694, 2009.

[32] Nidhi, R.S. Kaler, Umesh Tiwari, Vandana Mishra, Nahar Singh, Pawan Kapur, "Investigation of Long Period Grating as refractive index sensor," *Int. J. Light Electron Opt.*, vol. 123, no. 12, pp. 1071-1073, 2012.

[33] W. Xu, X. G. Huang, and J. S. Pan, "Simple fiber-optic refractive index sensor based on fresnel reflection and optical switch," *IEEE Sensors J.*, vol. 13, no. 5, pp. 1571–1574, 2013.

[34] J. Villatoro, D. Monzón-Hernández, and D. Talavera, "High resolution refractive index sensing with cladded multimode tapered optical fibre," *Electron. Lett.*, vol. 40, 106-107, 2004.

[35] Y. M. Wong, P. J. Scully, H. J. Kadim, V. Alexiou, and R. J. Bartlett, "Automation and dynamic characterization of light intensity with applications to tapered plastic optical fibre," *J. Opt. A: Pure Appl. Opt.*, vol. 5, pp. S51–S58, 2003.

[36] A. Banerjee, *et al.*, "Fiber optic sensing of liquid refractive index," *Sens. Actuators B*, vol. 123, pp. 594-605, 2007.

[37] F. Sequeira, *et al.*, "Refractive index sensing with d-shaped plastic optical fibers for chemical and biochemical applications," *Sensors*, vol. 16, no. 2119, pp. 1-11, 2016.

[38] F. De-Jun, Z. Mao-Sen, G. Liu, L. Xi-Lu, and J. Dong-Fang, “D-shaped plastic optical fiber sensor for testing refractive index,” *IEEE Sensors J.*, vol. 14, pp. 1673-1676, 2014.

[39] G. Liu, and D. Feng, “Evanescent wave analysis and experimental realization of refractive index sensor based on D-shaped plastic optical fiber,” *J. Light. Electron Opt.*, vol. 127, pp. 690-693, 2016.

[40] T. Kuwana, “Physical methods in modern chemical analysis,” Academic Press, New York : 1980.

[41] E. Hecht, "Optics fourth edition," Addition Wesley, New York : 2002

[42] J. Golebiowski, T.Prohun, “Dual-Channel filter photometer system for biocomponent content determnaion in diesel oil,” *Meas. Sci. Technol.,* vol. 19, article id. 075301, pp. 1-6, 2008.

[43] V. Kontturi, S. Hyvärinen, A. García, R Carmona, D. Yu Murzin, J-P. Mikkola and K-E. Peiponen, “Simultaneous detection of the absorption Spectrum and refractive index ratio with a spectrophotometer: Monitoring contaminants in bioethanol,” *Meas. Sci. Technol.,* vol. 22, pp. 1-6, 2011.

[44] M. Ventura, E. Simionatto, L.H.-C. Andrade, E.L. Simionatto, D. Riva, S.-M. Lima, “The use of thermal lens spectroscopy to assess oil-biodiesel blends,” *Fuel*, vol. 103, pp. 506–511, 2013.

[45] B. Kanyathare, K.-E. Peiponen, “Hand-Held Refractometer-Based Measurement and Excess Permittivity Analysis Method for Detection of Diesel Oils Adulterated by Kerosene in Field Conditions,” *Sensors*, vol. 18, 1551, 2018.

[46] http://www.refractometer.pl/refractometer-history.

[47] http://www.refractometer.pl/immersion-refractometer.

[48] S. E. Thompson, “Hand-held refractometer,” *U.S. Patent*, No. USD348849S, 1994.

[49] Y. Nakajima, H. Amamiya, M. Osawa, K. Sekiguchi, “Refractometer,” *US Patent*, No. US7492447B2, 2009.

[50] G. H. Hulands and J. F. Nunn, “Portable interference refractometers in anaesthesia,” *Br. J. Anaesth.*, vol. 42, pp. 1051-1059, 1970.

[51] K. V. Diprose and L. R. Redman, “An automatic interference refractometer,” *Br.J. Anaesth*., vol. 50, pp. 1155-1158, 1978.

[52] K. D. Singer, M. S. Merlin, S. J. Lalama, and A. F. Garito, “Interferometric refractometer for measuring the relative refractive index of two liquids,” *Rev. Sci. Instrum.*, vol. 53, pp. 202-204, 1982.

[53] N. S. Kapany and J. N. Pike, “Fiber Optics. Part IV. A Photorefractometer,” *J. Opt. Soc. Am.*, vol. 47, pp. 1109-1117, 1957.

[54] N. S. Kapany and D. A. Pontarelli, “Photorefractometer I. Extension of Sensitivity and Range,” *Appl. Opt.*, vol. 2, pp. 425-430, 1963.

[55] N. S. Kapany and D. A. Pontarelli, “Photorefractometer II. Measurement of N and K,” *Appl. Opt.*, vol. 2, pp. 1043-1048 1963.

[56] David, D. J. Shaw, D. and Tucker, H, “Design, development, and performance of a fiber optics refractometer: Application to HPLC,” *Rev. Sci. Instrum*., vol. 47, pp. 989-997, 1976.

[57] A. Arie, R. Karoubi, Y. S. Gur, and M. Tur, “Measurement and analysis of light transmission through a modified cladding optical fiber with applications to sensors,” *Appl. Opt.*, vol. 25, pp. 1754-1758, 1986.

[58] A. Arie, M. Tur, and S. Goldsmith, “Measurement and analysis of a modified cladding optical fiber with various input illuminations,” in *Fiber Optic and Laser Sensors IV*, SPIE, 1986.

[59] A. Arie and M. Tur, “Light transmission through a modified cladding optical fiber - inverse problem analysis,” in *Sixth Meeting in Israel on Optical Engineering*, SPIE, 1988.

[60] W. Golunski, R. Hypszer, and J. Plucinski, “Optical fibre refractometer for liquid refractive index measurement,” in *Optical Fibres and Their Applications V*, SPIE, 1989.

[61] C. F. Cole, A. J. Adams, and R. A. Sims, “An Optical Fiber Refractometer for Measuring the Dispersion of Turbid Fluids,” in *Chemical, Biochemical, and Environmental Fiber Sensors IV*, SPIE, 1992.

[62] A. Mukherjee, D. Munsi, V. Saxena, R. Rajput, P. Tewari, V. Singh, A. K. Ghosh, J. John, H. Wanare, and P. Gupta-Bhaya, "Characterization of a fiber optic liquid refractive index sensor," *Sens. Actuator B*, vol. 145, pp. 265–271, 2010.

[63] C.-H. Chen, T.-C. Tsao, J.-L. Tang, and W.-T. Wu, “A Multi-D-Shaped Optical Fiber for Refractive Index Sensing,” *Sensors*, vol. 10, pp. 4794-4804, 2010.

[64] R. A. Paselk, “The Evolution of the Abbé Refractometer,” *Bulletin of the Scientific Instrument Society*, vol. 62, pp. 19-22, 1999.

[65] W. B. Jensen,"Refractometers," in *Oesper Museum Booklets on the History of Chemical Apparatus*, no. 3, University of Cincinnati, 2014.

[66] www2.humboldt.edu/scimus/RefracExhibit/AbbeDesc/ZeissAbbe1893.htm

[67] http://www.refractometer.pl/Abbe-refractometer

[68] https://www2.humboldt.edu/scimus/RefracExhibit/SpecPics/CZ_Pulf_Acc_Prz.jpg

[69] http://www.refractometer.pl/Pulfrich-refractometer

[70] www2.humboldt.edu/scimus/RefracExhibit/SpecDesc/ZeissDip_Lcase.htm

[71] www2.humboldt.edu/scimus/RefracExhibit/SpecDesc/CZ_HandRef.htm

[72] http://www.refractometer.pl/hand-held-refractometer

[73] P. Bhatia and B. D.Gupta, “Surface-plasmon-resonance-based fiber-optic refractive index sensor: sensitivity enhancement,” *Appl. Opt.*, vol. 50, pp. 2032-2036, 2011.

[74] B. D. Gupta, S. K. Srivastava, and R. Verma, “Fiber optic sensors based on plasmonics,” World Scientific Publishing Co. Pte. Ltd., Singapore: 2015.

[75] Y. Jung, S. Kim, D. Lee and K. Oh, “Compact three segmented multimode fibre modal interferometer for high sensitivity refractive-index measurement,” *Meas. Sci. Technol*., vol. 17, pp. 1129-1133, 2006.

[76] J. Wang, Y. Jin, Y. Zhao, and X. Dong, “Refractive index sensor based on all-fiber multimode interference,” *Int. J. Light. Electron Opt.*, vol. 124, pp. 1845-1848, 2013.

[77] A. Asseh, S. Sandgren, H. Ahlfeldt, B. Sahlgren, R. Stubbe, and G. Edwall, “Fiber Optical Bragg Grating Refractometer,” *Fiber and Integrated Optics*, vol. 17, pp. 51-62, 1998.

[78] A. Othonos, K. Kalli, D. Pureur and A. Mugnier, “Wavelength Filters in Fibre Optics,” Springer, pp. 189-269, Verlag Berlin Heidelberg: 2006.

[79] H. Tsuda and K.Urabe, “Characterization of Long-period Grating Refractive Index Sensors and Their Applications,” *Sensors*, vol. 9, pp. 4559-4571, 2009.

[80] J. H. Chong, P. Shum, H. Haryono, A. Yohana, M.K. Rao, C. Lu, and Y. Zhu, “Measurements of refractive index sensitivity using long-period grating refractometer,” *Opt. Comm*., vol. 229, pp. 65–69, 2004.

[81] A. Singh, S. B. Rana, M. Singh, and A. Sharma, “Study and investigation of long period grating as refractive index sensor,” *Int. J. Light. Electron Opt.*, vol. 125, pp. 1860-1863, 2014.

[82] C.B. Kim and C. B. Su, “Measurement of the refractive index of liquids at 1.3 and 1.5 micron using a fibre optic Fresnel ratio meter,” *Meas. Sci. Technol*., vol. 15, pp. 1683-1686 (2004).

[83] J. Yuan, C. Zhao, M. Ye, J. Kang, Z. Zhang, and S. Jin, “A Fresnel Reflection-Based Optical Fiber Sensor System for Remote Refractive Index Measurement Using an OTDR,” *Photon. Sensors*, vol. 4, pp. 48-52, 2014.

[84] K. Yüksel, “Optical fiber sensor system for remote and multi-point refractive index measurement,” *Sens. Actuators A*, vol. 250, pp. 29-34, 2016.

[85] H. Apriyanto, G. Ravet, O. D. Bernal, M. Cattoen, H. C. Seat, V. Chavagnac, F. Surre, J. H. Sharp, "Comprehensive modeling of multimode fiber sensors for refractive index measurement and experimental validation," Sci. Rep., vol. 8, no. 5912, 2018.

[86] C. Boulart, M. C.Mowlem, D. P. Connelly, J.-P. Dutasta, and C. R.German, “A novel, low-cost, high performance dissolved methane sensor for aqueous environments,” *Opt. Express*, vol. 16, pp. 12607–12617, 2008.

[87] A.L. Chaudharia and A.D. Shaligramb, “Multi-wavelength optical fiber liquid refractometry based on intensity modulation,” *Sens. Actuators A*, vol. 100, pp. 160-164, 2002.

[88] A.L. Chaudharia and A.D. Shaligramb, “Simulation and experimental studies of an extrinsic fiber optic sensor for liquid refractometry,” *Int. J. Light. Electron Opt.*, vol. 124, pp. 3134-3137, 2013.

[89] M. E. Muthuraju, A. R. Patlollaa, B. V. Canthadaia, and V. Pachavab, “Low cost fiber optic sensing of sugar solution,” in *Optical Fibers and Sensors for Medical Diagnostics and Treatment Applications XV*, SPIE, 2015.

[90] B. E. A. Saleh and M. C. Teich, “Fundamental of Photonics,” John and Wiley & Sons, New York: 2007.

[91] S. John, “Evanescent Wave Fibre Optic Sensors : Design, Fabrication and Characterization,” PhD Thesis, India: Cochin University of Science & Technology, 2000.

[92] D. L. Woerdeman and R. S. Parnas, "Model of a Fiber-Optic Evanescent-Wave Fluorescence Sensor," *Applied Spectroscopy*, vol. 55, no. 3, pp. 331-337, 2001.

[93] B.K. Keller, M.D. DeGrandpre, and C.P. Palmer, “Waveguiding properties of fiber-optic capillaries for chemical sensing applications,” *Sens. Actuators B*, vol. 125, pp. 360–371, 2006.

[94] https://www.thorlabs.com/thorproduct.cfm?partnumber=BFL48-200

[95] https://www.thorlabs.com/thorproduct.cfm?partnumber=F220APC-1550

[96] A. E. Siegman, “Lasers,” University Science Books, Mill Valley: 1986.

[97] A.M. Kowalevicz Jr. and F. Bucholtz, “Beam Divergence from an SMF-28 Optical Fiber,” in *Naval Research Laboratory Memorandum Report OMB*, No. 0704-0188, Washington DC, USA (2006).

[98] F. A. Jenkins and H. E. White, “Fundamentals of optics,” McGraw-Hill Book Company, vol. 7, p. 473, New York: 2007.

[99] R. T. Schermer and J. H. Cole, “Improved bend loss formula verified for optical fiber by simulation and experiment,” *IEEE J. Quant. Electron.* Vol. 43, pp. 899–909, 2007.

[100] A. J. Fleming, “A review of nanometer resolution position sensors: Operation and performance,” *Sens. Actuators A*, vol. 190, pp. 106-126, 2013.

[101] W. O. Grant, “Understanding lightwave transmission: applications of fiber optics,” Harcourt Brace Jovanovich publisher, New York: 1998.

[102] https://www.comsol.com/blogs/using-perfectly-matched-layers-and-scattering-boundary-conditions-for-wave-electromagnetics-problems/

[103] https://www.thorlabs.com/drawings/770825baa935cad0-C8F3C0D5-A4B3-20D8-0033E053A3FD8E10/FP200ERT-SpecSheet.pdf

[104] T. A. Birks, P. J. Roberts, P. St. J. Russell, D. M. Atkin, T. J. Shepherd, “Full 2-D photonic bandgaps in silica/air structures,” *Electron. Lett.*, vol. 31, pp. 1941-1942, 1995.

[105] E. Yablonovitch, “Photonic band-gap structures,” *J. Opt. Soc. Am.*, vol. 10, pp. 283-295, 1993.

[106] P. Russel, "Photonic Crystal Fibers," *Science*, vol. 299, pp. 358-362, 2003.

[107] J. C. Knight, T. A. Birks, P. St. J. Russell, and D. M. Atkin, “All-silica single mode optical fiber with photonic crystal cladding,” *Opt. Lett*., vol. 21, pp. 1547-1549, 1996.

[108] T. A. Birks, J. C. Knight, and P. St. J. Russell, “Endlessly single-mode photonic crystal fiber,” *Opt. Lett*. 22, 961-963, 1997.

[109] M. Nielsen, C. Jacobsen, N. Mortensen, J. Folkenberg, and H. Simonsen, “Low-loss photonic crystal fibers for transmission systems and their dispersion properties,” *Opt. Express*, vol. 12, pp. 1372-1376, 2004.

[110] J. Villatoro, V. Finazzi, V. P. Minkovich, V. Pruneri, and G. Badenes, “Temperature-insensitive photonic crystal fiber interferometer for absolute strain sensing,” *Appl. Phys. Lett.*, vol. 91, Article ID 091109, 2007.

[111] Q. Shi, F. Y. Lv, Z. Wang et al., “Environmentally stable Fabry-Perot-type strain sensor based on hollow-core photonic bandgap fiber,” *IEEE Photon. Technol. Lett.*, vol. 20, pp. 237–239, 2008.

[112] H. Zhang, B. Liu, Z. Wang et al., “Temperature-insensitive displacement sensor based on high-birefringence photonic crystal fiber loop mirror,” *Optica Applicata*, vol. 40, pp. 209–217, 2010.

[113] J.N. Dash, R. Jha, J. Villatoro, and S. Dass, "Nano-displacement sensor based on photonic crystal fiber modal interferometer," *Opt. Lett.*, vol. 40, pp. 467-470, 2015.

[114] J. Ju, Z. Wang, W. Jin, and M. S. Demokan, “Temperature sensitivity of a two-mode photonic crystal fiber interferometric sensor,” *IEEE Photon. Technol. Lett.*vol. 18, no. 20, pp. 2168–2170, 2006.

[115] D. Monzon-Hernandez, V. P. Minkovich, and J. Villatoro, “High-temperature sensing with tapers made of microstructured optical fiber,” *IEEE Photon. Technol. Lett.*, vol. 18, pp. 511–513, 2006.

[116] H. Y. Choi, K. S. Pack, S. J. Park, U. C. Paek, B. H. Lee, and E. S. Choi, “Miniature fiber-optic high temperature sensor based on a hybrid structured Fabry-Perot interferometer,” *Opt. Lett.*, vol. 33, pp. 2455–2457, 2008.

[117] W. J. Bock, J. Chen, T. Eftimov, and W. Urbanczyk, “A photonic crystal fiber sensor for pressure measurements,” *IEEE T. Instrum. Meas.*, vol. 55, pp. 1119–1123, 2006.

[118] H. K. Gahir and D. Khanna, “Design and development of a temperature-compensated fiber optic polarimetric pressure sensor based on photonic crystal fiber at 1550 nm,” *Appl. Opt.*, vol. 46, pp. 1184–1189, 2007.

[119] T. Martynkien, M. Szpulak, G. Statkiewicz et al., “Measurements of sensitivity to hydrostatic pressure and temperature in highly birefringent photonic crystal fibers,” *Optical and Quantum Electronics*, vol. 39, pp. 481–489, 2007.

[120] Y. S. Shinde and H. K. Gahir, “Dynamic pressure sensing study using photonic crystal fiber: application to tsunami sensing,” *IEEE Photon. Technol. Lett.*, vol. 20, no. 4, pp. 279–281, 2008.

[121] J. B. Jensen, L. H. Pedersen, P. E. Hoiby, L. B. Nielsen, T. P. Hansen, J. R. Folkenberg, J. Riishede, D. Noordegraaf, K. Nielsen, A. Carlsen, and A. Bjarklev, “Photonic crystal fiber based evanescent-wave sensor for detection of biomolecules in aqueous solutions,” *Opt. Lett*., vol. 29, 1974–1976 (2004).

[122] J. B. Jensen, P. E. Hoiby, G. Emiliyanov, O. Bang, L. H. Pedersen, and A. Bjarklev, “Selective detection of antibodies in microstructured polymer optical fibers,” *Opt. Express*, vol. 13, pp. 5883–5889, 2005.

[123] L. Rindorf, J. B. Jensen, M. Dufva, L. H. Pedersen, P. E. Høiby, and O. Bang, "Photonic crystal fiber long-period gratings for biochemical sensing," *Opt. Express*, vol. 14, pp. 8224-8231, 2006.

[124] L. Rindorf, P. E. Hoiby, J. B. Jensen, L. H. Pedersen, O. Bang, and O. Geschke, “Biomolecule detection with integrated evanescent-wave microstructured optical fibre sensor,” *Anal. Bioanal. Chem*., pp. 1–6, 2006.

[125] Y. L. Hoo, W. Jin, H. L. Ho, D. N. Wang, and R. S. Windeler, “Evanescent-wave gas sensing using microstructure fiber,” *Opt. Engineering*, vol. 41, pp. 8–9, 2002.

[126] Q. Wang, D. Wu, L. Bai, W. Hou and Y. Zhao, “Improved sensitivity of a photonic crystal fiber evanescent-wave gas sensor,” *Instrum. Sci. Technol.*, vol. 41:2, 202-211, 2013.

[127] L. Kornaszewski, N. Gayraud, J. M. Stone et al., “Mid-infrared methane detection in a photonic bandgap fiber using a broadband optical parametric oscillator,” *Opt. Express*, vol. 15, no. 18, pp. 11219–11224, 2007.

[128] A. M. Cubillas, J. M. Lazaro, M. Silva-Lopez, O. M. Conde, M. N. Petrovich, and J. M. Lopez-Higuera, “Methane sensing at 1300 nm band with hollow-core photonic bandgap fibre as gas cell,” *Electron. Lett*., vol. 44, no. 6, pp. 403–405, 2008.

[129] E. Austin, A. van Brakel, M. N. Petrovich, and D. J. Richardson, “Fibre optical sensor for c_2h_2 gas using gas-filled photonic bandgap fibre reference cell,” *Sens. Actuators B*, vol. 139, no. 1, pp. 30–34, 2009.

[130] T. Ritari, J. Tuominen, H. Ludvigsen et al., “Gas sensing using air-guiding photonic bandgap fibers,” *Opt. Express*, vol. 12, no. 17, pp. 4080–4087, 2004.

[131] J. B. Jensen, L. H. Pedersen, P. E. Hoiby, L. B. Nielsen, T. P. Hansen, J. R. Folkenberg, J. Riishede, D. N., K. Nielsen, A. Carlsen, and A. Bjarklev, "Photonic crystal fiber based evanescent-wave sensor for detection of biomolecules in aqueous solutions," *Opt. Lett*., vol. 29, pp. 1974-1976, 2004.

[132] J. Jian, “Highly Birefringence Photonic Crystal Fibers and sensors.,” PhD Thesis, The Hong Kong Polytechnic University, 2006.

[133] J. Ju, W. Jin, Y. L. Hoo, and M. S. Demokan, “A simple method for estimating splice loss of photonic crystal fiber/single-mode fiber,” *Microw. Opt. Technol. Lett*., vol**.** 42, pp. 171-173, 2004.

[134] J.Gabard and André Collet, “Synthesis of a (D3)-bis(cyclotriveratrylenyl) macrocage by stereospecific replication of a (C3)-subunit,” *J. the Chemical Society, Chemical Communications*, no. 21, pp. 1137-1139, 1981.

[135] L.Garel, J. P. Dutastaand A. Collet, “Complexation of methane and chlorofluorocarbons by cryptophane-A in organic solution,”*Angew. Chem. Int. Ed*., vol. 32, pp. 1169–1171; 1993.

[136] J. Yang, Ch. Tao, X. Li, G. Zhu, and W. Chen, “Long-period fiber grating sensor with a styrene-acrylonitrile nano-film incorporating cryptophane A for methane detection,” *Opt. Express*, vol. 19, pp. 14696–14706, 2011.

[137] J. Yang, L. Zhou, J. Huang, Ch. Tao, X. Li, and W. Chen, “Sensitivity enhancing of transition mode Long-Period Fiber Grating as methane sensor using high refractive index polycarbonate/ cryptophane Aoverlay deposition,” *Sens. Actuators B*, vol. 207, pp. 477–480, 2015.

[138] F. T. Dullo, S. Lindecrantz, J. Jágerská, J. H. Hansen, M. Engqvist, S. A.Solbø, and O. G.Hellesø, "Sensitive on-chip methane detection with a cryptophane-A cladded Mach-Zehnder interferometer," *Opt. Express*, vol. 23, pp. 31564-31573, 2015.

[139] J. W. Steed and J. L. Atwood, “Supramolecular chemistry,” John Wiley & Sons, 2013.

[140] J.T. Houghton, G.J. Jenkins, and J.J. Ephraums, “Climate Change,” The IPCC assessment, Cambridge University Press: 1990.

[141] https://climatechangeconnection.org/emissions/co2-equivalents.

[142] https://www.epa.gov/ghgemissions/overview-greenhouse-gases.

[143] A.S. Hakemian, and A.C. Rosenzweig, “The Biochemistry of Methane Oxidation,” *Annual Review of Biochemistry*, 76(1): 223-241, 2007.

[144] https://www.globalmethane.org/documents/gmi-mitigation-factsheet.pdf

[145] J. P.Kennett, K. G. Cannariato, I. L. Hendy, *and* R. J. Behl*, ”*Methane Hydrates in Quaternary Climate Change: The Clathrate Gun Hypothesis*,” Spec. Publ. Ser.*, vol. *54*, Washington, *D. C.:* 2003.

[146] L. de Angelis and R. Riva, “Selectivity and stability of a tin dioxide sensor for methane,” *Sens. Actuators B*, vol. 28, pp. 25-29, 1995.

[147] F. Quaranta, R. Rella, P. Siciliano, S. Capone, M. Epifani, L. Vasanelli, A. Licciulli, and A. Zocco, “A novel gas sensor based on SnO_2/Os thin film for the detection of methane at low temperature,” *Sens. Actuators B*, vol. 58, pp. 350-355, 1999.

[148] B. W. Licznerski, K. Nitsch, H. Teterycz, P. M. Szecowka, and K. Wisniewski, “Humidity insensitive thick film methane sensor based on SnO_2/Pt,” *Sens. Actuators B*, vol. 57, pp. 192-196, 1999.

[149] P. N. Bartlett and S. Guerin, “A micromachined calorimetric Gas Sensor: an application of electrodeposited nanostructured palladium for the detection of combustible gases,” *Anal. Chem*., vol. 75, pp. 126-132, 2003.

[150] H. Debeda, L. Dulau, P. Dondon, F. Menil, C. Lucat and P. Massok, “Development of a reliable methane detector,” *Sens. Actuators B*, vol. 44, pp. 248-256, 1997.

[151] S. Schilt, A. Vicet, R. Werner, M. Mattiello, L. Thévenaz, A. Salhi, Y. Rouillard and J. Koeth, “Application of antimonide diode lasers in photoacoustic spectroscopy,” *Spectrochim. Acta, Part A: Mol. Biomol. Spectr*., vol. 60, pp. 3431-3436, 2004.

[152] C. Boulart, R. Prien, V. Chavagnac, and J-P. Dutasta, “Sensing dissolved methane in aquatic environments : an experiment in the central Baltic Sea using surface plasmon resonance,” *Environmental science & technology*, vol. 45, pp. 8582-8590, 2013.

[153] J. Yang, L. Xu, and W. Chen, "An optical fiber methane gas sensing film sensor based on core diameter mismatch," *Chin. Opt. Lett.*, vol. 8, pp. 482-484, 2010.

[154] J. Yang, J. Huang, X. Li, S. Li, B. Luo, C. Tao and W. Chen, “High-sensitivity long-period fiber grating sensor with SAN/cryptophane A for coal mine gas detection,” *Chin. Opt. Lett.*, vol. 11, pp. *080601,* 2013.

[155] S. M. Lindecrantz, “Waveguide Mach-Zehnder interferometer for measurement of methane dissolved in water,” PhD dissertation, The Arctic University of Norway, 2016.

[156] Z. Voros and R. Johnsen, “A simple demonstration of frustrated total internal reflection,” *Am. J. Phys.*, vol. 76, pp.746-749, 2008.

[157] C. Gouveia, A. Markovics, and J.M. Baptista, “Measurement of CO_2 using refractometric fiber optic sensors,” *in Proc. 3rd WSEAS Int. Conf. Adv. Sensors, Signals Mater*., 2010.

[158] W. Ma, R. Wang, Q. Rong, Z. Shao, W. Zhang, T. Guo, J. Wang, and X. Qiao, “CO_2 gas sensing using optical fiber Fabry-Perot interferometer based on polyethyleneimine/ poly(vinyl alcohol) coating,” *IEEE Photon. J.*, vol. 9, pp. 1-8, 2017.

[159] S. P. Usha, S. K. Mishra, and B. D. Gupta, “Zinc oxide thin film/ nanorods based lossy mode resonance hydrogen sulphide gas sensor,” *Materials research express*, vol. 2, pp. 1-11, 2015.

[160] L. I. B. Silva, A. V. Pantheleitchouck, A. C. Freitas, T. A. P. Rocha-Santos, and A. C. Duarte, "Microscale optical fiber sensor for BTEX monitoring in landfill leachate," *Analytical methods*, vol. 1, pp. 100-107, 2009.

[161] D. Sun, L.-P. Sun, T. Guo, and B.-O, Guan, "Label-free Thrombin detection using a tapered fiber-optic interferometric Aptasensor," *J. Lightwave. Technol.*, 2018. DOI: 10.1109/JLT.2018.2878762.

[162] A.R. Ghannoum, P. Nieva, A. Yu, and A. Khajepour, "Development of embedded fiber-optic evanescent wave sensors for optical characterization of Graphite anodes in lithium-ion batteries," *Appl. Mater. Interfaces*, vol. 9, pp. 41284-41290, 2017.